

Important Notice

This copy may be used only for the purposes of research and private study, and any use of the copy for a purpose other than research or private study may require the authorization of the copyright owner of the work in question. Responsibility regarding questions of copyright that may arise in the use of this copy is assumed by the recipient.

UNIVERSITY OF CALGARY

Exact, linear and nonlinear AVO modeling in poroelastic media

by

Steven M. Kim

A THESIS

SUBMITTED TO THE FACULTY OF GRADUATE STUDIES
IN PARTIAL FULFILMENT OF THE REQUIREMENTS FOR THE
DEGREE OF MASTER OF SCIENCE

DEPARTMENT OF GEOSCIENCE

CALGARY, ALBERTA

APRIL, 2014

© Steven M. Kim 2014

Abstract

An exact, analytical solution for PP reflection amplitudes is derived for poroelastic media as a result of incorporating the poroelastic parameters of fluid (f), shear modulus (μ), and density (ρ) into the elastic Zoeppritz equations. This solution contains many terms which may be neglected to produce first (linear), second (nonlinear) and third (nonlinear) order approximations. These approximations are derived in terms of perturbations (a_f, a_μ, a_ρ) and reflectivities ($\Delta f/f, \Delta\mu/\mu, \Delta\rho/\rho$). These results are expected to extend to dynamic poroelastic models of wave propagation and initial groundwork for this extension is reported. When modeling reflection amplitudes of media with small poroelastic contrasts (10%), the first order approximation yields 5% error for the zero offset reflection amplitude and much less than 1% error for the third order approximation. By changing the media properties to replicate large poroelastic contrasts (50%), the first order approximation produces 20% error for the zero offset reflection amplitude and less than 1% error for the third order approximation. Nonlinear corrective terms of order 2 and 3 are, therefore, relevant for poroelastic AVO analysis in geophysically realistic scenarios.

Acknowledgements

The manner in which this thesis has been compiled is, in large part, from the interactions and experiences that I have had as a Master's student, and there are many people that I would like to express gratitude towards. Of those people, I would first like to dedicate a tremendous amount of appreciation to my supervisor Dr. Kris Innanen for his leadership, guidance, and more importantly, patience; he has played an important role in shaping my career as a geophysicist. Secondly, I would like to thank the CREWES business manager, Laura Baird, for making graduate student life all the more pleasurable in many aspects.

My research on the topic of poroelastic AVO was generously funded by a university grant provided by Imperial Oil and for that, I am very grateful and would like to acknowledge them for their support.

A major component of this thesis is based on Dr. Brian Russell's work on poroelastic AVO and I feel fortunate to have had the opportunity to speak with him on several occasions; he has provided insightful and positive feedback during the incremental stages of my research. I would like to thank Dr. Harvey Yarranton for agreeing to be one of the examiners of my defense and Dr. Bernard Guest for being the neutral chair.

I would like to thank Rolf Maier and Kevin Hall for helping me whenever possible when it came to any technical computing issues and to Joe Wong and Peter Manning for their useful discussions and comments. I would also like to thank Dave Henley for giving me career advice

and some industry background knowledge and to Dr. John Bancroft for giving me the initial push early on as a grad student.

There are many fellow Master's students and classmates that I have spent time conversing with. I greatly value sharing this entire experience as a graduate student with Heather Lloyd, Hormoz Izadi, Andrew Nicol, Jessie Arthur, Byron Kelly, Chris Bird, Melissa Hernandez, Peter Gagliardi, Matt McDonald, Diane Lespinasse, Virginia Vera, Marcus Wilson, Patricia Gavotti, Xinxiang Li, Oliver Lahr, Saúl Guevara, and Glen Young. The students pursuing their PhD's provided the much needed wisdom and support to help me gauge what was to come during the course of my program, and what I should expect. I will remember having discussions with Dave Cho, Ben Wards, Shahin Moradi, Shahin Jabbari, Hassan Khaniani, Mahdi Al Mutlaq and Faranak Mahmoudian.

I have also enjoyed speaking with some of the newer students of CREWES and hoped to have given them useful advice by sharing my knowledge with Wenyong Pan, Paul McGee, Jesse Kolb, Adrian Smith, Penny Pan, Rafael Asuaje, Babatunde Arenrin and to anyone else who I may have missed.

Finally, I would like to show my appreciation to Roy Lindseth for assisting me during the final editing stage of my thesis and talking to me about his experiences as a geophysicist.

Dedication

To my parents, Simon and Nancy

Table of Contents

Abstract	ii
Acknowledgements	iii
Dedication	v
Table of Contents	vi
List of Tables	viii
List of Figures and Illustrations	ix
List of Symbols, Abbreviations and Nomenclature	xi
CHAPTER ONE: INTRODUCTION	1
1.1 Statement of the problem	1
1.2 Concepts, terms and technical overview	2
1.2.1 Elementary wave field behaviour	3
1.2.2 Reflection at a boundary: AVO and the Zoeppritz equations	7
1.3 AVO analysis	10
1.3.1 Development of seismic amplitude analysis	10
1.3.2 Fluid discrimination from AVO analysis	13
1.4 Thesis overview	14
CHAPTER TWO: THEORETICAL BACKGROUND	16
2.1 Chapter overview	16
2.2 The Zoeppritz equations in a geological setting	16
2.2.1 Case study applications of exact solutions	16
2.2.2 Issue with exact solutions	23
2.2.3 AVO approximations	23
2.3 Poroelasticity	24
2.4 The Russell-Gray linear poroelastic AVO model	27
2.5 Chapter summary	28
CHAPTER THREE: EXACT EXPRESSIONS FOR POROELASTIC R_{PP} , R_{PS} , R_{SS} , R_{SP}	29
3.1 Chapter overview	29
3.2 A convenient formulation of the Zoeppritz equations	29
3.2.1 Case 1 – incident P-wave	31
3.2.2 Case 2 – incident S-wave	35
3.3 The transformation from V_P , V_S , ρ to f , μ , ρ	38
3.4 The P-wave and S-wave Zoeppritz equations in poroelastic terms (f , μ , ρ)	39
3.4.1 Incident P-wave	39
3.4.2 Incident S-wave	42
3.5 Solutions for R_{PP} , R_{PS} , R_{SS} , R_{SP}	44
3.6 Chapter summary	45
CHAPTER FOUR: SERIES SOLUTIONS FOR POROELASTIC R_{PP}	46
4.1 Chapter overview	46
4.2 The poroelastic P-wave Zoeppritz equations in perturbative form	46
4.3 Series expansion of the solution for R_{PP}	50

4.3.1 Expansion of each element of the Zoeppritz matrix.....	50
4.3.2 Expansion of the determinant ratios	53
4.4 Transformation from perturbative form to reflectivity form	54
4.5 The $(\gamma_1)_{\text{dry}}^2$ parameter	56
4.6 Chapter summary	57
CHAPTER FIVE: EXACT, LINEAR, AND NONLINEAR POROELASTIC AVO MODELING: VALIDATION AND ANALYSIS	58
5.1 Chapter overview	58
5.2 Forms for first, second and third order series approximations	58
5.3 Agreement of first order R_{PP} with expression of Russell and Gray	60
5.4 Importance of low-order nonlinear poroelastic AVO: numerical study	62
5.5 Chapter summary	75
CHAPTER SIX: TOWARDS A MORE COMPLETE PICTURE OF POROELASTICITY	76
6.1 Chapter overview	76
6.2 An introduction to the Gurevich study	76
6.3 Reflection and transmission coefficients for porous-porous media.....	78
6.4 Reflection and transmission coefficients for free fluid-porous media.....	83
6.5 Chapter summary	86
CHAPTER SEVEN: CONCLUSIONS	87
7.1 Summary	87
7.1.1 Review of AVO poroelasticity	87
7.1.2 Exact expressions for poroelastic R_{PP} , R_{PS} , R_{SS} , R_{SP}	88
7.1.3 Series solutions for poroelastic R_{PP}	89
7.1.4 Analytic and numerical validation.....	90
7.1.5 Dynamic poroelasticity.....	91
7.2 Key outcomes of the study.....	95
7.3 Future directions	96
7.3.1 Synthetic data	96
7.3.2 Physical model data	97
7.3.3 Field data	98
7.3.4 Generalization to dynamic poroelasticity	98
7.3.5 Generalization to full poroelastic scattering.....	98
REFERENCES	103
APPENDIX A: POROELASTIC WEIGHTING FACTORS.....	109

List of Tables

Table 2.1: Top layer parameters for six Zoeppritz models from Richards (1961) for Paleozoic limestone structures in Western Canada. The parameters for the bottom layer are $V_P = 6096$ m/s, $V_S = 3048$ m/s, and $\rho = 2650$ kg/m ³	17
Table 2.2: Parameters for Zoeppritz models from Figure (2.2).	22
Table 5.1: Perturbation values from Figure (5.1).	66
Table 5.2: Reflectivity values from Figure (5.2).	67
Table 5.3: Values for perturbation and reflectivity for Figure (5.3).	69
Table 5.4: Values for perturbation and reflectivity for Figure (5.4).	71
Table 5.5: Values for perturbation and reflectivity for Figure (5.5).	73
Table 5.6: Values for perturbation and reflectivity for Figure (5.6).	75

List of Figures and Illustrations

Figure 1.1: A snapshot in time of a source emitting spherical wave fronts.....	5
Figure 1.2: The result of the wave field interacting with the boundary is a reflected wave field that is recorded by the receiver and a transmitted wave field that continues to travel downward into the subsurface.	5
Figure 1.3: This encapsulates all paths that a P-wave may take, which includes the incident, reflected, and transmitted wave. The dotted line is perpendicular to the boundary.	7
Figure 1.4: A simplified two-layer geological representation with an incident P-wave approaching an interface. As the incident P-wave, P^0_{inc} , propagates toward the boundary at $\theta > 0$, a set of P- and S-waves will reflect off of the boundary and another set of P- and S-waves will transmit through the boundary into medium 1. The angles measured from normal for the two reflected and the two transmitted waves all obey Snell's law.....	10
Figure 2.1: Zoeppritz curves of various P- velocities, S- velocities and densities using values from Table (2.1).	18
Figure 2.2: P-wave reflection coefficient versus incident angle for model parameters given in Table (2.2). Figures (a) and (b) show a varying Poisson ratio in the second medium, (c) and (e) show a varying Poisson ratio in the first medium, (d) shows varying values of Poisson's ratio that are equal in both half-spaces, (f) shows varying values of Poisson's ratio that are equal in both half-spaces, and (g) shows varying values of the P-wave velocity contrast (Castagna and Backus, 1993).	21
Figure 3.1: Illustration of all of the wave fields that are generated from incident plane waves. The short arrows indicate particle motion.....	30
Figure 4.1: These plots compare the exact series solutions (blue) with the linear R_{PP} solution that uses $(\gamma_1)_{dry}^2$ (red) and the linear R_{PP} solution that uses $(\gamma_0)_{dry}^2$ (black).....	57
Figure 5.1: All four panels have a consistent perturbation each in a_f , a_μ , and a_ρ . Four curves are produced in each panel: the blue curve represents the exact solutions while the solid, dashed, and dash-dotted black curves represent the 1 st , 2 nd , and 3 rd order approximations respectively.	66
Figure 5.2: The four panels use a consistent reflectivity of $\Delta f/f$, $\Delta\mu/\mu$, and $\Delta\rho/\rho$ in each. Four curves are reproduced in each panel: the blue curve represents the exact solutions while the solid, dashed, and dash-dotted black curves represent the 1 st , 2 nd , and 3 rd order approximations respectively.	67
Figure 5.3: Figures (a), (c), and (e) represent the perturbation based poroelastic AVO approximations of 1 st , 2 nd , and 3 rd order, as shown by the solid, dashed, and dash-dotted black curves respectively. Figures (b), (d), and (f) represent the reflectivity based	

poroelastic AVO approximations of 1st, 2nd, and 3rd order, as shown by the solid, dashed, and dash-dotted black curves respectively. The exact amplitudes are shown by the blue curve..... 68

Figure 5.4: Figures (a), (c), and (e) represent the perturbation based poroelastic AVO approximations of 1st, 2nd, and 3rd order, as shown by the solid, dashed, and dash-dotted black curves respectively. Figures (b), (d), and (f) represent the reflectivity based poroelastic AVO approximations of 1st, 2nd, and 3rd order, as shown by the solid, dashed, and dash-dotted black curves respectively. The exact amplitudes are shown by the blue curve..... 70

Figure 5.5: Figures (a), (c), and (e) represent the perturbation based poroelastic AVO approximations of 1st, 2nd, and 3rd order, as shown by the solid, dashed, and dash-dotted black curves respectively. Figures (b), (d), and (f) represent the reflectivity based poroelastic AVO approximations of 1st, 2nd, and 3rd order, as shown by the solid, dashed, and dash-dotted black curves respectively. The exact amplitudes are shown by the blue curve..... 72

Figure 5.6: Figures (a), (c), and (e) represent the perturbation based poroelastic AVO approximations of 1st, 2nd, and 3rd order, as shown by the solid, dashed, and dash-dotted black curves respectively. Figures (b), (d), and (f) represent the reflectivity based poroelastic AVO approximations of 1st, 2nd, and 3rd order, as shown by the solid, dashed, and dash-dotted black curves respectively. The exact amplitudes are shown by the blue curve..... 74

Figure 6.1: A representation of an incoming P-wave in layer b. The reflection and transmission coefficients are for P-waves only and the subscripts indicate a fast P-wave (1) and Biot's slow wave (2)..... 79

Figure 6.2: A second representation of an incoming P-wave in a free fluid occupying layer b. The reflection and transmission coefficients are for P-waves only and the subscripts indicate a fast P-wave (1) and Biot's slow wave (2)..... 84

List of Symbols, Abbreviations and Nomenclature

Symbol	Definition
AVO	Amplitude variation with offset
AVAZ	Amplitude variation with azimuth
R_P	P-wave normal incidence reflectivity
R_S	S-wave normal incidence reflectivity
θ	P-wave incidence angle
SV	Vertically polarized shear wave
SH	Horizontally polarized shear wave
R_{PP}	Amplitude of reflected P-wave
R_{PS}	Amplitude of reflected S-wave
T_{PP}	Amplitude of transmitted P-wave
T_{PS}	Amplitude of transmitted S-wave
V_P	P-wave velocity
V_S	S-wave velocity
ρ	Density
γ	Compressional-to-shear wave velocity ratio
λ	Lamé's constant
μ	Shear modulus
K	Bulk modulus
$f - m - r$	Fluid-mu-rho
f	Fluid
σ	Poisson's ratio
WIFF	Wave-induced fluid flow
CO ₂	Carbon dioxide
α	Biot coefficient
M	Fluid modulus
ϕ	Porosity
P_I	Incidence P-wave displacement amplitude approaching the boundary from above
P_R	Reflected P-wave displacement amplitude moving away from the boundary
P_T	Transmitted P-wave displacement amplitude moving away from the boundary
S_I	Incidence S-wave displacement amplitude approaching the boundary from above
S_R	Reflected S-wave displacement amplitude moving away from the boundary
S_T	Transmitted S-wave displacement amplitude moving away from the boundary
P'_I	Incidence P-wave displacement amplitude approaching the boundary from below
S'_I	Incidence S-wave displacement amplitude approaching the boundary from below
P	Matrix representation of P-wave Zoeppritz

	equations elements
\mathbf{m}_P	Vector representation of P-wave Zoeppritz equations elements
\mathbf{S}	Matrix representation of S-wave Zoeppritz equations elements
\mathbf{m}_S	Vector representation of S-wave Zoeppritz equations elements
A_{ij}	P-wave Zoeppritz element in \mathbf{P}
B_{ij}	S-wave Zoeppritz element in \mathbf{S}
a_i	P-wave Zoeppritz element in \mathbf{m}_P
b_i	S-wave Zoeppritz element in \mathbf{m}_S
a_f	Fluid perturbation
a_μ	Shear modulus perturbation
a_ρ	Density perturbation
$\Delta f/f$	Fluid reflectivity
$\Delta\mu/\mu$	Shear modulus reflectivity
$\Delta\rho/\rho$	Density reflectivity
ω	Angular frequency
ω_c	Biot's characteristic frequency
η	Steady-state shear viscosity
κ	Permeability
ρ_f	Density of pore fluid
R_{11}	Normal incidence reflection coefficient for fast P-waves
R_{12}	Normal incidence reflection coefficient for Biot slow waves
T_{11}	Normal incidence transmission coefficient for fast P-waves
T_{12}	Normal incidence transmission coefficient for Biot slow waves
$\nabla \cdot$	Divergence operator
Δ^2	Laplacian
$\mathbf{L}_P(\mathbf{r}, \omega)$	Scattered field operator
\mathbf{r}	Spatial coordinates in x, y, z
\mathbf{V}_P	Scattering potential
\mathbf{G}	Green's function
\mathbf{G}_0	Unperturbed Green's function
\mathbf{u}	Displacement of the solid
\mathbf{u}_0	Displacement of the solid in an unperturbed state
\mathbf{w}	Displacement of the fluid relative to the solid
\mathbf{w}_0	Displacement of the fluid relative to the solid in an unperturbed state
\mathbf{F}	Source signature term
\mathbf{f}	Source signature term
δ	Difference

Chapter One: Introduction

1.1 Statement of the problem

AVO analysis and inversion remain a key part of seismic exploration and monitoring. Extensive mathematical analysis of isotropic-elastic AVO equations has been undertaken, in exact forms (Zoeppritz, 1919; Aki and Richards, 1980), linear forms (Richards and Frasier, 1976; Wiggins et al., 1983; Gray et al., 1999) and nonlinear series expansions (Stovas and Ursin, 2001; Innanen 2013). This has been extended to anisotropic AVAZ (Mahmoudian, 2013) and anelastic media (Innanen, 2011a).

Seismic responses in poroelastic media (Biot, 1941; Gassmann, 1951) have been studied in great detail numerically (Carcione et al., 2010; Moradi and Lawton, 2013) and analytically (Gurevich et al., 2004; Müller et al., 2010); the poroelastic model appears to capture geological features of reservoirs very effectively.

Partly in response to a new range of re-parameterization of the linearized AVO equation (Goodway et al., 1997), Russell and Gray formulated linearized poroelastic AVO, through which the amplitude responses in reflection seismic experiments could be related to poroelastic properties such as the Biot fluid term (Russell et al., 2003, 2011). At present, neither exact, nor nonlinear series exist for the Russell and Gray equation; nor is known the importance of AVO nonlinearity with respect to Biot's fluid term.

1.2 Concepts, terms and technical overview

Amplitude variation with offset (AVO) analysis of seismic reflections has become an important tool for hydrocarbon prospecting (Foster et al., 2010). Various AVO parameterizations exist, all of which involve the sum of three weighted elastic-constant terms (Russell et al., 2011).

Zoeppritz (1919) has provided a set of equations that accurately calculates the amplitudes for reflected and transmitted plane waves. These amplitudes can be calculated for a range of offsets in a surface seismic survey.

Various AVO case studies have been investigated in the last several decades. One of the earlier case studies involving Koefoed (1955) shows the effects of using differing Poisson ratios and their impact on the angle-dependent P-wave reflection coefficient. This caused significant angle-dependent variation in the P-wave reflection coefficient (Foster et al., 2010). Other types of hydrocarbon-related AVO responses are identified by Rutherford and Williams (1989), who consider the effects of acoustic-impedance contrasts. They describe the seismic AVO response of gas sands, which have a similar or higher acoustic impedance than the encasing shales. Their work has led to a classification system for AVO responses that has been universally adopted for oil and gas exploration (Foster et al. 2010).

Prior to the wide use of AVO, seismic signals were conventionally viewed as a band-limited normal incidence reflection coefficient series with appropriate traveltimes and amplitude variation due to propagation through an overburden (Castagna and Backus, 1993). Ostrander (1982) demonstrated that gas sand reflection coefficients vary in an anomalous fashion with increasing

offset and showed how to utilize this anomalous behaviour as a direct hydrocarbon indicator on real data (Castagna and Backus, 1993).

The recognition that hydrocarbons affect the acoustic impedance and Poisson's ratio of reservoir sandstones led to the development of seismic attributes to detect these effects (Foster et al. 2010). Some common AVO attributes are the reflection-coefficient intercept or normal-incidence reflection coefficient A ; the reflection-coefficient gradient at normal incidence B ; P-wave normal-incidence reflectivity R_P , which is equivalent to intercept A ; and S-wave normal-incidence reflectivity R_S . Most of these attributes originate with Aki and Richards' (1980) approximation for the angle-dependent P-wave reflection coefficient (Foster et al. 2010).

In this chapter, the following topics will be discussed. The first topic will discuss elementary wave field behaviour for plane waves and the two modes that exist when traveling in a homogenous medium. As plane waves travel in a homogeneous medium and are disturbed by a boundary, reflected and transmitted plane waves are formed as a result where the amplitudes of these waves can be exactly calculated by what is known as the Zoeppritz equations. This will be explained in a brief introduction to how these equations appear in analytical notation as well as the numerous associated linearized approximations. One such approximation has been developed by Russell et al. (2011) and will be discussed in more detail.

1.2.1 Elementary wave field behaviour

When a source located on the surface becomes active, a mechanical disturbance begins to propagate through the subsurface. This is seen in Figure (1.1) where a source has become active

and a series of spherical wave fronts are propagating towards a boundary. For a homogeneous medium, the wave fronts remain spherical given that there are no effects such as anisotropy distorting the overall character of the wave. After a wave front interacts with the boundary, a reflection and a transmission of that wave front will occur. The amplitudes of these wave fronts change depending on the relative change in medium properties. If changes are small, the amplitudes are also small, while large changes produce large amplitudes.

Once the down-going waves emitted from the source have interacted with the boundary separating the two media, a series of reflected and transmitted wave fronts will be generated continuously until the energy dissipates. These two waves are shown in Figure (1.2) where some of the energy acting as up-going wave fronts in the beige medium travels back towards the surface while the rest of the energy continues to travel down. For each down-going wave front that interacts with the boundary, an associated up-going and a transmitted wave front are produced, which accounts for the total of three wave fronts in this simple geological system.

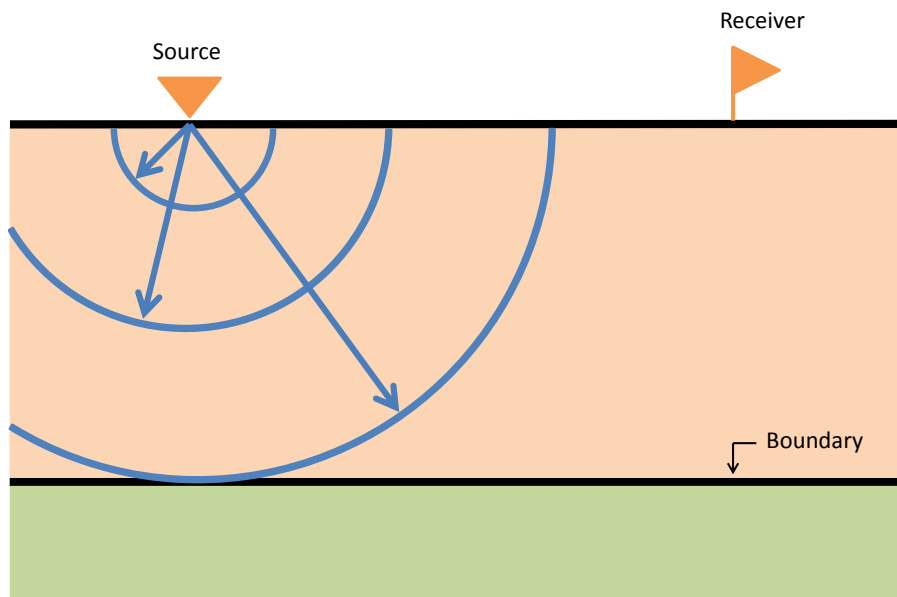


Figure 1.1: A snapshot in time of a source emitting spherical wave fronts.

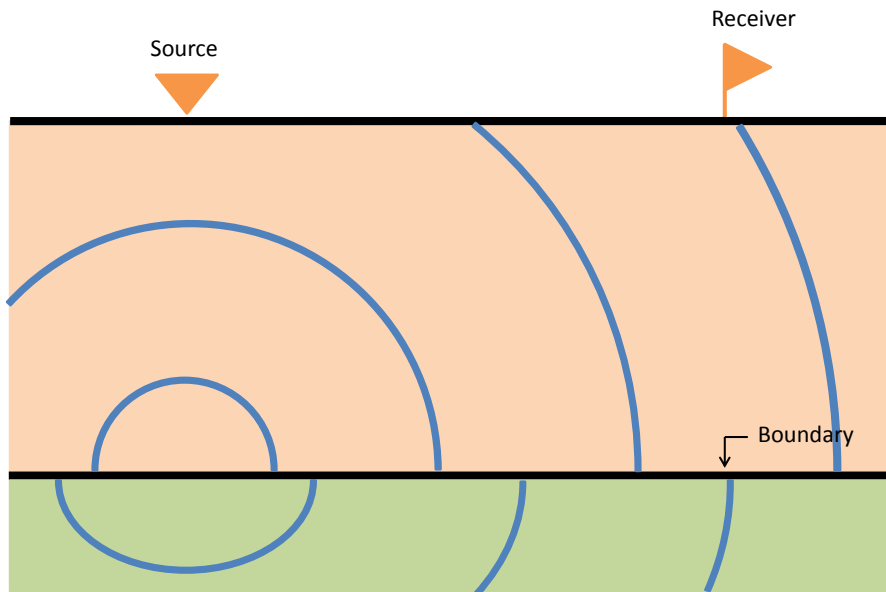


Figure 1.2: The result of the wave field interacting with the boundary is a reflected wave field that is recorded by the receiver and a transmitted wave field that continues to travel downward into the subsurface.

In terms of computer modeling, spherical wave modeling as shown in Figures (1.1) and (1.2) can be time consuming. Plane wave modeling, and more specifically plane wave amplitude

modeling, is useful to approximate spherical wave field amplitudes for several linearized P-wave amplitude modeling equations, as will be demonstrated later in this chapter.

In Figure (1.3) a single P-wave ray path is demonstrated. It shows a down-going P-wave which strikes the boundary at a particular incidence angle θ . The angle θ in relation to the reflected and transmitted angles is shown by Snell's law. Another form of a plane wave is the S-wave which is also generated by the source if it is given a shear motion. These waves propagate at a velocity different than their P- counterparts. As either P- or S-waves interact with a boundary, mode conversion occurs which produces both P- and S-waves that propagate as a reflected wave and a transmitted wave as illustrated in Figure (1.4). The Zoeppritz equations describe how these relationships hold based on conservation of reflection and transmission amplitudes for plane waves. More specifically, the Zoeppritz equations are useful in describing the vector orientation of the plane wave with its amplitude. For this study, primary interest is in the P-wave amplitude signature that the wave field carries as it travels from the source to a reflecting boundary, and to a receiver as seen in Figure (1.3).

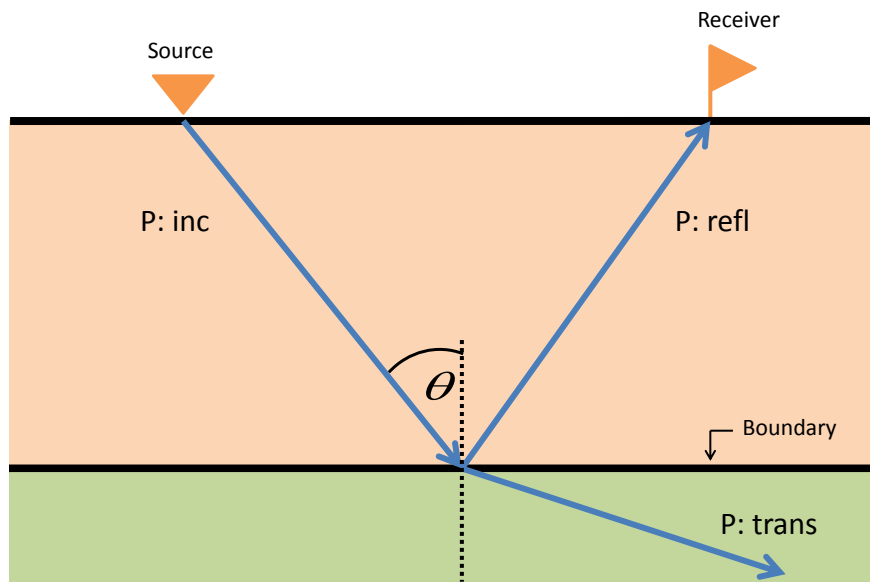


Figure 1.3: This encapsulates all paths that a P-wave may take, which includes the incident, reflected, and transmitted wave. The dotted line is perpendicular to the boundary.

The Zoeppritz equations will be used as the starting point for our study. As mentioned previously, the incoming P-wave approaches the boundary at a particular angle θ . When $0^\circ < \theta < 90^\circ$, a reflected and transmitted P-wave is produced. The direction and the amplitude of the reflected and transmitted waves are based on two factors: the elastic contrasts between the upper and lower geological layer, and the incident angle θ . These factors are explicitly shown in the Zoeppritz equations which quantify the amplitudes of these P- and S-waves. More details about the Zoeppritz equations will be explained in the subsection.

1.2.2 Reflection at a boundary: AVO and the Zoeppritz equations

A simple model that is considered for studying reflection amplitudes may consist of two semi-infinite isotropic homogeneous half-spaces that are welded together at a plane interface or boundary. For an incident plane wave traveling within this model, the reflection coefficient

variation with an angle of incidence is given by the Zoeppritz equations (Castagna et al. 1998). Due to the complex structure of these equations, approximations (Bortfeld, 1961; Richards and Frasier, 1976; Aki and Richards, 1980; Shuey, 1985) have been derived to simplify the calculation of the reflection coefficient (Castagna et al. 1998). Before discussing the approximations, the Zoeppritz equations will be described in more detail.

A P-wave that strikes a planar interface between two elastic solids gives rise to four other plane waves: the reflected vertically polarized shear (SV) wave, the reflected P-wave, the transmitted P-wave, and the transmitted SV-wave as shown in Figure (1.4) (Keys, 1989). Since the horizontally polarized shear (SH) wave is not calculated in the Zoeppritz equations, the shear wave will be referred to as the S-wave.

The amplitudes of these plane waves are related to one another by the requirement that normal and tangential components of stress and displacement must be continuous across the reflecting interface (Keys, 1989). From these continuity conditions, a set of four equations for the four P-wave displacement amplitudes can be derived:

$$\begin{bmatrix} -X & -\sqrt{1-B^2X^2} & CX & -\sqrt{1-D^2X^2} \\ \sqrt{1-X^2} & -BX & \sqrt{1-C^2X^2} & DX \\ 2B^2X\sqrt{1-X^2} & B(1-2B^2X^2) & 2AD^2X\sqrt{1-C^2X^2} & -AD(1-2D^2X^2) \\ -(1-2B^2X^2) & 2B^2X\sqrt{1-B^2X^2} & AC(1-2D^2X^2) & 2AD^2X\sqrt{1-D^2X^2} \end{bmatrix} \begin{bmatrix} R_{PP} \\ R_{PS} \\ T_{PP} \\ T_{PS} \end{bmatrix} = \begin{bmatrix} X \\ \sqrt{1-X^2} \\ 2B^2X\sqrt{1-X^2} \\ 1-2B^2X^2 \end{bmatrix} \quad (1.1)$$

where R_{PP} is the amplitude of the reflected P-wave, R_{PS} is the amplitude of the reflected S-wave, T_{PP} is the amplitude of the transmitted P-wave, and T_{PS} is the amplitude of the transmitted S-wave (Keys, 1989). The variable X is $\sin \theta_0$, where θ_0 is the angle of incidence. A , B , C , and D

represent ratios of the elastic parameters: $A = \rho_1/\rho_0$, $B = V_{S_0}/V_{P_0}$, $C = V_{P_1}/V_{P_0}$, and $D = V_{S_1}/V_{P_0}$, where ρ_i , V_{P_i} , and V_{S_i} are the density, P-wave velocity and S-wave velocity of medium i , respectively. Equation (1.1) is equivalent to the Zoeppritz equations used by Levin (1986).

By observing the interaction of a plane wave upon an interface of two semi-infinite half spaces, four different energy partitions result from an incident P-wave. These partitions are (1) a reflected P-wave, (2) a transmitted P-wave, (3) a reflected S-wave, and (4) a transmitted S-wave (Castagna and Backus, 1993). The angles of each partition may be calculated using Snell's law,

$$p = \frac{\sin \theta_0}{V_{P_0}} = \frac{\sin \theta_1}{V_{P_1}} = \frac{\sin \phi_0}{V_{S_0}} = \frac{\sin \phi_1}{V_{S_1}},$$

where, V_{P_0} and V_{P_1} are the P-wave velocities in medium 0 and medium 1, respectively; V_{S_0} and V_{S_1} are the S-wave velocities in medium 0 and medium 1, respectively; θ_0 and θ_1 are the incident P-wave angle, and the transmitted P-wave angle, respectively; ϕ_0 and ϕ_1 are the reflected S-wave angle, and the transmitted S-wave angle, respectively; finally p is the ray parameter. This is illustrated in Figure (1.4).

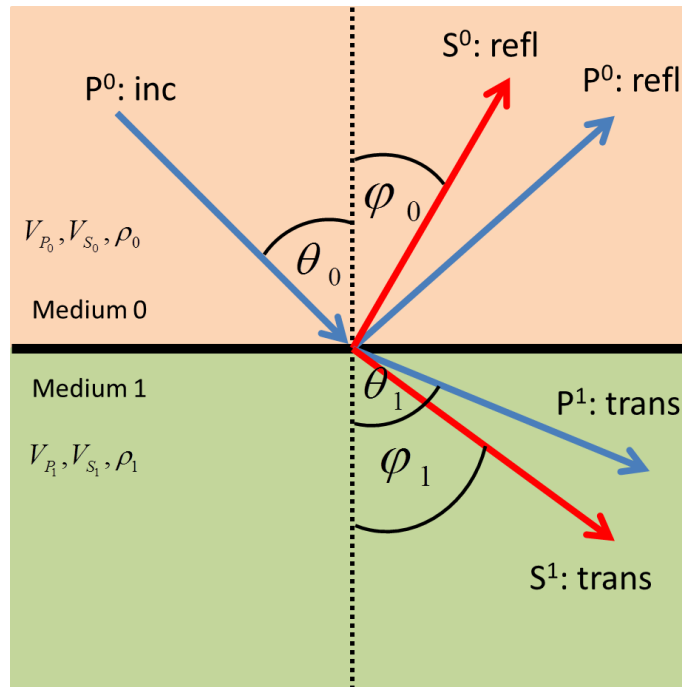


Figure 1.4: A simplified two-layer geological representation with an incident P-wave approaching an interface. As the incident P-wave, $P^0: \text{inc}$, propagates toward the boundary at $\theta > 0$, a set of P- and S-waves will reflect off of the boundary and another set of P- and S-waves will transmit through the boundary into medium 1. The angles measured from normal for the two reflected and the two transmitted waves all obey Snell's law.

1.3 AVO analysis

1.3.1 Development of seismic amplitude analysis

In literature, many studies demonstrate linearized AVO equations that approximate the Zoeppritz equations. These linearized equations extract physical information from amplitude data directly (Shuey, 1985; Aki and Richards, 2002; Smith and Gidlow, 1987; Rutherford and Williams, 1989).

The Zoeppritz equations describe the relations of incident, reflected and transmitted longitudinal waves (P-waves) and shear waves (S-waves) on both sides of an interface (Smith and Gidlow,

1987). These equations are the fundamental mathematical formulae for the amplitudes of reflected and transmitted plane waves when an incident P-wave strikes an elastic boundary. Although they give precise values of the amplitudes of the reflected and transmitted plane waves, they may cause problems. For instance, the effects of parameter changes on the seismic amplitudes and the unstable solution that may result from the intrinsic nonlinearity of these equations make it less practical than are linearized approximations to them (Zong et al., 2012).

For analysis of P-wave reflections, the requirement is an equation which relates reflected P-wave amplitudes to incident P-wave amplitudes as a function of the angle of incidence (Smith and Gidlow, 1987). Following Russell et al. (2011), the Aki and Richards approximation is expressed as a linearized sum of three terms given by

$$R_{pp}(\theta) \approx (1 + \tan^2 \theta) \frac{\Delta V_P}{2V_P} + \left(\frac{-8 \sin^2 \theta}{\gamma_{sat}^2} \right) \frac{\Delta V_S}{2V_S} + \left(1 - \frac{4 \sin^2 \theta}{\gamma_{sat}^2} \right) \frac{\Delta \rho}{2\rho} \quad (1.2)$$

where V_P , V_S , and ρ are the average velocity and density values across the boundary; ΔV_P , ΔV_S , and $\Delta \rho$ are the differences of the velocity and density values across the boundary; θ is interpretable as either the incidence angle or the average of the incident and refracted angles; and $\gamma_{sat} = (V_P/V_S)_{sat}$ is the compressional-to-shear-wave velocity ratio for the *in situ* (saturated) rocks (Russell et al. 2011). An assumption is made such that the relative changes of property ($\Delta V_P/2V_P$, $\Delta V_S/2V_S$, $\Delta \rho/2\rho$) are sufficiently small that second-order terms can be neglected and that θ does not approach the critical angle or 90° (Smith and Gidlow, 1987).

Several important algebraic rearrangements of equation (1.2) exist, the most common being

$$R_{pp}(\theta) \approx A + B \sin^2 \theta + C \tan^2 \theta \sin^2 \theta \quad (1.3)$$

where $A = R_{P0} = \frac{1}{2} \left[\frac{\Delta V_P}{V_P} + \frac{\Delta \rho}{\rho} \right]$ is a linearized approximation to the zero offset P-wave reflection coefficient, $B = \frac{\Delta V_P}{2V_P} - \frac{8}{\gamma_{\text{sat}}^2} \frac{\Delta V_S}{2V_S} - \frac{4}{\gamma_{\text{sat}}^2} \frac{\Delta \rho}{2\rho}$, and $C = \frac{\Delta V_P}{2V_P}$ (Russell et al., 2011). Equation (1.3) is initially derived by Wiggins et al. (1983), and is the basis of much empirical AVO work (Russell et al., 2011).

A second rearrangement of equation (1.3), by Gidlow et al. (1992) and Fatti et al. (1994), based on an earlier equation by Smith and Gidlow (1987), is given by

$$R_{\text{PP}}(\theta) \approx (1 + \tan^2 \theta) R_{P0} + \left(-\frac{8}{\gamma_{\text{sat}}^2} \sin^2 \theta \right) R_{S0} + \left(\frac{4}{\gamma_{\text{sat}}^2} \sin^2 \theta - \tan^2 \theta \right) R_D \quad (1.4)$$

where $R_{P0} = \frac{1}{2} \left[\frac{\Delta V_P}{V_P} + \frac{\Delta \rho}{\rho} \right]$ is equal to the A term from equation (1.3), $R_{S0} = \frac{1}{2} \left[\frac{\Delta V_S}{V_S} + \frac{\Delta \rho}{\rho} \right]$ is the linearized approximation to the S-wave impedance reflectivity, and $R_D = \frac{\Delta \rho}{2\rho}$ is the linearized density reflectivity term (Russell et al., 2011). More recently, Gray et al. (1999) reformulated equation (1.3) for two sets of fundamental constants: λ , μ , and ρ (the first and second Lamé parameters and density, respectively), and K , μ , and ρ (bulk modulus, shear modulus, and density respectively) (Russell et al., 2011). Gray et al.'s (1999) two formulations are given as

$$R_{\text{PP}}(\theta) \approx \left(\frac{1}{4} - \frac{1}{2\gamma_{\text{sat}}^2} \right) \sec^2 \theta \frac{\Delta \lambda}{\lambda} + \frac{1}{\gamma_{\text{sat}}^2} \left(\frac{1}{2} \sec^2 \theta - 2 \sin^2 \theta \right) \frac{\Delta \mu}{\mu} + \left(\frac{1}{2} - \frac{1}{4} \sec^2 \theta \right) \frac{\Delta \rho}{\rho}, \quad (1.5)$$

and

$$R_{pp}(\theta) \approx \left(\frac{1}{4} - \frac{1}{3\gamma_{sat}^2} \right) \sec^2 \theta \frac{\Delta K}{K} + \frac{1}{\gamma_{sat}^2} \left(\frac{1}{3} \sec^2 \theta - 2 \sin^2 \theta \right) \frac{\Delta \mu}{\mu} + \left(\frac{1}{2} - \frac{1}{4} \sec^2 \theta \right) \frac{\Delta \rho}{\rho}. \quad (1.6)$$

1.3.2 Fluid discrimination from AVO analysis

The development of methods to obtain various fluid factors from prestack seismic data has pushed the development of technology for reservoir forecasting and fluid discrimination (Smith and Gidlow, 2000; Quakenbush et al., 2006; Zong et al., 2012). Traditional AVO and petrophysical analysis seeks to identify anomalous variations between seismic compressional wave velocity (V_p) and shear wave velocity (V_s) to indicate changes primarily in pore fluid, as well as lithologic properties (Goodway et al., 1997; Gassmann, 1951; Pickett, 1963; Tatham, 1982; Castagna, 1993). The $\lambda - \mu - \rho$ parameterization is presented by Goodway et al. (1997) that show an alternate way to extract the parameters suggested (Russell et al., 2011).

Gray et al. (1999) derive two formulas which parameterize AVO in terms of constants λ , μ , and ρ (Lamé moduli, shear modulus, and density) for the first formula, and K , μ , and ρ (bulk modulus, shear modulus, and density) for the second formula in equations (1.5) and (1.6) (Russell et al. 2011). It is the combination of the $\lambda - \mu - \rho$ technique and Gray's AVO formulations that motivated the linear poroelastic AVO derivation by Russell et al. (2011). Russell et al. (2011) refer to this equation as the $f - m - r$ equation. An additional linearized poroelastic AVO equation is derived by Zong et al. (2012) parameterized in terms of P-wave modulus, S-wave modulus, and dry velocity ratio.

Interpreted in the context of Biot (1941) and Gassmann (1951) theory, the Russell et al. (2011) linearized poroelastic AVO equation accounts for gas-filled pore space contributions. Russell et al. (2011) derived the $f - m - r$ equation beginning with the linear elastic form in equation (1.2). One of our goals will be to re-derive $f - m - r$ beginning with a re-parameterization of the full Zoeppritz equations.

1.4 Thesis overview

As mentioned in the statement of the problem, there are no cited investigations that reveal exact solutions or nonlinear series solutions in regards to PP reflection modeling of poroelastic inclusions in geological settings.

However, the research of exact reflection modeling is available in great detail (Zoeppritz, 1919; Keys, 1989; Levin, 1986) and there are also instances found in the literature that portray different parameterizations of PP reflection modeling as linearized approximations (Aki and Richards, 2002; Shuey, 1985) as well as nonlinear series solutions (Innanen, 2013). In regards to geological settings that include pore fluids, there is also research by Biot (1941) and Gassmann (1951) that illustrate how the introduction of these pore fluids affect an initially dry (or drained) porous rock. More recently, a study has been performed in regards to poroelastic media using reflection modeling. Russell et al. (2011) show that a derivation of a linearized AVO equation of poroelastic environments can be quantitatively measured with three poroelastic parameters; the first is known as the fluid term (f), the second is a saturated shear modulus (μ) and the third, a saturated density (ρ) term. The contents of this thesis will explain how it is possible to use these poroelastic parameters (f, μ, ρ) to derive both exact and nonlinear series solutions using the

exact-elastic reflection modeling or Zoeppritz modeling as an extension to the research of Russell et al. (2011).

At the beginning of chapters two, three, four, five and six, an overview will state the purpose of that chapter in a section by section basis. These chapters will be concluded with a summary that will mention the main result or observation and transition to the following chapter. Chapter seven is the conclusions chapter and will summarize the thesis in addition to providing the key results and the future directions of this work.

Chapter Two: Theoretical Background

2.1 Chapter overview

The purpose of this chapter is to introduce concepts of AVO theory. In section 2.2 we will review two studies using exact AVO modeling followed by an issue that is found using these exact AVO equations. The section will conclude with several forms of linearized AVO equations. Section 2.3 will introduce poroelasticity using Biot's fluid term to describe how elastic moduli may be written analytically to compensate for the effect of a fluid. This will lead into the Russell and Gray AVO approximation that uses Biot's fluid term as one of its parameters in section 2.4. Finally, chapter 2 will be summarized in section 2.5.

2.2 The Zoeppritz equations in a geological setting

2.2.1 Case study applications of exact solutions

The P-wave reflection coefficient as a function of incidence angle $R_{PP}(\theta_0)$ is defined as the ratio of the amplitude of the reflected P-wave to that of the incident P-wave (Castagna and Backus, 1993). Similarly, the P-wave transmission coefficient $T_{PP}(\theta_0)$ is the ratio of the amplitude of the transmitted P-wave to that of the incident P-wave. Also, $R_{PS}(\theta_0)$ is the ratio of the amplitudes of the reflected S-wave and the incident P-wave and $T_{PS}(\theta_0)$ is the ratio of the transmitted S-wave and incident P-wave amplitudes (Castagna and Backus, 1993). Knott (1899) and Zoeppritz (1919) invoked continuity of displacement and stress at the reflecting interface as boundary conditions to solve for the reflection and transmission coefficients as a function of the incident angle and the media elastic properties (density, bulk modulus and shear modulus) (Castagna and Backus, 1993). The result is a set of equations known as the Zoeppritz equations.

The Zoeppritz equations are very complex and involve instances of rational expressions that yield real and complex valued reflection and transmission coefficients. This kind of complexity provides little physical insight (Castagna and Backus, 1993). The coefficients R_{PP} , R_{PS} , T_{PP} , and T_{PS} as a function of θ_0 , are computed from the P-wave velocity, S-wave velocity, and density of each medium. Figure (2.1) provides reflection coefficient values for PP waves for various velocities and densities (Castagna and Backus, 1993). These velocities and densities are shown in Table (2.1).

Overburden Model	V_P (m/s)	V_S (m/s)	ρ (kg/m ³)
A	1829	914	2020
B	2521	1260	2120
C	3048	1524	2200
D	4267	2133	2380
E	4877	2438	2470
F	5486	2743	2560

Table 2.1: Top layer parameters for six Zoeppritz models from Richards (1961) for Paleozoic limestone structures in Western Canada. The parameters for the bottom layer are $V_P = 6096$ m/s, $V_S = 3048$ m/s, and $\rho = 2650$ kg/m³.

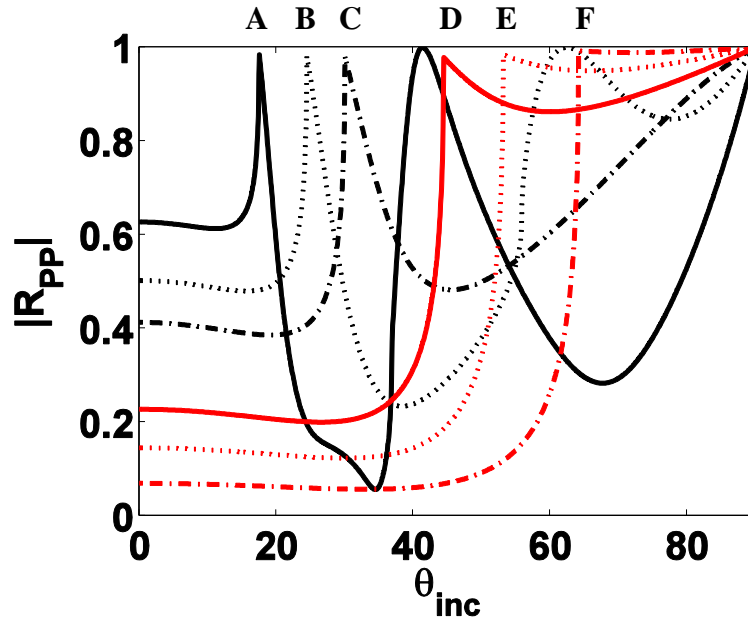


Figure 2.1: Zoeppritz curves of various P- velocities, S- velocities and densities using values from Table (2.1).

Figure (2.1) shows the entire range of possible incidence angles, whereas common exploration incidence angles are about 30 degrees or less (Castagna and Backus, 1993). For the AVO curves in this figure, the following observations have been made (Castagna and Backus, 1993):

- (1) The local maxima for reflected P-wave amplitudes may occur at normal incidence, the first critical angle, and possibly near the S-wave critical angle.
- (2) The change of the reflection coefficient with respect to the angle of incidence is small at low angles.
- (3) The first critical angle θ_{c_0} is given by

$$\sin \theta_{c_0} = \frac{V_{P_0}}{V_{P_1}} . \quad (2.1)$$

For elastic layers, the reflected P-wave energy decreases after the first critical angle due to increased conversion to reflected and transmitted S-waves. Consequently, there can be a second critical angle θ_{c_1} given by

$$\sin \theta_{c_1} = \frac{V_{P_0}}{V_{S_1}} . \quad (2.2)$$

Beyond this critical angle there are no transmitted S-waves. From equation (2.1), we can see that there is no first critical angle when V_{P_0} is greater than V_{P_1} . When this occurs, P-waves are always transmitted. In equation (2.2), there is no second critical angle when V_{P_0} is greater than V_{S_1} implying that converted S-waves are transmitted at all angles below 90° . Finally,

- (4) At near normal incidence, R_{pp} initially decreases very slightly with increasing angle. Deviations from this general behaviour can result from changes in V_P/V_S across the interface, and form the basis for seismic lithology analysis.

In exploration seismology, the reflection coefficient is typically desired for pre-critical angles. Koefoed (1955) was first to point out that AVO analysis may be used to identify V_P/V_S variations. His research explored conditions such that V_P/V_S variations, where Poisson's ratio measurements are changing across an interface, may be used as an indicator for hydrocarbon detection (Castagna and Backus, 1993). The relationship of Poisson's ratio to V_P/V_S is

$$\sigma = \frac{\frac{1}{2} \left(\frac{V_P}{V_S} \right)^2 - 1}{\left(\frac{V_P}{V_S} \right)^2 - 1} , \quad (2.3)$$

and

$$\frac{V_s}{V_p} = \sqrt{\frac{1-\sigma}{2-\sigma}}. \quad (2.4)$$

Koefoed's (1955) work is illustrated in Figure (2.2) where varying V_p/V_s ratios and Poisson's ratios are tested. There are several observations that may be made about Figure (2.2) (Castagna and Backus, 1993): (1) Figures (2.2a), (2.2b), and (2.2c) illustrate the basic principle exploited when AVO is used for hydrocarbon detection; as σ_1 decreases (as would occur when gas replaces brine); the reflection coefficient becomes more negative with increasing offset. (2) For $\Delta\sigma = 0$ (Figures (2.2d) and (2.2f)), lowering the average Poisson ratio also causes the reflection coefficient to become more negative with increasing offset. (3) Comparison of Figures (2.2b) and (2.2e) shows that the effect of lowering σ_1 occurs for all V_{P1}/V_{P0} ratios. (4) If V_{P1}/V_{P0} is varied while density and Poisson's ratio remain constant, the magnitude of the AVO effect is essentially unchanged (the AVO curves are shifted by the normal incidence reflection coefficient R_p).

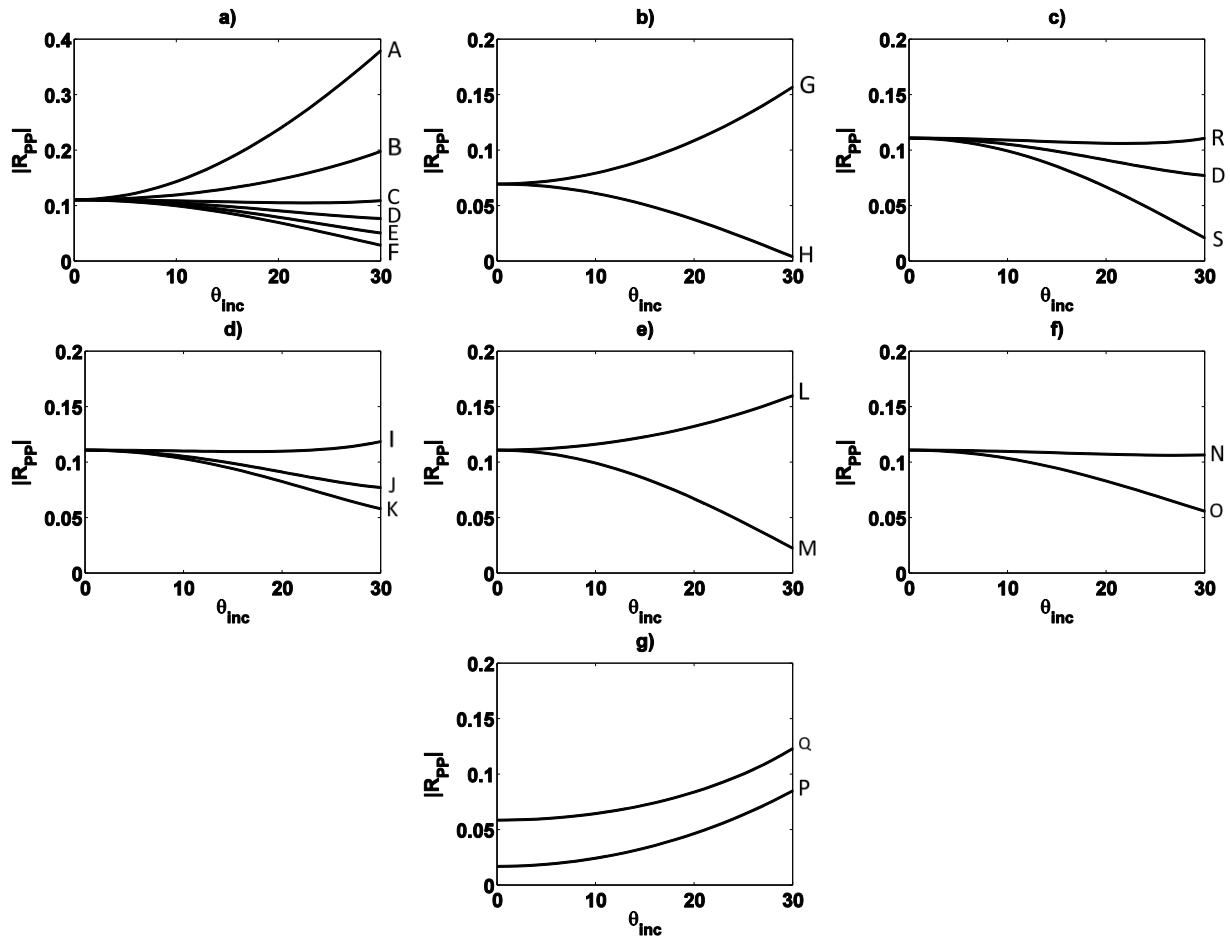


Figure 2.2: P-wave reflection coefficient versus incident angle for model parameters given in Table (2.2). Figures (a) and (b) show a varying Poisson ratio in the second medium, (c) and (e) show a varying Poisson ratio in the first medium, (d) shows varying values of Poisson's ratio that are equal in both half-spaces, (f) shows varying values of Poisson's ratio that are equal in both half-spaces, and (g) shows varying values of the P-wave velocity contrast (Castagna and Backus, 1993).

Model	ρ_1/ρ_0	V_{S_0}/V_{P_0}	V_{P_1}/V_{P_0}	V_{S_1}/V_{P_0}	σ_0	σ_1
A	1.0	0.58	1.25	0.00	0.25	0.50
B	1.0	0.58	1.25	0.51	0.25	0.40
C	1.0	0.58	1.25	0.67	0.25	0.30
D	1.0	0.58	1.25	0.72	0.25	0.25
E	1.0	0.58	1.25	0.76	0.25	0.20
F	1.0	0.58	1.25	0.80	0.25	0.15
G	1.0	0.58	1.15	0.47	0.25	0.40
H	1.0	0.58	1.15	0.74	0.25	0.15
I	1.0	0.41	1.25	0.51	0.40	0.40
J	1.0	0.58	1.25	0.72	0.25	0.25
K	1.0	0.64	1.25	0.80	0.15	0.15
L	1.0	0.41	0.80	0.46	0.40	0.25
M	1.0	0.64	0.80	0.46	0.15	0.25
N	1.0	0.41	0.80	0.33	0.40	0.40
O	1.0	0.64	0.80	0.51	0.15	0.15
P	0.9	0.58	1.15	0.54	0.25	0.36
Q	0.9	0.58	1.25	0.58	0.25	0.36
R	1.0	0.64	1.25	0.72	0.15	0.25
S	1.0	0.41	1.25	0.72	0.40	0.25

Table 2.2: Parameters for Zoeppritz models from Figure (2.2).

2.2.2 Issue with exact solutions

Reflection and transmission coefficients can be found by solving the Zoeppritz equations. Depending on the incident plane wave, two sets of Zoeppritz equations may be derived; one for P-wave and one for S-wave. As shown by Innanen (2013) for incident P-waves in elastic media, an expression in the form of a series is possible for R_{PP} , R_{PS} , T_{PP} or T_{PS} in the Zoeppritz equations. Within Innanen (2013), a four-by-four matrix configuration is shown to represent the weights that are associated with R_{PP} , R_{PS} , T_{PP} and T_{PS} , in this type of representation of the Zoeppritz equations. Either one of R_{PP} , R_{PS} , T_{PP} or T_{PS} may be solved using Cramer's rule. Solving for one of these coefficients using Cramer's rule would result in a series that is very difficult to interpret analytically. Hence, one factor that motivated the development of AVO approximations was to not only have a means to analyze parameter changes more easily, but to also reduce computational costs.

2.2.3 AVO approximations

Approximations are extremely useful for practical applications as they more readily reveal the information content contained in the amplitude behaviour and provide the basis for certain AVO processing techniques (Castagna and Backus, 1993). Bortfeld (1961) linearized the solutions of the Zoeppritz equations by assuming small changes in layer properties and obtained

$$R_{PP}(\theta_0) \approx \frac{1}{2} \ln \left[\frac{V_{P1} \rho_1 \cos \theta_0}{V_{P0} \rho_0 \cos \theta_1} \right] + \left(\frac{\sin \theta_0}{V_{P0}} \right)^2 (V_{S0}^2 - V_{S1}^2) \left[2 + \frac{\ln(\rho_1 / \rho_0)}{\ln(V_{S1} / V_{S0})} \right]. \quad (2.5)$$

The parameters in equation (2.5) are as follows: V_P , V_S , and ρ are the P-wave velocity, S-wave velocity, and density respectively; θ is the incidence angle that the plane wave makes with respect to normal of the interface; and the subscripts '0' and '1' represent the medium above the

interface and the medium below the interface respectively. This approach was also followed by Richards and Frasier (1976) and Aki and Richards (1980) who derived a form parameterized in terms of the changes in density, P-wave velocity, and S-wave velocity across the interface (Castagna and Backus, 1993). The mathematical form of this AVO approximation is shown in chapter 1 equation (1.2). Other AVO approximations appear in the form

$$R_{PP}(\theta_0) = \frac{V_{P_1}\rho_1 \cos \theta_0 - V_{P_0}\rho_0 \cos \theta_1}{V_{P_1}\rho_1 \cos \theta_0 + V_{P_0}\rho_0 \cos \theta_1}, \quad (2.6)$$

which is referred to as the ‘acoustic’ reflection coefficient. Shuey (1985) also presents an AVO approximation that is similar to the Aki and Richards (1980) approximation

$$R_{PP}(\theta_0) \approx R_P + \left(A_0 R_P + \frac{\Delta\sigma}{(1-\sigma)^2} \right) \sin^2 \theta_0 + \frac{1}{2} \frac{\Delta V_P}{V_{P_{avg}}} (\tan^2 \theta_0 - \sin^2 \theta_0), \quad (2.7)$$

where, R_P is the normal incidence reflection coefficient, and A_0 and B_0 are given by

$$A_0 = B_0 - 2(1 + B_0) \left(\frac{1-2\sigma}{1-\sigma} \right), \quad (2.8)$$

and

$$B_0 = \frac{\Delta V_P / V_{P_{avg}}}{\Delta V_P / V_{P_{avg}} + \Delta \rho / \rho_{avg}}. \quad (2.9)$$

2.3 Poroelasticity

Exploration geophysicists are interested in the inelastic attenuation and dispersion of plane waves resulting from the presence of fluids in the pore space of rocks (Müller et al., 2010). It is believed that an understanding of fluid-related dissipation of seismic wave energy in hydrocarbon reservoir rocks, combined with improved measurements of attenuation and/or

dispersion from recorded seismic data, may be used in the future to estimate the hydraulic properties of these rocks (Müller et al., 2010). A major cause of attenuation in porous media is wave-induced fluid flow (WIFF), which occurs at different spatial scales – macroscopic, mesoscopic, and microscopic (Carcione et al., 2010). WIFF occurs as a passing wave creates pressure gradients within the fluid phase and the resulting movement of the fluid relative to the solid (fluid flow) is accompanied with internal friction until the pore pressure is equilibrated (Müller et al., 2010). WIFF's classification depends on the length scale of the pressure gradient (Müller et al., 2010). If a body wave propagates through a spatially homogeneous, permeable, fluid-saturated rock, it will create pressure gradients between peaks and troughs of the wave (Müller et al., 2010).

The theories of poroelasticity are essential in many geophysical applications where pore-filling materials are of interest, e.g., oil exploration, gas-hydrate detection, seismic monitoring of CO₂ storage, and hydrogeology (Carcione et al., 2010). Modern poroelastic theory was introduced by Maurice Biot in the 1950s (e.g., Biot, 1962; Bourbié et al., 1987; Allard, 1993; Carcione, 2007), who obtained the dynamic equations for wave propagation in a fully saturated medium (Carcione et al., 2010). Since Biot presented his work on poroelastic wave theory in the early 1960s, significant research on poroelastic wave propagation has been conducted (Ren et al., 2009). These equations predict the effects of movement of the pore fluid relative to the solid skeleton on seismic waves propagating through the rock (Gurevich et al., 2004). According to Biot's theory, seismic waves propagating in a homogeneous poroelastic medium are not attenuated significantly in the seismic frequency range of 0-200 Hz (Ren et al., 2009).

Russell et al. (2011) make use of these fundamental equations due to Biot (1941), which relate the dry elastic moduli to saturated moduli where

$$\lambda_{\text{sat}} = \lambda_{\text{dry}} + \alpha^2 M , \quad (2.10)$$

$$K_{\text{sat}} = K_{\text{dry}} + \alpha^2 M \quad (2.11)$$

and

$$\mu_{\text{sat}} = \mu_{\text{dry}} . \quad (2.12)$$

Lamé's constant λ , bulk modulus K and shear modulus μ are represented here. These three relationships show how λ , K , and μ can be compensated when fluid is present. The $\alpha^2 M$ term that appears in equations (2.10) and (2.11) is the fluid modulus, the dissipative term corresponding to viscoelastic effects associated with the squeezing of the fluid in the small, crack-like volumes surrounding the areas of contact inside a pore (Biot, 1962). The term α is referred to as the Biot coefficient, and is defined as

$$\alpha = 1 - \frac{K_{\text{dry}}}{K_{\text{m}}} , \quad (2.13)$$

where K_{dry} is the elastic bulk modulus and K_{m} is the bulk modulus of the mineral. The term M is

$$M = \left(\frac{\alpha - \phi}{K_{\text{m}}} + \frac{\phi}{K_{\text{fl}}} \right)^{-1} , \quad (2.14)$$

where α is the Biot coefficient, ϕ is the porosity, and K_{fl} is the bulk modulus of the fluid.

Equations (2.10) – (2.12) can be inserted into the elastic P-wave and S-wave velocity equations in order to account for fluid. For elastic media, expressions for P- and S-wave velocities can be written such that

$$V_p^2 = \frac{\lambda + 2\mu}{\rho} = \frac{K + (4/3)\mu}{\rho} = \frac{s}{\rho}, \quad (2.15)$$

and

$$V_s^2 = \frac{\mu}{\rho}. \quad (2.16)$$

According to Russell et al. (2011), by substituting equations (2.10) – (2.12) into (2.15) and (2.16), the poroelastic expressions for V_p and V_s become

$$(V_p)_{\text{sat}}^2 = \frac{\lambda_{\text{dry}} + 2\mu_{\text{sat}} + \alpha^2 M}{\rho_{\text{sat}}} = \frac{K_{\text{dry}} + (4/3)\mu_{\text{sat}} + \alpha^2 M}{\rho_{\text{sat}}}, \quad (2.17)$$

and

$$(V_s)_{\text{sat}}^2 = \frac{\mu_{\text{sat}}}{\rho_{\text{sat}}}. \quad (2.18)$$

Since equation (2.18) does not include the fluid modulus $\alpha^2 M$, the poroelastic S-wave velocity remains unchanged.

2.4 The Russell-Gray linear poroelastic AVO model

Russell and Gray (Russell et al., 2011), using the foregoing framework, proposed a linearized poroelastic AVO approximation, building on work reported by Russell et al. (2003). Russell et al. (2003) discusses how to obtain fluid from seismic data by showing the lambda-mu-rho technique originally discussed by Goodway et al. (1997). Fundamentally, the lambda-mu-rho technique can extract $\lambda\rho$ and $\mu\rho$ from seismic data by taking the squares and differences of the P and S impedances. Gray et al. (1999) provides two AVO formulations that model the subsurface as either $K - \mu - \rho$ or $\lambda - \mu - \rho$. By combining Gray et al. (1999) and Goodway et al.'s (1997) lambda-mu-rho techniques, Russell et al. (2011) were able to derive a generalized expression for

poroelastic media. That expression is what we will refer to as the Russell and Gray approximation:

$$R_{PP}^{(RG)}(\theta) \approx \left[\left(1 - \frac{\gamma_{\text{dry}}^2}{\gamma_{\text{sat}}^2} \right) \frac{\sec^2 \theta}{4} \right] \frac{\Delta f}{f} + \left[\frac{\gamma_{\text{dry}}^2}{4\gamma_{\text{sat}}^2} \sec^2 \theta - \frac{2}{\gamma_{\text{sat}}^2} \sin^2 \theta \right] \frac{\Delta \mu}{\mu} + \left[\frac{1}{2} - \frac{\sec^2 \theta}{4} \right] \frac{\Delta \rho}{\rho}, \quad (2.19)$$

where θ is the average between the incidence and refracted angle; $\gamma_{\text{sat}} = (V_{P_0} + V_{P_1})_{\text{sat}} / (V_{S_0} + V_{S_1})_{\text{sat}}$ and $\gamma_{\text{dry}} = (V_{P_0} + V_{P_1})_{\text{dry}} / (V_{S_0} + V_{S_1})_{\text{dry}}$; Δf , $\Delta \mu$ and $\Delta \rho$ are the differences in fluid, shear modulus, and density across the interface; and f , μ and ρ are averages.

2.5 Chapter summary

This chapter concludes with the Russell and Gray approximation in equation (2.19). This equation is an approximation of exact AVO that is parameterized in terms of poroelastic properties. Although this equation is linear, it is possible to derive a set of equations that is in kind with the Zoeppritz equations that use the poroelastic parameters f , μ , ρ . Before this is shown, the following chapter will produce the Zoeppritz equations for elastic media such that exact solutions of R_{PP} , R_{PS} , R_{SS} and R_{SP} can be calculated.

Chapter Three: Exact expressions for poroelastic R_{PP} , R_{PS} , R_{SS} , R_{SP}

3.1 Chapter overview

In this chapter the Zoeppritz equations will be re-written using the poroelastic parameterization of Russell and Gray. The equations take the form of two sets of four equations, one for the plane-wave displacement reflection and transmission coefficients associated with an incident P-wave, and one for those associated with an incident S-wave. The elastic forms are arrived at in section 3.2, and in sections 3.3-3.4. Each element in these equations is re-expressed in poroelastic terms. This chapter will conclude with formal, exact solutions for poroelastic R_{PP} , R_{PS} , R_{SS} and R_{SP} by using Cramer's rule, in section 3.6.

3.2 A convenient formulation of the Zoeppritz equations

All 16 possible reflection and transmission wave fields are illustrated in Figure (3.1). In order to calculate the displacement amplitudes of one of the 16 wave fields, a ratio of the reflected and transmitted wave field and the incident wave field is needed. For instance, $SS_{\text{refl}}/S_{\text{inc}}$ will give the displacement amplitude ratio of a reflected S-wave and $PS_{\text{trans}}/P'_{\text{inc}}$ will give the displacement amplitude ratio of a transmitted P-wave, and so forth. All of the amplitudes displayed in Figure (3.1) can be calculated using the displacement amplitude equations by Aki and Richards (2002).

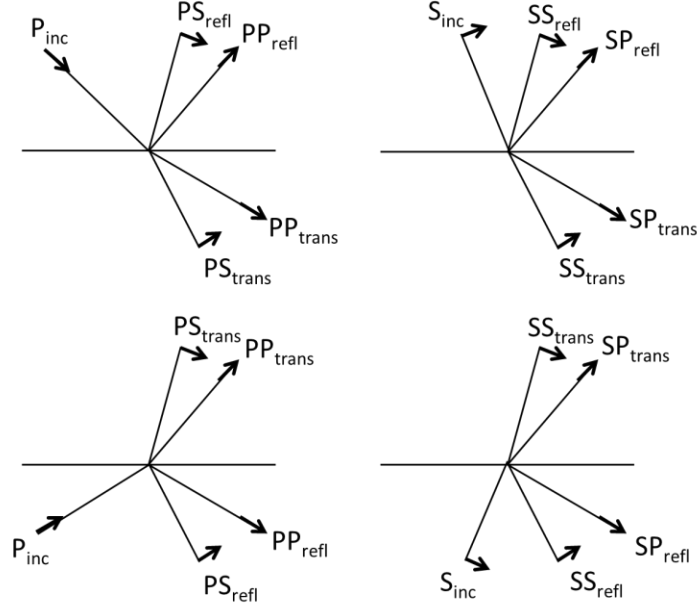


Figure 3.1: Illustration of all of the wave fields that are generated from incident plane waves. The short arrows indicate particle motion.

These 4 equations are as follows using the notation from Innanen (2011b):

$$\sin(\theta_0)(P_I + P_R) + \cos(\varphi_0)(S_I + S_R) = \sin(\theta_1)(P_T + P'_I) + \cos(\varphi_1)(S_T + S'_I), \quad (3.1)$$

and

$$\cos(\theta_0)(P_I - P_R) - \sin(\varphi_0)(S_I - S_R) = \cos(\theta_1)(P_T - P'_I) - \sin(\varphi_1)(S_T - S'_I), \quad (3.2)$$

and

$$\begin{aligned} & 2\rho_0 \frac{V_{S_0}^2}{V_{P_0}} \sin(\theta_0) \cos(\theta_0) (P_I - P_R) + \rho_0 V_{S_0} \left[1 - 2 \frac{V_{S_0}^2}{V_{P_0}^2} \sin^2(\theta_0) \right] (S_I - S_R) \\ & = 2\rho_1 \frac{V_{S_1}^2}{V_{P_0}} \sin(\theta_0) \cos(\theta_1) (P_T - P'_I) + \rho_1 V_{S_1} \left[1 - 2 \frac{V_{S_1}^2}{V_{P_0}^2} \sin^2(\theta_0) \right] (S_T - S'_I), \end{aligned} \quad (3.3)$$

and

$$\begin{aligned}
& \rho_0 V_{P_0} \left[1 - 2 \frac{V_{S_0}^2}{V_{P_0}^2} \sin^2(\theta_0) \right] (P_I + P_R) - 2 \rho_0 \frac{V_{S_0}^2}{V_{P_0}} \sin(\theta_0) \cos(\varphi_0) (S_I + S_R) \\
& = \rho_1 V_{P_1} \left[1 - 2 \frac{V_{S_1}^2}{V_{P_0}^2} \sin^2(\theta_0) \right] (P_T + P'_I) - 2 \rho_1 \frac{V_{S_1}^2}{V_{P_0}} \sin(\theta_0) \cos(\varphi_1) (S_T + S'_I).
\end{aligned} \tag{3.4}$$

The incident P- and S-wave angles that are measured with respect to the horizontal plane are θ and φ respectively; P_I, P_R, P_T are the displacement amplitudes for the incident, reflected, and transmitted P-waves respectively; S_I, S_R, S_T are the displacement amplitudes for the incident, reflected, and transmitted S-waves respectively, and P'_I and S'_I indicate displacement amplitudes for incident P- and S-waves approaching the boundary from the lower medium respectively.

3.2.1 Case 1 – incident P-wave

Reflection coefficients are produced by the ratios of the displacement amplitudes of the reflected and incident waves. Transmission coefficients are also ratios but of the displacement amplitudes of the transmitted and incident waves. For the case of an incident P-wave these ratios are

$$R_{PP} = \frac{P_R}{P_I}, \quad R_{PS} = \frac{S_R}{P_I}, \quad T_{PP} = \frac{P_T}{P_I}, \quad T_{PS} = \frac{S_T}{P_I}. \tag{3.5}$$

These ratios can be found in equations (3.1) – (3.4). By doing so, it is possible to derive the Zoeppritz equations in convenient matrix notation. As an example, equation (3.1) will be used to demonstrate how to achieve one row of the matrix-notated Zoeppritz equations as shown by Keys (1989). The displacement amplitude equation in (3.1) represents the first row of Keys (1989). To confirm this statement, two conditions must be applied to equation (3.1): the first is to apply $S'_I = P'_I = S_I = 0$ and the second is to divide the equation by P_I . Doing so results in

$$\sin(\theta_0) + \frac{P_R}{P_I} \sin(\theta_0) + \sqrt{1 - \frac{V_{S_0}^2}{V_{P_0}^2} \sin^2(\theta_0)} \frac{S_R}{P_I} = \frac{V_{P_1}}{V_{P_0}} \sin(\theta_0) \frac{P_T}{P_I} + \sqrt{1 - \frac{V_{S_1}^2}{V_{P_0}^2} \sin^2(\theta_0)} \frac{S_T}{P_I}.$$

In equation (3.1) the trigonometric identity $\cos^2 \theta + \sin^2 \theta = 1$ and Snell's law are used to write the expression in terms of θ_0 . After application of the trigonometric identity, Snell's law and substitution of equation (3.5), the equation becomes

$$-\sin(\theta_0)(R_{PP}) - \sqrt{1 - \frac{V_{S_0}^2}{V_{P_0}^2} \sin^2(\theta_0)}(R_{PS}) + \frac{V_{P_1}}{V_{P_0}} \sin(\theta_0)(T_{PP}) + \sqrt{1 - \frac{V_{S_1}^2}{V_{P_0}^2} \sin^2(\theta_0)}(T_{PS}) = \sin(\theta_0).$$

This is the first row equation found in Keys (1989). If equations (3.2) – (3.4) undergo the same process as shown for (3.1), a matrix representation of these four equations can be derived where R_{PP} , R_{PS} , T_{PP} , and T_{PS} form a column vector and the weighting factors in front of these coefficients become the elements inside a matrix \mathbf{P} . The remaining terms that are not coupled with a reflection or a transmission coefficient are then moved to the right hand side of the equal sign. In matrix notation, the result is

$$\mathbf{P} \begin{bmatrix} R_{PP} \\ R_{PS} \\ T_{PP} \\ T_{PS} \end{bmatrix} = \mathbf{m}_P, \quad (3.6)$$

where \mathbf{P} contains sixteen elements defined by the elastic parameters V_P , V_S , ρ , and θ_0 . The sixteen elements in matrix \mathbf{P} are the weighting factors that are coupled with R_{PP} , R_{PS} , T_{PP} , T_{PS} are arranged as

$$\mathbf{P} = \begin{bmatrix} A_{11} & A_{12} & A_{13} & A_{14} \\ A_{21} & A_{22} & A_{23} & A_{24} \\ A_{31} & A_{32} & A_{33} & A_{34} \\ A_{41} & A_{42} & A_{43} & A_{44} \end{bmatrix}. \quad (3.7)$$

The vector on the right hand side of equation (3.6) is a vector containing 4 elements of a 's and is written as

$$\mathbf{m}_P = \begin{bmatrix} a_1 \\ a_2 \\ a_3 \\ a_4 \end{bmatrix}. \quad (3.8)$$

All of the A_{ij} elements in the first row of \mathbf{P} are defined as

$$A_{11} = -\sin \theta_0,$$

$$A_{12} = -\left[1 - \frac{V_{S_0}^2}{V_{P_0}^2} \sin^2 \theta_0\right]^{1/2},$$

$$A_{13} = \left(\frac{V_{P_1}}{V_{P_0}}\right) \sin \theta_0,$$

$$A_{14} = -\left[1 - \left(\frac{V_{S_1}}{V_{P_0}}\right)^2 \sin^2 \theta_0\right]^{1/2},$$

the elements of the second row are

$$A_{21} = \left[1 - \sin^2 \theta_0\right]^{1/2},$$

$$A_{22} = -\left(\frac{V_{S_0}}{V_{P_0}}\right) \sin \theta_0,$$

$$A_{23} = \left[1 - \left(\frac{V_{P_1}}{V_{P_0}}\right)^2 \sin^2 \theta_0\right]^{1/2},$$

$$A_{24} = \left(\frac{V_{S_1}}{V_{P_0}}\right) \sin \theta_0,$$

the elements of the third row are

$$A_{31} = 2 \left(\frac{V_{S_0}^2}{V_{P_0}^2} \right) \sin \theta_0 \left[1 - \sin^2 \theta_0 \right]^{1/2},$$

$$A_{32} = \left(\frac{V_{S_0}}{V_{P_0}} \right) \left[1 - 2 \left(\frac{V_{S_0}^2}{V_{P_0}^2} \right) \sin^2 \theta_0 \right],$$

$$A_{33} = 2 \left(\frac{\rho_1}{\rho_0} \right) \left(\frac{V_{S_1}^2}{V_{P_0}^2} \right) \sin \theta_0 \left[1 - \left(\frac{V_{P_1}^2}{V_{P_0}^2} \right) \sin^2 \theta_0 \right]^{1/2},$$

$$A_{34} = - \left(\frac{\rho_1}{\rho_0} \right) \left(\frac{V_{S_1}}{V_{P_0}} \right) \left[1 - 2 \left(\frac{V_{S_1}^2}{V_{P_0}^2} \right) \sin^2 \theta_0 \right],$$

the elements of the fourth row are

$$A_{41} = - \left[1 - 2 \left(\frac{V_{S_0}^2}{V_{P_0}^2} \right) \sin^2 \theta_0 \right],$$

$$A_{42} = 2 \left(\frac{V_{S_0}^2}{V_{P_0}^2} \right) \sin \theta_0 \left[1 - \left(\frac{V_{S_0}^2}{V_{P_0}^2} \right) \sin^2 \theta_0 \right]^{1/2},$$

$$A_{43} = \left(\frac{\rho_1}{\rho_0} \right) \left(\frac{V_{P_1}}{V_{P_0}} \right) \left[1 - 2 \left(\frac{V_{S_1}^2}{V_{P_0}^2} \right) \sin^2 \theta_0 \right],$$

$$A_{44} = 2 \left(\frac{\rho_1}{\rho_0} \right) \left(\frac{V_{S_1}^2}{V_{P_0}^2} \right) \sin \theta_0 \left[1 - \left(\frac{V_{S_1}^2}{V_{P_0}^2} \right) \sin^2 \theta_0 \right]^{1/2},$$

and the elements representing the vector \mathbf{m}_p are

$$a_1 = \sin \theta_0,$$

$$a_2 = \left[1 - \sin^2 \theta_0 \right]^{1/2},$$

$$a_3 = 2 \left(\frac{V_{S_0}^2}{V_{P_0}^2} \right) \sin \theta_0 [1 - \sin^2 \theta_0]^{1/2},$$

$$a_4 = \left[1 - 2 \left(\frac{V_{S_0}^2}{V_{P_0}^2} \right) \sin^2 \theta_0 \right].$$

3.2.2 Case 2 – incident S-wave

The reflection and transmission coefficients for incident S-waves are produced in the same manner as shown for case 1. These coefficients are shown as displacement amplitude ratios of the reflected or transmitted wave and the incident wave. They are

$$R_{SS} = \frac{S_R}{S_I}, \quad R_{SP} = \frac{P_R}{S_I}, \quad T_{SS} = \frac{S_T}{S_I}, \quad T_{SP} = \frac{P_T}{S_I}. \quad (3.9)$$

From displacement amplitude equations (3.1) – (3.4), deriving a set of S-wave Zoeppritz equations is demonstrated by setting $P'_I = S'_I = P_I = 0$ and dividing by S_I throughout. The result is a set of modified equations that can be written in convenient matrix notation where the result is a four-by-four matrix. The matrix \mathbf{S} contains the weighting factors for R_{SS} , R_{SP} , T_{SS} , T_{SP} . Any factors that are not coupled with either a reflection coefficient or a transmission coefficient are moved to the right hand side of the equal sign. In matrix notation, the result is

$$\mathbf{S} \begin{bmatrix} R_{SS} \\ R_{SP} \\ T_{SS} \\ T_{SP} \end{bmatrix} = \mathbf{m}_S, \quad (3.10)$$

where \mathbf{S} contains 16 elements written in terms of elastic parameters V_P , V_S , ρ , and θ . This matrix is written as

$$\mathbf{S} = \begin{bmatrix} B_{11} & B_{12} & B_{13} & B_{14} \\ B_{21} & B_{22} & B_{23} & B_{24} \\ B_{31} & B_{32} & B_{33} & B_{34} \\ B_{41} & B_{42} & B_{43} & B_{44} \end{bmatrix}, \quad (3.11)$$

and the vector \mathbf{m}_s is a vector that is not coupled to a reflection or transmission coefficient and is a column vector such that

$$\mathbf{m}_s = \begin{bmatrix} b_1 \\ b_2 \\ b_3 \\ b_4 \end{bmatrix}. \quad (3.12)$$

The elements contained in the first row of equation (3.10) are

$$B_{11} = [1 - \sin^2 \varphi_0]^{1/2},$$

$$B_{12} = \left(\frac{V_{R_0}}{V_{S_0}} \right) \sin \varphi_0,$$

$$B_{13} = - \left[1 - \left(\frac{V_{S_1}^2}{V_{S_0}^2} \right) \sin^2 \varphi_0 \right]^{1/2},$$

$$B_{14} = - \left(\frac{V_{R_1}}{V_{S_0}} \right) \sin \varphi_0,$$

we find in the second row of equation (3.10)

$$B_{21} = \sin \varphi_0,$$

$$B_{22} = - \left[1 - \left(\frac{V_{R_0}^2}{V_{S_0}^2} \right) \sin^2 \varphi_0 \right]^{1/2},$$

$$B_{23} = \left(\frac{V_{S_1}}{V_{S_0}} \right) \sin \varphi_0 ,$$

$$B_{24} = - \left[1 - \left(\frac{V_{P_1}^2}{V_{S_0}^2} \right) \sin^2 \varphi_0 \right]^{1/2} ,$$

and the elements of the third row are

$$B_{31} = (1 - 2 \sin^2 \varphi_0) ,$$

$$B_{32} = 2 \left(\frac{V_{P_0}}{V_{S_0}} \right) \sin \varphi_0 \left[1 - \left(\frac{V_{P_0}^2}{V_{S_0}^2} \right) \sin^2 \varphi_0 \right]^{1/2} ,$$

$$B_{33} = \left(\frac{V_{S_1}}{V_{S_0}} \right) \left(1 - 2 \left(\frac{V_{S_1}^2}{V_{S_0}^2} \right) \sin^2 \varphi_0 \right) ,$$

$$B_{34} = 2 \left(\frac{V_{S_1}^2}{V_{S_0}^2} \right) \sin \varphi_0 \left[1 - \left(\frac{V_{P_1}^2}{V_{S_0}^2} \right) \sin^2 \varphi_0 \right]^{1/2} ,$$

the elements of the fourth row are

$$B_{41} = -2 \sin \varphi_0 \left[1 - \sin^2 \varphi_0 \right]^{1/2} ,$$

$$B_{42} = \left(\frac{V_{P_0}}{V_{S_0}} \right) (1 - 2 \sin^2 \varphi_0) ,$$

$$B_{43} = 2 \left(\frac{\rho_1}{\rho_0} \right) \left(\frac{V_{S_1}^2}{V_{S_0}^2} \right) \sin \varphi_0 \left[1 - \left(\frac{V_{S_1}^2}{V_{S_0}^2} \right) \sin^2 \varphi_0 \right]^{1/2} ,$$

$$B_{44} = - \left(\frac{\rho_1}{\rho_0} \right) \left(\frac{V_{P_1}}{V_{S_0}} \right) \left(1 - 2 \left(\frac{V_{S_1}^2}{V_{S_0}^2} \right) \sin^2 \varphi_0 \right) .$$

Finally, the elements of the vector \mathbf{m}_S are

$$b_1 = [1 - \sin^2 \varphi_0]^{1/2},$$

$$b_2 = \sin \varphi_0,$$

$$b_3 = [1 - 2 \sin^2 \varphi_0]^{1/2},$$

$$b_4 = 2 \sin \varphi_0 [1 - \sin^2 \varphi_0]^{1/2}.$$

3.3 The transformation from V_P, V_S, ρ to f, μ, ρ

The equations for the velocities V_P and V_S are written as follows

$$V_P^2 = \frac{K + \frac{4}{3}\mu}{\rho} = \frac{\lambda + 2\mu}{\rho}, \quad (3.13)$$

and

$$V_S^2 = \frac{\mu}{\rho}, \quad (3.14)$$

where K, μ, λ and ρ represent bulk modulus, shear modulus, Lamé's parameter, and density respectively. As previously mentioned in chapter 2, Russell et al. (2011) show that a fluid term can be integrated into the numerator of the P-wave velocity equation to compensate for fluid-filled media. This fluid term is written in terms of the Biot coefficient α and modulus M such that $f = \alpha^2 M$ where

$$\alpha = 1 - \frac{K_{\text{dry}}}{K_m}, \quad (3.15)$$

and

$$M = \left(\frac{\alpha - \phi}{K_m} + \frac{\phi}{K_{\text{fl}}} \right)^{-1}. \quad (3.16)$$

In these two equations, K_{dry} , K_{m} , K_{fl} are the bulk moduli for the matrix skeleton, mineral, and fluid respectively and ϕ represents the porosity. To calculate the P-wave velocity of a medium that contains fluid, the P-wave velocity equation becomes

$$\left(V_P^2\right)_{\text{sat}} = \frac{K_{\text{dry}} + \frac{4}{3}\mu_{\text{dry}} + f}{\rho_{\text{sat}}} = \frac{\lambda_{\text{dry}} + 2\mu_{\text{dry}} + f}{\rho_{\text{sat}}}, \quad (3.17)$$

where the subscripts ‘sat’ refers to media that is saturated in situ and ‘dry’ refers to a medium that is drained of fluid. The S-wave velocity equation remains unchanged as it does not include a fluid term (Russell et al., 2011). Equation (3.17) is fundamental in transitioning from parameters V_P , V_S , ρ to f , μ , ρ in the Zoeppritz equations. Since ρ does not need to be substituted in the transition and μ can be written in terms of V_S and ρ from equation (3.14), this leaves the fluid term. By using equations (3.17) and (3.14), f can be written in terms of elastic parameters such that

$$f = (\rho)_{\text{sat}} \left(V_P^2\right)_{\text{sat}} - \gamma_{\text{dry}}^2 (\mu)_{\text{sat}}, \quad (3.18)$$

where $\gamma_{\text{dry}}^2 = \left(\frac{V_P}{V_S}\right)_{\text{dry}}^2 = \frac{\lambda_{\text{dry}}}{\mu} + 2 = \frac{K_{\text{dry}}}{\mu} + \frac{4}{3}$.

3.4 The P-wave and S-wave Zoeppritz equations in poroelastic terms (f , μ , ρ)

3.4.1 Incident P-wave

There are ratios that appear in both the P- and S-wave Zoeppritz equations that appear in different combinations for velocity and density. For the P-wave Zoeppritz equations, there is a single density ratio and three V_P/V_S ratios where V_{P_0} appears in the denominator. Using Russell

et al. (2011), equation (3.19) shows that the ratios appearing in the P-wave Zoeppritz equations can be written in terms of poroelastic parameters f , μ , ρ . Those ratios are

$$\begin{aligned}
 \frac{\rho_1}{\rho_0} &= \left(\frac{\rho_1}{\rho_0} \right), \\
 \frac{V_{s_0}^2}{V_{p_0}^2} &= \left(\frac{\mu_0}{s_0 + f_0} \right), \\
 \frac{V_{p_1}^2}{V_{p_0}^2} &= \left(\frac{\rho_0}{\rho_1} \right) \left(\frac{s_1 + f_1}{s_0 + f_0} \right), \\
 \frac{V_{s_1}^2}{V_{p_0}^2} &= \left(\frac{\rho_0}{\rho_1} \right) \left(\frac{\mu_1}{s_0 + f_0} \right),
 \end{aligned} \tag{3.19}$$

where $s = \lambda + 2\mu = K + (4/3)\mu$. By substituting these ratios into the A_{ij} elements of equation (3.6), the resulting elements for the case of an incident P-wave become

$$\begin{aligned}
 A_{11} &= -\sin \theta_0, \\
 A_{12} &= -\left[1 - \left(\frac{\mu_0}{s_0 + f_0} \right) \sin^2 \theta_0 \right]^{1/2}, \\
 A_{13} &= \left[\left(\frac{\rho_0}{\rho_1} \right) \left(\frac{s_1 + f_1}{s_0 + f_0} \right) \right]^{1/2} \sin \theta_0, \\
 A_{14} &= -\left[1 - \left(\frac{\rho_0}{\rho_1} \right) \left(\frac{\mu_1}{s_0 + f_0} \right) \sin^2 \theta_0 \right]^{1/2},
 \end{aligned}$$

the elements of the second row are

$$\begin{aligned}
 A_{21} &= \left[1 - \sin^2 \theta_0 \right]^{1/2}, \\
 A_{22} &= -\left(\frac{\mu_0}{s_0 + f_0} \right)^{1/2} \sin \theta_0,
 \end{aligned}$$

$$A_{23} = \left[1 - \left(\frac{\rho_0}{\rho_1} \right) \left(\frac{s_1 + f_1}{s_0 + f_0} \right) \sin^2 \theta_0 \right]^{1/2},$$

$$A_{24} = \left[\left(\frac{\rho_0}{\rho_1} \right) \left(\frac{\mu_1}{s_0 + f_0} \right) \right]^{1/2} \sin \theta_0,$$

the elements of the third row are

$$A_{31} = 2 \left(\frac{\mu_0}{s_0 + f_0} \right) \sin \theta_0 \left[1 - \sin^2 \theta_0 \right]^{1/2},$$

$$A_{32} = \left(\frac{\mu_0}{s_0 + f_0} \right)^{1/2} \left[1 - 2 \left(\frac{\mu_0}{s_0 + f_0} \right) \sin^2 \theta_0 \right],$$

$$A_{33} = 2 \left(\frac{\mu_1}{s_0 + f_0} \right) \sin \theta_0 \left[1 - \left(\frac{\rho_0}{\rho_1} \right) \left(\frac{s_1 + f_1}{s_0 + f_0} \right) \sin^2 \theta_0 \right]^{1/2},$$

$$A_{34} = - \left(\frac{\rho_1}{\rho_0} \right) \left[\left(\frac{\rho_0}{\rho_1} \right) \left(\frac{\mu_1}{s_0 + f_0} \right) \right]^{1/2} \left[1 - 2 \left(\frac{\rho_0}{\rho_1} \right) \left(\frac{\mu_1}{s_0 + f_0} \right) \sin^2 \theta_0 \right],$$

the elements of the fourth row are

$$A_{41} = - \left[1 - 2 \left(\frac{\mu_0}{s_0 + f_0} \right) \sin^2 \theta_0 \right],$$

$$A_{42} = 2 \left(\frac{\mu_0}{s_0 + f_0} \right) \sin \theta_0 \left[1 - \left(\frac{\mu_0}{s_0 + f_0} \right) \sin^2 \theta_0 \right]^{1/2},$$

$$A_{43} = \left(\frac{\rho_1}{\rho_0} \right) \left[\left(\frac{\rho_0}{\rho_1} \right) \left(\frac{s_1 + f_1}{s_0 + f_0} \right) \right]^{1/2} \left[1 - 2 \left(\frac{\rho_0}{\rho_1} \right) \left(\frac{\mu_1}{s_0 + f_0} \right) \sin^2 \theta_0 \right],$$

$$A_{44} = 2 \left(\frac{\mu_1}{s_0 + f_0} \right) \sin \theta_0 \left[1 - \left(\frac{\rho_0}{\rho_1} \right) \left(\frac{\mu_1}{s_0 + f_0} \right) \sin^2 \theta_0 \right]^{1/2},$$

and the elements representing the vector \mathbf{m}_p are

$$\begin{aligned}
a_1 &= \sin \theta_0, \\
a_2 &= [1 - \sin^2 \theta_0]^{1/2}, \\
a_3 &= 2 \left(\frac{\mu_0}{s_0 + f_0} \right) \sin \theta_0 [1 - \sin^2 \theta_0]^{1/2}, \\
a_4 &= \left[1 - 2 \left(\frac{\mu_0}{s_0 + f_0} \right) \sin^2 \theta_0 \right].
\end{aligned}$$

3.4.2 Incident S-wave

For the S-wave Zoeppritz equations, velocity and density ratios are also found as in equation (3.19). These ratios can also be written in terms of the poroelastic parameters used by Russell et al. (2011) and are

$$\begin{aligned}
\frac{\rho_1}{\rho_0} &= \left(\frac{\rho_1}{\rho_0} \right), \\
\frac{V_{P_0}^2}{V_{S_0}^2} &= \left(\frac{s_0 + f_0}{\mu_0} \right), \\
\frac{V_{P_1}^2}{V_{S_0}^2} &= \left(\frac{\rho_0}{\rho_1} \right) \left(\frac{s_1 + f_1}{\mu_0} \right), \\
\frac{V_{S_1}^2}{V_{S_0}^2} &= \left(\frac{\mu_1}{\mu_0} \right) \left(\frac{\rho_0}{\rho_1} \right).
\end{aligned} \tag{3.20}$$

These ratios can be substituted into equation (3.10) so that the B_{ij} elements transform to the poroelastic case where the first row of \mathbf{S} becomes

$$\begin{aligned}
B_{11} &= [1 - \sin^2 \varphi_0]^{1/2}, \\
B_{12} &= - \left(\frac{s_0 + f_0}{\mu_0} \right)^{1/2} \sin \varphi_0,
\end{aligned}$$

$$B_{13} = \left[1 - \left(\frac{\mu_1}{\mu_0} \right) \left(\frac{\rho_0}{\rho_1} \right) \sin^2 \varphi_0 \right]^{1/2},$$

$$B_{14} = \left[\left(\frac{\rho_0}{\rho_1} \right) \left(\frac{s_1 + f_1}{\mu_0} \right) \right]^{1/2} \sin \varphi_0,$$

and the second row changes to

$$B_{21} = \sin \varphi_0,$$

$$B_{22} = - \left[1 - \left(\frac{s_0 + f_0}{\mu_0} \right) \sin^2 \varphi_0 \right]^{1/2},$$

$$B_{23} = \left[\left(\frac{\mu_1}{\mu_0} \right) \left(\frac{\rho_0}{\rho_1} \right) \right]^{1/2} \sin \varphi_0,$$

$$B_{24} = - \left[1 - \left(\frac{\rho_0}{\rho_1} \right) \left(\frac{s_1 + f_1}{\mu_0} \right) \sin^2 \varphi_0 \right]^{1/2},$$

the elements of the third row become

$$B_{31} = 1 - 2 \sin^2 \varphi_0,$$

$$B_{32} = 2 \sin \varphi_0 \left[1 - \left(\frac{s_0 + f_0}{\mu_0} \right) \sin^2 \varphi_0 \right]^{1/2},$$

$$B_{33} = \left(\frac{\rho_1}{\rho_0} \right) \left[\left(\frac{\mu_1}{\mu_0} \right) \left(\frac{\rho_0}{\rho_1} \right) \right]^{1/2} \left(1 - 2 \left(\frac{\mu_1}{\mu_0} \right) \left(\frac{\rho_0}{\rho_1} \right) \sin^2 \varphi_0 \right),$$

$$B_{34} = 2 \left(\frac{\mu_1}{\mu_0} \right) \sin \varphi_0 \left[1 - \left(\frac{\rho_0}{\rho_1} \right) \left(\frac{s_1 + f_1}{\mu_0} \right) \sin^2 \varphi_0 \right]^{1/2},$$

the elements of the fourth row become

$$B_{41} = -2 \sin \varphi_0 \left[1 - \sin^2 \varphi_0 \right]^{1/2},$$

$$B_{42} = \left(\frac{s_0 + f_0}{\mu_0} \right)^{1/2} (1 - 2 \sin^2 \varphi_0),$$

$$B_{43} = 2 \left(\frac{\mu_1}{\mu_0} \right) \sin \varphi_0 \left[1 - \left(\frac{\mu_1}{\mu_0} \right) \left(\frac{\rho_0}{\rho_1} \right) \sin^2 \varphi_0 \right]^{1/2},$$

$$B_{44} = - \left(\frac{\rho_1}{\rho_0} \right) \left[\left(\frac{\rho_0}{\rho_1} \right) \left(\frac{s_1 + f_1}{\mu_0} \right) \right]^{1/2} \left(1 - 2 \left(\frac{\mu_1}{\mu_0} \right) \left(\frac{\rho_0}{\rho_1} \right) \sin^2 \varphi_0 \right).$$

Finally, the elements of the vector \mathbf{m}_S change to

$$b_1 = [1 - \sin^2 \varphi_0]^{1/2},$$

$$b_2 = \sin \varphi_0,$$

$$b_3 = [1 - 2 \sin^2 \varphi_0]^{1/2},$$

$$b_4 = 2 \sin \varphi_0 [1 - \sin^2 \varphi_0]^{1/2}.$$

3.5 Solutions for R_{PP} , R_{PS} , R_{SS} , R_{SP}

The exact solutions for R_{PP} , R_{PS} , R_{SS} , and R_{SP} can be found by using a technique known as Cramer's rule where a system of linear equations contains an equal number of unknown parameters as data points. Each solution is found by taking the determinant of an augmented matrix and dividing by the determinant of the un-augmented matrix where

$$R_{PP} = \frac{\det \mathbf{P}_P}{\det \mathbf{P}}, \quad R_{PS} = \frac{\det \mathbf{P}_S}{\det \mathbf{P}}, \quad R_{SS} = \frac{\det \mathbf{S}_S}{\det \mathbf{S}}, \quad R_{SP} = \frac{\det \mathbf{S}_P}{\det \mathbf{S}}. \quad (3.21)$$

The augmented matrices \mathbf{P}_P and \mathbf{P}_S are written such that a column is replaced by the vector \mathbf{m}_P and likewise \mathbf{S}_S and \mathbf{S}_P are written such that a column is replaced by the vector \mathbf{m}_S . These matrices are shown as

$$\begin{aligned}
\mathbf{P}_P &= \begin{bmatrix} a_1 & A_{12} & A_{13} & A_{14} \\ a_2 & A_{22} & A_{23} & A_{24} \\ a_3 & A_{32} & A_{33} & A_{34} \\ a_4 & A_{42} & A_{43} & A_{44} \end{bmatrix}, & \mathbf{P}_S &= \begin{bmatrix} A_{11} & a_1 & A_{13} & A_{14} \\ A_{21} & a_2 & A_{23} & A_{24} \\ A_{31} & a_3 & A_{33} & A_{34} \\ A_{41} & a_4 & A_{43} & A_{44} \end{bmatrix}, \\
\mathbf{S}_S &= \begin{bmatrix} b_1 & B_{12} & B_{13} & B_{14} \\ b_2 & B_{22} & B_{23} & B_{24} \\ b_3 & B_{32} & B_{33} & B_{34} \\ b_4 & B_{42} & B_{43} & B_{44} \end{bmatrix}, & \mathbf{S}_P &= \begin{bmatrix} B_{11} & b_1 & B_{13} & B_{14} \\ B_{21} & b_2 & B_{23} & B_{24} \\ B_{31} & b_3 & B_{33} & B_{34} \\ B_{41} & b_4 & B_{43} & B_{44} \end{bmatrix}.
\end{aligned} \tag{3.22}$$

3.6 Chapter summary

Equations (3.21) are exact, though formal, solutions for displacement reflection coefficients in terms of poroelastic parameters as used by Russell et al. (2011) in their linearized expression.

In the following chapters we will investigate series expansions of R_{PP} , paying particular attention to (1) their consistency with the Russell and Gray $f - m - r$ equation, and (2) the importance of their higher order (nonlinear) terms.

Chapter Four: Series solutions for poroelastic R_{PP}

4.1 Chapter overview

Leading from the end of chapter 3 which showed the formalism of deriving exact poroelastic solutions of R_{PP} , R_{PS} , R_{SS} and R_{SP} , chapter 4 will show how to achieve a series solution for poroelastic R_{PP} . This chapter begins by defining a set of perturbations in f , μ , ρ in section 4.2 that will re-parameterize the P-wave Zoeppritz equations. Section 4.3 will demonstrate the application of a Taylor series expansion of each element of the Zoeppritz equations; this will be followed by the product of calculating the determinant ratio of the augmented and un-augmented \mathbf{P} matrix. Section 4.4 will show how to write perturbations in terms of reflectivity and finally section 4.5 will discuss the $(\gamma_1)_{\text{dry}}^2$ parameter how this parameter affects the series solution for poroelastic R_{PP} .

4.2 The poroelastic P-wave Zoeppritz equations in perturbative form

From chapter 3, the poroelastic P-wave Zoeppritz equations are in terms of f , μ , ρ . To re-parameterize the poroelastic P-wave Zoeppritz equations, we will first define a set of perturbations for poroelastic media such that

$$a_f = 1 - \frac{f_0}{f_1}, \quad a_\mu = 1 - \frac{\mu_0}{\mu_1}, \quad a_\rho = 1 - \frac{\rho_0}{\rho_1}. \quad (4.1)$$

The ratios found in chapter 3 in equation (3.19) can be written in terms of perturbations.

Substituting equation (4.1) into (3.19) yields

$$\begin{aligned}
\left(\frac{\rho_1}{\rho_0}\right) &= (1-a_\rho)^{-1}, \\
\left(\frac{\mu_0}{s_0+f_0}\right) &= (\gamma_0)_{\text{sat}}^{-2}, \\
\left(\frac{\rho_0}{\rho_1}\right)\left(\frac{s_1+f_1}{s_0+f_0}\right) &= (1-a_\rho)\left[\left(\frac{(\gamma_0)_{\text{dry}}^2}{(\gamma_0)_{\text{sat}}^2}\right)(1-a_\mu)^{-1} + \left(1-\frac{(\gamma_0)_{\text{dry}}^2}{(\gamma_0)_{\text{sat}}^2}\right)(1-a_f)^{-1}\right], \\
\left(\frac{\rho_0}{\rho_1}\right)\left(\frac{\mu_1}{s_0+f_0}\right) &= \frac{(1-a_\mu)^{-1}(1-a_\rho)}{(\gamma_0)_{\text{sat}}^2}.
\end{aligned} \tag{4.2}$$

Of these four ratios, the first ratio is the simplest to write in terms of perturbation. The second ratio is the inverse of $V_{P_0}^2/V_{S_0}^2$ and is written using $(\gamma)_{\text{sat}}^{-2}$ to maintain consistent notation with Russell et al. (2011). The fourth ratio can be shown to be true by

$$\left(\frac{\rho_0}{\rho_1}\right)\left(\frac{\mu_1}{s_0+f_0}\right) = \left(\frac{\mu_1}{\mu_0}\right)\frac{(1-a_\rho)}{s_0+f_0}\mu_0 = \frac{(1-a_\mu)^{-1}(1-a_\rho)}{(\gamma_0)_{\text{sat}}^2},$$

and the third ratio is the most complex where the ratio can be shown by

$$\begin{aligned}
\left(\frac{V_{P_1}^2}{V_{P_0}^2}\right) &= \left(\frac{\rho_0}{\rho_1}\right)\left(\frac{s_1+f_1}{s_0+f_0}\right) = \frac{s_1+f_1}{\rho_1} \times \frac{\rho_0}{s_0+f_0}, \\
&= (1-a_\rho)\left[\frac{s_1}{s_0+f_0} + \frac{f_1}{s_0+f_0}\right], \\
&= (1-a_\rho)\left[\frac{(\gamma_0)_{\text{dry}}^2 \mu_1}{\rho_0 V_{P_0}^2} + \frac{f_0(1-a_f)^{-1}}{\rho_0 V_{P_0}^2}\right], \\
&= (1-a_\rho)\left[\frac{(\gamma_0)_{\text{dry}}^2 \mu_0(1-a_\mu)^{-1}}{\rho_0 V_{P_0}^2} + \frac{(\rho_0 V_{P_0}^2 - (\gamma_0)_{\text{dry}}^2 \mu_0)(1-a_f)^{-1}}{\rho_0 V_{P_0}^2}\right], \\
&= (1-a_\rho)\left[\left(\frac{(\gamma_0)_{\text{dry}}^2}{(\gamma_0)_{\text{sat}}^2}\right)(1-a_\mu)^{-1} + \left(1-\frac{(\gamma_0)_{\text{dry}}^2}{(\gamma_0)_{\text{sat}}^2}\right)(1-a_f)^{-1}\right].
\end{aligned}$$

Note that this derivation of $V_{P_1}^2/V_{P_0}^2$ uses $(\gamma_0)_{\text{dry}}^2$ in place of $(\gamma_1)_{\text{dry}}^2$ in the third line of this equation. The parameter that reflects the skeleton framework of the lower medium s_1 should contain $(\gamma_1)_{\text{dry}}^2$ as $s_1 = (\gamma_1)_{\text{dry}}^2 \mu_1$. The justification to not use $(\gamma_1)_{\text{dry}}^2$ is the result of the number of weighting factors that are found when deriving the linear solution for poroelastic R_{pp} . There are 28 weighting factors coupled with the a_f term, 28 weighting factors coupled with a_μ , 31 weighting factors coupled with the a_ρ term and an additional 32 weighting factors that are not coupled with a perturbation. This will be discussed further in section 4.5. Nevertheless, these ratios may be substituted into the poroelastic P-wave Zoeppritz equations.

By substituting the perturbations of equation (4.1) into the poroelastic P-wave Zoeppritz equations, the elements in \mathbf{P} will change such that the first row becomes

$$A_{11} = -\sin \theta_0,$$

$$A_{12} = -\left[1 - (\gamma_0)_{\text{sat}}^2 \sin^2 \theta_0\right]^{1/2},$$

$$A_{13} = \left(\frac{(\gamma_0)_{\text{dry}}^2 (1 - a_\rho)}{(\gamma_0)_{\text{sat}}^2 (1 - a_\mu)} + \left(1 - \frac{(\gamma_0)_{\text{dry}}^2}{(\gamma_0)_{\text{sat}}^2}\right) \frac{(1 - a_\rho)}{(1 - a_f)}\right)^{1/2} \sin \theta_0,$$

$$A_{14} = -\left[1 - \frac{(1 - a_\mu)^{-1} (1 - a_\rho)}{(\gamma_0)_{\text{sat}}^2} \sin^2 \theta_0\right]^{1/2},$$

the elements of the second row become

$$A_{21} = \left[1 - \sin^2 \theta_0\right]^{1/2},$$

$$A_{22} = -(\gamma_0)_{\text{sat}} \sin \theta_0,$$

$$A_{23} = \left[1 - \left\{ (1 - a_\rho) \left[\left(\frac{(\gamma_0)_{\text{dry}}^2}{(\gamma_0)_{\text{sat}}^2} \right) (1 - a_\mu)^{-1} + \left(1 - \frac{(\gamma_0)_{\text{dry}}^2}{(\gamma_0)_{\text{sat}}^2} \right) (1 - a_f)^{-1} \right] \right\} \sin^2 \theta_0 \right]^{1/2},$$

$$A_{24} = \frac{\left((1 - a_\mu)^{-1} (1 - a_\rho) \right)^{1/2}}{(\gamma_0)_{\text{sat}}} \sin \theta_0,$$

the elements of the third row become

$$A_{31} = 2(\gamma_0)_{\text{sat}}^2 \sin \theta_0 [1 - \sin^2 \theta_0]^{1/2},$$

$$A_{32} = (\gamma_0)_{\text{sat}} [1 - 2(\gamma_0)_{\text{sat}}^2 \sin^2 \theta_0],$$

$$A_{33} = 2(1 - a_\rho)^{-1} \left(\frac{(1 - a_\mu)^{-1} (1 - a_\rho)}{(\gamma_0)_{\text{sat}}^2} \right) \sin \theta_0$$

$$\times \left[1 - \left\{ (1 - a_\rho) \left[\left(\frac{(\gamma_0)_{\text{dry}}^2}{(\gamma_0)_{\text{sat}}^2} \right) (1 - a_\mu)^{-1} + \left(1 - \frac{(\gamma_0)_{\text{dry}}^2}{(\gamma_0)_{\text{sat}}^2} \right) (1 - a_f)^{-1} \right] \right\} \sin^2 \theta_0 \right]^{1/2},$$

$$A_{34} = -(1 - a_\rho)^{-1} \left(\frac{(1 - a_\mu)^{-1} (1 - a_\rho)}{(\gamma_0)_{\text{sat}}^2} \right)^{1/2} \left[1 - 2 \left(\frac{(1 - a_\mu)^{-1} (1 - a_\rho)}{(\gamma_0)_{\text{sat}}^2} \right) \sin^2 \theta_0 \right],$$

the elements of the fourth row become

$$A_{41} = -[1 - 2(\gamma_0)_{\text{sat}}^2 \sin^2 \theta_0],$$

$$A_{42} = 2(\gamma_0)_{\text{sat}}^2 \sin \theta_0 \left[1 - (\gamma_0)_{\text{sat}}^2 \sin^2 \theta_0 \right]^{1/2},$$

$$A_{43} = (1 - a_\rho)^{-1} \left\{ (1 - a_\rho) \left[\left(\frac{(\gamma_0)_{\text{dry}}^2}{(\gamma_0)_{\text{sat}}^2} \right) (1 - a_\mu)^{-1} + \left(1 - \frac{(\gamma_0)_{\text{dry}}^2}{(\gamma_0)_{\text{sat}}^2} \right) (1 - a_f)^{-1} \right] \right\}^{1/2} \\ \times \left[1 - 2 \left(\frac{(1 - a_\mu)^{-1} (1 - a_\rho)}{(\gamma_0)_{\text{sat}}^2} \right) \sin^2 \theta_0 \right],$$

$$A_{44} = 2(1 - a_\rho)^{-1} \left(\frac{(1 - a_\mu)^{-1} (1 - a_\rho)}{(\gamma_0)_{\text{sat}}^2} \right) \sin \theta_0 \left[1 - \left(\frac{(1 - a_\mu)^{-1} (1 - a_\rho)}{(\gamma_0)_{\text{sat}}^2} \right) \sin^2 \theta_0 \right]^{1/2},$$

and the elements of the vector \mathbf{m}_p become

$$a_1 = \sin \theta_0,$$

$$a_2 = \left[1 - \sin^2 \theta_0 \right]^{1/2},$$

$$a_3 = 2(\gamma_0)_{\text{sat}}^2 \sin \theta_0 \left[1 - \sin^2 \theta_0 \right]^{1/2},$$

$$a_4 = \left[1 - 2(\gamma_0)_{\text{sat}}^2 \sin^2 \theta_0 \right].$$

4.3 Series expansion of the solution for R_{pp}

4.3.1 Expansion of each element of the Zoeppritz matrix

After having written the A_{ij} elements in matrix \mathbf{P} and a_i elements in vector \mathbf{m}_p in terms of perturbation, the next step involves using Taylor series expansion. The Taylor series expansion will be applied to each element in orders of $\sin^2 \theta_0$, a_f , a_μ , and a_ρ .

This will result in changes of the first row of \mathbf{P} to become

$$A_{11} = -\sin \theta_0,$$

$$A_{12} = -1 + \frac{1}{2}(\gamma_0)_{\text{sat}}^2 \sin^2 \theta_0,$$

$$A_{13} = \sin \theta_0 + \left[\left(\frac{1}{2} - \frac{(\gamma_0)_{\text{dry}}^2}{2(\gamma_0)_{\text{sat}}^2} \right) \sin \theta_0 \right] a_f + \left(\frac{(\gamma_0)_{\text{dry}}^2}{2(\gamma_0)_{\text{sat}}^2} \sin \theta_0 \right) a_\mu - \left(\frac{1}{2} \sin \theta_0 \right) a_\rho + \dots,$$

$$A_{14} = -1 + \frac{1}{(\gamma_0)_{\text{sat}}^2} \sin^2 \theta_0 + \left(\frac{1}{2(\gamma_0)_{\text{sat}}^2} \sin^2 \theta_0 \right) a_\mu - \left(\frac{1}{2(\gamma_0)_{\text{sat}}^2} \sin^2 \theta_0 \right) a_\rho + \dots,$$

changes in the second row of \mathbf{P} to become

$$A_{21} = 1 - \frac{1}{2} \sin^2 \theta_0,$$

$$A_{22} = -(\gamma_0)_{\text{sat}} \sin \theta_0,$$

$$A_{23} = 1 - \frac{1}{2} \sin^2 \theta_0 - \left[\frac{1}{2} \left(1 - \frac{(\gamma_0)_{\text{dry}}^2}{(\gamma_0)_{\text{sat}}^2} \right) \sin^2 \theta_0 \right] a_f - \left(\frac{(\gamma_0)_{\text{dry}}^2}{2(\gamma_0)_{\text{sat}}^2} \sin^2 \theta_0 \right) a_\mu + \left(\frac{1}{2} \sin^2 \theta_0 \right) a_\rho + \dots,$$

$$A_{24} = \frac{1}{(\gamma_0)_{\text{sat}}} \sin \theta_0 + \left(\frac{1}{2(\gamma_0)_{\text{sat}}} \right) a_\mu - \left(\frac{1}{2(\gamma_0)_{\text{sat}}} \sin \theta \right) a_\rho + \dots,$$

changes in the third row of \mathbf{P} to become

$$A_{31} = 2(\gamma_0)_{\text{sat}}^2 \sin \theta_0,$$

$$A_{32} = (\gamma_0)_{\text{sat}} \left[1 - 2(\gamma_0)_{\text{sat}}^2 \sin^2 \theta_0 \right],$$

$$A_{33} = \frac{2}{(\gamma_0)_{\text{sat}}^2} \sin \theta_0 + \left(\frac{2}{(\gamma_0)_{\text{sat}}^2} \sin \theta_0 \right) a_\mu + \dots,$$

$$\begin{aligned}
A_{34} = & -\left(\frac{1}{(\gamma_0)_{\text{sat}}}\right)\left(1 - \frac{2}{(\gamma_0)_{\text{sat}}^2} \sin^2 \theta_0\right) + \left(\frac{2}{(\gamma_0)_{\text{sat}}^3} \sin^2 \theta_0 - \frac{1}{2(\gamma_0)_{\text{sat}}}\left(1 - \frac{2}{(\gamma_0)_{\text{sat}}^2} \sin^2 \theta_0\right)\right) a_{\mu} \\
& + \left(-\frac{2}{(\gamma_0)_{\text{sat}}^3} \sin^2 \theta_0 - \frac{1}{2(\gamma_0)_{\text{sat}}}\left(1 - \frac{2}{(\gamma_0)_{\text{sat}}^2} \sin^2 \theta_0\right)\right) a_{\rho} + \dots,
\end{aligned}$$

changes in the fourth row \mathbf{P} to become

$$A_{41} = 2(\gamma_0)_{\text{sat}}^2 \sin^2 \theta_0 - 1,$$

$$A_{42} = 2(\gamma_0)_{\text{sat}}^2 \sin \theta_0,$$

$$\begin{aligned}
A_{43} = & 1 - \frac{2}{(\gamma_0)_{\text{sat}}^2} \sin^2 \theta_0 + \left(\frac{1}{2} - \frac{(\gamma_0)_{\text{dry}}^2}{2(\gamma_0)_{\text{sat}}^2}\right)\left(1 - \frac{2}{(\gamma_0)_{\text{sat}}^2} \sin^2 \theta_0\right) a_f \\
& + \left[\left(\frac{(\gamma_0)_{\text{dry}}^2}{2(\gamma_0)_{\text{sat}}^2}\right)\left(1 - \frac{2}{(\gamma_0)_{\text{sat}}^2} \sin^2 \theta_0\right) - \frac{2}{(\gamma_0)_{\text{sat}}^2} \sin^2 \theta_0\right] a_{\mu} + \left(\frac{1}{2} + \frac{1}{(\gamma_0)_{\text{sat}}^2} \sin^2 \theta_0\right) a_{\rho} + \dots,
\end{aligned}$$

$$A_{44} = \frac{2}{(\gamma_0)_{\text{sat}}^2} \sin \theta_0 + \left(\frac{2}{(\gamma_0)_{\text{sat}}^2} \sin \theta_0\right) a_{\mu} + \dots$$

Finally, changes in the elements of \mathbf{m}_P to become

$$a_1 = \sin \theta_0,$$

$$a_2 = 1 - \frac{1}{2} \sin^2 \theta_0,$$

$$a_3 = 2(\gamma_0)_{\text{sat}}^2 \sin \theta_0,$$

$$a_4 = 1 - 2(\gamma_0)_{\text{sat}}^2 \sin^2 \theta_0.$$

4.3.2 Expansion of the determinant ratios

Expanding the ratio of determinants of the four-by-four matrix \mathbf{P} required the use of mathematical processing software Maple to calculate R_{PP} . Using compact notation, the solution of R_{PP} is

$$R_{\text{PP}} = R_{\text{PP}}^{(1)} + R_{\text{PP}}^{(2)} + R_{\text{PP}}^{(3)} + \dots, \quad (4.3)$$

where the first, second, and third order terms are contained within $R_{\text{PP}}^{(1)}$, $R_{\text{PP}}^{(2)}$ and $R_{\text{PP}}^{(3)}$ respectively. Equation (4.3) is the symbolic representation of the exact series solution of R_{PP} .

For a first order poroelastic AVO approximation, $R_{\text{PP}}^{(2)}$, $R_{\text{PP}}^{(3)}$ and etc are neglected. This is an approximation of the exact solutions and is written as

$$R_{\text{PP}} \approx R_{\text{PP}}^{(1)}, \quad (4.4)$$

the second order approximation includes both first and second order terms which means

$$R_{\text{PP}} \approx R_{\text{PP}}^{(1)} + R_{\text{PP}}^{(2)}, \quad (4.5)$$

and the third order approximation includes the first, second, and third order terms such that

$$R_{\text{PP}} \approx R_{\text{PP}}^{(1)} + R_{\text{PP}}^{(2)} + R_{\text{PP}}^{(3)}, \quad (4.6)$$

and etc. There are three weighting terms found in $R_{\text{PP}}^{(1)}$, six in $R_{\text{PP}}^{(2)}$, and ten in $R_{\text{PP}}^{(3)}$. Explicitly,

$R_{\text{PP}}^{(1)}$ appears as

$$R_{\text{PP}}^{(1)}(\theta_0) = \left[\left(1 - \frac{(\gamma_0)_{\text{dry}}^2}{(\gamma_0)_{\text{sat}}^2} \right) \frac{(1 + \sin^2 \theta_0)}{4} \right] a_f + \left[\frac{(\gamma_0)_{\text{dry}}^2}{4(\gamma_0)_{\text{sat}}^2} (1 + \sin^2 \theta_0) - \frac{2}{(\gamma_0)_{\text{sat}}^2} \sin^2 \theta_0 \right] a_\mu + \left[\frac{1}{4} - \frac{\sin^2 \theta_0}{4} \right] a_\rho, \quad (4.7)$$

which has the same number of weighting terms as Russell et al. (2011). Due to equation length, the second and third order poroelastic R_{PP} terms are found in appendix A.

4.4 Transformation from perturbative form to reflectivity form

Aki and Richards (2002), Shuey (1985), Russell et al. (2011) and others use model parameters known as reflectivities to parameterize AVO approximations. Russell et al. (2011) use poroelastic model parameters f , μ and ρ to characterize gas-saturated sands. The reflectivity terms are

$$\frac{\Delta f}{f} = \frac{2(f_1 - f_0)}{f_1 + f_0}, \quad \frac{\Delta \mu}{\mu} = \frac{2(\mu_1 - \mu_0)}{\mu_1 + \mu_0}, \quad \frac{\Delta \rho}{\rho} = \frac{2(\rho_1 - \rho_0)}{\rho_1 + \rho_0}. \quad (4.8)$$

Using the definitions for perturbations in equation (4.1) and the reflectivity definitions in (4.8), reflectivity can be written as a series of perturbations. It can also be shown that for small property contrasts, when reflectivity is small in value, reflectivity is approximately equal to perturbation such that

$$\begin{aligned} \frac{\Delta f}{f} &= \frac{2(f_1 - f_0)}{f_1 + f_0} = 2 \frac{1 - f_0/f_1}{1 + f_0/f_1} = 2 \frac{a_f}{1 + (1 - a_f)} = \frac{a_f}{1 - (1/2)a_f} \\ &= a_f \left[1 + \left(\frac{1}{2}a_f\right) + \left(\frac{1}{2}a_f\right)^2 + \dots \right] \approx a_f. \end{aligned} \quad (4.9)$$

This shows fluid reflectivity as a fluid perturbation series. By inspection of equation (4.8) and (4.9), reflectivities $\Delta\mu/\mu$ and $\Delta\rho/\rho$ will yield the same symbolic result as (4.9). Using equation (4.9), fluid perturbation a_f may be written in terms of fluid reflectivity $\Delta f/f$ using series reversion. This is accomplished by defining an inverse series for a_f where

$$a_f = a_{f_1} + a_{f_2} + \dots \quad (4.10)$$

By substituting equation (4.10) into (4.9), equating like orders will then produce an expression for a_f such that

$$a_f = \frac{\Delta f}{f} - \frac{1}{2} \left(\frac{\Delta f}{f} \right)^2 + \dots \quad (4.11)$$

The symbolic forms for the shear modulus and density perturbations and reflectivities are identical therefore the shear modulus and density perturbation inverse series are

$$a_\mu = \frac{\Delta \mu}{\mu} - \frac{1}{2} \left(\frac{\Delta \mu}{\mu} \right)^2 + \dots, \quad (4.12)$$

and

$$a_\rho = \frac{\Delta \rho}{\rho} - \frac{1}{2} \left(\frac{\Delta \rho}{\rho} \right)^2 + \dots \quad (4.13)$$

Using the fluid, shear modulus and density inverse series' in (4.11) – (4.13), substitutions of those into (4.1) will create a set of poroelastic P-wave Zoeppritz solutions that measure relative changes in reflectivity terms rather than perturbation. The steps that are applied in order to derive an exact series solution for poroelastic R_{PP} using perturbation contrasts are the same for reflectivity. Due to length, the second and third order poroelastic R_{PP} approximations are left in appendix A; however, the first order approximation is

$$R_{PP}(\theta_0) \approx \left[\left(1 - \frac{(\gamma_0)_{\text{dry}}^2}{(\gamma_0)_{\text{sat}}^2} \right) \frac{(1 + \sin^2 \theta_0)}{4} \right] \frac{\Delta f}{f} + \left[\frac{(\gamma_0)_{\text{dry}}^2}{4(\gamma_0)_{\text{sat}}^2} (1 + \sin^2 \theta_0) - \frac{2}{(\gamma_0)_{\text{sat}}^2} \sin^2 \theta_0 \right] \frac{\Delta \mu}{\mu} \quad (4.14)$$

$$+ \left[\frac{1}{4} - \frac{\sin^2 \theta_0}{4} \right] \frac{\Delta \rho}{\rho},$$

where this solution contains the same weighting coefficients as the approximation in equation (4.7).

4.5 The $(\gamma_1)_{\text{dry}}^2$ parameter

As mentioned in section 4.2, use of the $(\gamma_1)_{\text{dry}}^2$ parameter instead of the $(\gamma_0)_{\text{dry}}^2$ parameter in the $V_{P_1}^2/V_{P_0}^2$ ratio produces different analytical series solutions in R_{PP} . For convenience, the series solution containing the $(\gamma_1)_{\text{dry}}^2$ parameter will be the $(\gamma_1)_{\text{dry}}^2$ series solution and the series solution containing $(\gamma_0)_{\text{dry}}^2$ will be the $(\gamma_0)_{\text{dry}}^2$ series solution. Numerically, these two series solutions are compared with the exact solutions. The result of this comparison shows that for small perturbations, the two series solutions are approximately equal as shown in Figure (4.1a). As the perturbations increase however, the $(\gamma_1)_{\text{dry}}^2$ series solution begins to diverge more quickly from the exact solution than $(\gamma_0)_{\text{dry}}^2$ series solution. In Figure 4.1 the blue curve represents the exact solutions, the red curve represents the $(\gamma_1)_{\text{dry}}^2$ solution and the blue curve represents the $(\gamma_0)_{\text{dry}}^2$ solution.

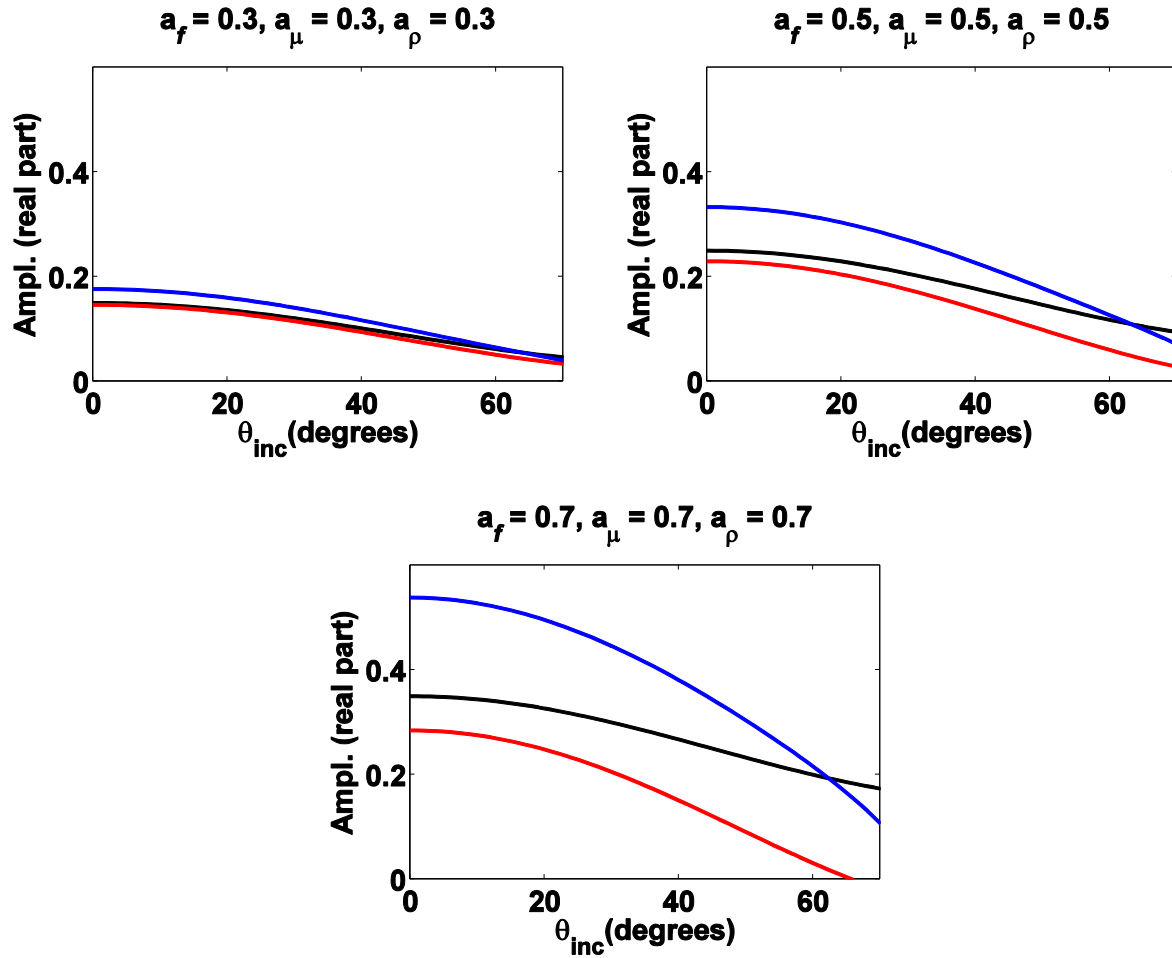


Figure 4.1: These plots compare the exact series solutions (blue) with the linear R_{PP} solution that uses $(\gamma_1)_{dry}^2$ (red) and the linear R_{PP} solution that uses $(\gamma_0)_{dry}^2$ (black).

4.6 Chapter summary

The approximation shown in equations (4.7) and (4.14) is the result of deriving a series solution for R_{PP} in terms of poroelastic property contrasts. These two equations are different by how each equation measures poroelasticity, equation (4.7) is in terms of perturbation and (4.14) is in terms of reflectivity. The weighting factors however, are identical and equation (4.14) will be compared with the Russell and Gray approximation in the next chapter. Numerical modeling will also be explored in the next chapter.

Chapter Five: Exact, linear, and nonlinear poroelastic AVO modeling: validation and analysis

5.1 Chapter overview

The forms for the first, second and third order poroelastic AVO approximations are shown in section 5.2. The linear derivation of R_{PP} will be compared with the Russell and Gray approximation for the purpose of showing that they agree with each other in section 5.3.

Following is a numerical study of the exact, linear and nonlinear approximations in both perturbation and reflectivity domains to illustrate the benefit of including low-order nonlinear terms.

5.2 Forms for first, second and third order series approximations

Using the methods shown in chapter 4 illustrate how to apply Cramer's rule to produce series solutions, the exact expression for PP reflection coefficients involves all corrective terms

$R_{PP}^{(1)} + R_{PP}^{(2)} + R_{PP}^{(3)} + \dots$. The linear approximation involves only the first order corrective term

$R_{PP}^{(1)}$ and the second and third order approximations include corrective terms $R_{PP}^{(1)} + R_{PP}^{(2)}$ and

$R_{PP}^{(1)} + R_{PP}^{(2)} + R_{PP}^{(3)}$, respectively. These approximations in the perturbation and reflectivity

domains create two sets of approximations that bring the total number of approximations to six.

In the set of approximations that involve perturbations, the first order approximation is

$$R_{PP} \approx W_{a_1} a_f + W_{a_2} a_\mu + W_{a_3} a_\rho, \quad (5.1)$$

the second order approximation is

$$\begin{aligned} R_{PP} \approx & W_{a_1} a_f + W_{a_2} a_\mu + W_{a_3} a_\rho + W_{a_4} a_f^2 + W_{a_5} a_\mu^2 + W_{a_6} a_\rho^2 \\ & + W_{a_7} a_f a_\mu + W_{a_8} a_f a_\rho + W_{a_9} a_\mu a_\rho, \end{aligned} \quad (5.2)$$

and the third order approximation is

$$\begin{aligned}
R_{\text{PP}} \approx & W_{a_1} a_f + W_{a_2} a_\mu + W_{a_3} a_\rho + W_{a_4} a_f^2 + W_{a_5} a_\mu^2 + W_{a_6} a_\rho^2 \\
& + W_{a_7} a_f a_\mu + W_{a_8} a_f a_\rho + W_{a_9} a_\mu a_\rho + W_{a_{10}} a_f^3 + W_{a_{11}} a_\mu^3 + W_{a_{12}} a_\rho^3 \\
& + W_{a_{13}} a_f^2 a_\mu + W_{a_{14}} a_f^2 a_\rho + W_{a_{15}} a_\mu^2 a_f + W_{a_{16}} a_\mu^2 a_\rho + W_{a_{17}} a_\rho^2 a_f \\
& + W_{a_{18}} a_\rho^2 a_\mu + W_{a_{19}} a_f a_\mu a_\rho,
\end{aligned} \tag{5.3}$$

where the weighting factors are represented by W_a . There are three weighting factors in the first order approximation, nine in the second order approximation and nineteen in the third order approximation. In the second set of approximations that use reflectivity, the first order approximation is

$$R_{\text{PP}} \approx W_{\Delta_1} \frac{\Delta f}{f} + W_{\Delta_2} \frac{\Delta \mu}{\mu} + W_{\Delta_3} \frac{\Delta \rho}{\rho}, \tag{5.4}$$

the second order approximation is

$$\begin{aligned}
R_{\text{PP}} \approx & W_{\Delta_1} \frac{\Delta f}{f} + W_{\Delta_2} \frac{\Delta \mu}{\mu} + W_{\Delta_3} \frac{\Delta \rho}{\rho} + W_{\Delta_4} \left(\frac{\Delta f}{f} \right)^2 + W_{\Delta_5} \left(\frac{\Delta \mu}{\mu} \right)^2 \\
& + W_{\Delta_6} \left(\frac{\Delta \rho}{\rho} \right)^2 + W_{\Delta_7} \frac{\Delta f}{f} \frac{\Delta \mu}{\mu} + W_{\Delta_8} \frac{\Delta f}{f} \frac{\Delta \rho}{\rho} + W_{\Delta_9} \frac{\Delta \mu}{\mu} \frac{\Delta \rho}{\rho},
\end{aligned} \tag{5.5}$$

and the third order approximation is

$$\begin{aligned}
R_{\text{PP}} \approx & W_{\Delta_1} \frac{\Delta f}{f} + W_{\Delta_2} \frac{\Delta \mu}{\mu} + W_{\Delta_3} \frac{\Delta \rho}{\rho} + W_{\Delta_4} \left(\frac{\Delta f}{f} \right)^2 + W_{\Delta_5} \left(\frac{\Delta \mu}{\mu} \right)^2 \\
& + W_{\Delta_6} \left(\frac{\Delta \rho}{\rho} \right)^2 + W_{\Delta_7} \frac{\Delta f}{f} \frac{\Delta \mu}{\mu} + W_{\Delta_8} \frac{\Delta f}{f} \frac{\Delta \rho}{\rho} + W_{\Delta_9} \frac{\Delta \mu}{\mu} \frac{\Delta \rho}{\rho} \\
& + W_{\Delta_{10}} \left(\frac{\Delta f}{f} \right)^3 + W_{\Delta_{11}} \left(\frac{\Delta \mu}{\mu} \right)^3 + W_{\Delta_{12}} a_\rho^3 \left(\frac{\Delta \rho}{\rho} \right)^3 + W_{\Delta_{13}} \left(\frac{\Delta f}{f} \right)^2 \frac{\Delta \mu}{\mu} \\
& + W_{\Delta_{14}} \left(\frac{\Delta f}{f} \right)^2 \frac{\Delta \rho}{\rho} + W_{\Delta_{15}} \left(\frac{\Delta \mu}{\mu} \right)^2 \frac{\Delta f}{f} + W_{\Delta_{16}} \left(\frac{\Delta \mu}{\mu} \right)^2 \frac{\Delta \rho}{\rho} \\
& + W_{\Delta_{17}} \left(\frac{\Delta \rho}{\rho} \right)^2 \frac{\Delta f}{f} + W_{\Delta_{18}} \left(\frac{\Delta \rho}{\rho} \right)^2 \frac{\Delta \mu}{\mu} + W_{\Delta_{19}} \frac{\Delta f}{f} \frac{\Delta \mu}{\mu} \frac{\Delta \rho}{\rho}.
\end{aligned} \tag{5.6}$$

This set of approximations shows the same number of weighting factors as the perturbation-based approximations.

5.3 Agreement of first order R_{PP} with expression of Russell and Gray

Russell et al. (2011) have presented a linearized poroelastic approximation for PP reflection coefficients that resembles forms shown by Aki and Richards (2002), Shuey (1985), Wiggins et al. (1983), and Smith and Gidlow (1987). This formulation is able to invert seismic amplitude data to predict a fluid parameter. To reiterate from chapter 2, the equation by Russell et al. (2011) is

$$R_{PP}^{(RG)}(\theta) \approx \left[\left(1 - \frac{\gamma_{dry}^2}{\gamma_{sat}^2} \right) \frac{\sec^2 \theta}{4} \right] \frac{\Delta f}{f} + \left[\frac{\gamma_{dry}^2}{4\gamma_{sat}^2} \sec^2 \theta - \frac{2}{\gamma_{sat}^2} \sin^2 \theta \right] \frac{\Delta \mu}{\mu} + \left[\frac{1}{2} - \frac{\sec^2 \theta}{4} \right] \frac{\Delta \rho}{\rho}, \quad (5.7)$$

where θ is the average between the incidence and refraction angles, $\Delta f/f$, $\Delta \mu/\mu$, and $\Delta \rho/\rho$ are the reflectivities and γ_{dry} and γ_{sat} represent average V_P/V_S ratios for dry and saturated media respectively. From chapter 4, two linear expressions for R_{PP} are shown, one is written in terms of perturbation and the other is written in terms of reflectivity. The first order poroelastic approximation for reflectivity contrasts is

$$R_{PP} \approx \left[\left(1 - \frac{(\gamma_0)_{dry}^2}{(\gamma_0)_{sat}^2} \right) \frac{(1 + \sin^2 \theta_0)}{4} \right] \frac{\Delta f}{f} + \left[\frac{(\gamma_0)_{dry}^2}{4(\gamma_0)_{sat}^2} (1 + \sin^2 \theta_0) - \frac{2}{(\gamma_0)_{sat}^2} \sin^2 \theta_0 \right] \frac{\Delta \mu}{\mu} + \left[\frac{1}{4} - \frac{\sin^2 \theta_0}{4} \right] \frac{\Delta \rho}{\rho}. \quad (5.8)$$

There are similarities between the Russell and Gray approximation and the first order poroelastic approximation where the weighting factors are nearly identical. Using a small angle

approximation on the first order approximation in equation (5.8) will show that it is consistent with Russell and Gray. Applying the small angle approximation on the three $\sin^2 \theta_0$ terms, can alter them to $\sec^2 \theta_0$. The small angle approximation for $\sec^2 \theta_0$ is written such that

$$\sec^2 \theta_0 \approx 1 + \sin^2 \theta_0, \quad (5.9)$$

which can be proven by

$$\sec^2 \theta_0 = \frac{1}{\cos^2 \theta_0} = \frac{1}{1 - \sin^2 \theta_0} = 1 + \sin^2 \theta_0 + \sin^4 \theta_0 + \dots .$$

By substituting the small angle approximation (5.9) into (5.8) the equation becomes

$$\begin{aligned} R_{PP} \approx & \left[\left(1 - \frac{(\gamma_0)_{\text{dry}}^2}{(\gamma_0)_{\text{sat}}^2} \right) \frac{\sec^2 \theta_0}{4} \right] \frac{\Delta f}{f} + \left[\frac{(\gamma_0)_{\text{dry}}^2}{4(\gamma_0)_{\text{sat}}^2} \sec^2 \theta_0 - \frac{2}{(\gamma_0)_{\text{sat}}^2} \sin^2 \theta_0 \right] \frac{\Delta \mu}{\mu} \\ & + \left[\frac{1}{2} - \frac{\sec^2 \theta_0}{4} \right] \frac{\Delta \rho}{\rho}. \end{aligned} \quad (5.10)$$

Equation (5.10) is the final result of the first order poroelastic AVO equation derived from the elastic Zoeppritz equations. The differences in the Russell and Gray approximation derived by Russell et al. (2011) and our first order approximation represented in equation (5.7) and (5.10) respectively, are between the parameters θ and θ_0 , γ_{dry} and $(\gamma_0)_{\text{dry}}$, and γ_{sat} and $(\gamma_0)_{\text{sat}}$. These differences in V_p/V_s ratios and plane wave angle show that the first order poroelastic AVO approximation requires only information from the incident medium while Russell et al.'s (2011) poroelastic approximation requires information from both layers. Otherwise, the first order poroelastic approximation and the Russell and Gray approximation are consistent.

5.4 Importance of low-order nonlinear poroelastic AVO: numerical study

In the following figures, AVO modeling is performed on scenarios consisting of two homogeneous layers separated by a horizontal interface. The top layer contains its own unique set of fluid, shear modulus, and density parameters as does the bottom layer. The numerical AVO results are calculated such that the poroelastic parameters (f , μ , ρ) are predetermined for medium 1 and the poroelastic parameters for the top layer depend on the selected perturbation (a_f , a_μ , a_ρ) or reflectivity ($\Delta f/f$, $\Delta\mu/\mu$, $\Delta\rho/\rho$) values chosen by the user.

For medium 1 the predetermined values are

$$\begin{aligned} f_1 &= 7.000 \text{ GPa}, \\ \mu_1 &= 3.000 \text{ GPa}, \\ \rho_1 &= 2.200 \text{ g/cm}^3. \end{aligned}$$

and medium 0 values are calculated using

$$\begin{aligned} f_0 &= f_1(1 - a_f) = f_1 \left(1 - \frac{\Delta f}{f} \left(1 + \frac{\Delta f}{2\Delta f} \right)^{-1} \right), \\ \mu_0 &= \mu_1(1 - a_\mu) = \mu_1 \left(1 - \frac{\Delta\mu}{\mu} \left(1 + \frac{\Delta\mu}{2\Delta\mu} \right)^{-1} \right), \\ \rho_0 &= \rho_1(1 - a_\rho) = \rho_1 \left(1 - \frac{\Delta\rho}{\rho} \left(1 + \frac{\Delta\rho}{2\Delta\rho} \right)^{-1} \right). \end{aligned}$$

Figure (5.1) shows perturbation-based AVO modeling using equations (5.1) – (5.3) where all three perturbation constants are equal as perturbation models increase simultaneously from Figures (5.1a) – (5.1d). Figure (5.1a) shows the reflection amplitudes based on small perturbation values $a_f = a_\mu = a_\rho = 0.100$. These perturbation values predict exact R_{PP} accurately. Figure (5.1b) shows the reflection amplitudes based on a 0.100 increase in

perturbation for each perturbation parameter such that $a_f = a_\mu = a_\rho = 0.200$. This increase in perturbation also increased the amplitude values across all approximations. An increase in perturbation to $a_f = a_\mu = a_\rho = 0.400$ shows a significant decrease in accuracy of the first order approximation as well as an accuracy decrease for the second order approximation in Figure (5.1c). Figure (5.1d) uses perturbation values of $a_f = a_\mu = a_\rho = 0.500$ and highlights a drop in accuracy of the first order approximation by more than 20% of the zero offset amplitude measurement and the third order approximation has a drop in accuracy less than 1% of the zero offset amplitude measurement.

Figure (5.2) shows reflectivity-based AVO modeling using equations (5.4) – (5.6) where all three reflectivity constants are equal as reflectivity models increase simultaneously, illustrated in Figures (5.2a) – (5.2d). These figures illustrate the same numerical approach as Figure (5.1) by using $\frac{\Delta f}{f} = \frac{\Delta \mu}{\mu} = \frac{\Delta \rho}{\rho} = 0.100$ for Figure (5.2a) and etc. In Figure (5.2a), the reflectivity parameters are small, $\frac{\Delta f}{f} = \frac{\Delta \mu}{\mu} = \frac{\Delta \rho}{\rho} = 0.100$. Reflectivity parameters of this magnitude show that the first, second and third order approximations are predicting exact R_{PP} correctly. This remains to be true as reflectivity in fluid, shear modulus, and density is increased from Figure (5.2b) – (5.2d). In the next two sets of figures, Figures (5.3) – (5.5) display a side-by-side comparison between the perturbation and reflectivity-modeled AVO curves.

Figure (5.3) shows a comparison of the performance of the perturbation based modeling and the reflectivity based modeling simultaneously. Figures (5.3a) and (5.3b) use parameter values of $a_f = \frac{\Delta f}{f} = 0.300$, $a_\mu = \frac{\Delta \mu}{\mu} = 0.100$, and $a_\rho = \frac{\Delta \rho}{\rho} = 0.100$. Figures (5.3c) and (5.3d) use

parameter values of $a_f = \frac{\Delta f}{f} = 0.100$, $a_\mu = \frac{\Delta \mu}{\mu} = 0.300$, and $a_\rho = \frac{\Delta \rho}{\rho} = 0.100$. Finally, Figures (5.3e) and (5.3f) use parameter values of $a_f = \frac{\Delta f}{f} = 0.100$, $a_\mu = \frac{\Delta \mu}{\mu} = 0.100$, and $a_\rho = \frac{\Delta \rho}{\rho} = 0.300$. Figures (5.3a), (5.3c) and (5.3e) show a decreasing amplitude trend from 0° to 30° incidence angle. The AVO curves produced in these figures highlight the effects that fluid, shear modulus and density contrasts have on these curves. All three figures show approximately 12% error for the first order approximation at zero offset and less than 1% error for the third order approximation also at zero offset. Figures (5.3b), (5.3d) and (5.3f) show small errors for first, second and third order approximations. The zero offset error is less than 1% for the first and third order approximations in all three figures.

Figures (5.4) and (5.5) illustrate the same type of numerical analysis as shown in Figure (5.3) but use larger contrasts. The larger contrasts emphasize the effects that fluid, shear modulus and density perturbation/reflectivity models have on the AVO curves by the decreasing accuracy of the approximations. In Figure (5.4), an increase in the single perturbation/reflectivity constant is measured to be 0.600. Doing so significantly affects the accuracy of the first, second and third order approximations in the perturbation domain. This is seen in Figures (5.4a), (5.4c), and (5.4e) where the zero offset amplitude measurement, compared to the first order approximation loses accuracy relative to exact R_{PP} by 33%, whereas the third order approximation has 9% error for the zero offset amplitude measurement. The reflectivity domain based equations however, remain largely unaffected. In Figure (5.5), another increase in the single perturbation/reflectivity constant is measured at 0.900 where this increase has brought another significant decrease in accuracy for first, second and third order approximations in the perturbation domain. The error of

the zero offset amplitudes for the first and third order approximations are very large but this is not the case for the reflectivity based approximations, where the first and third order approximations predict exact R_{PP} with 20% and 3% error respectively.

Figure (5.6) continues to compare the performance of the perturbation modeling and the reflectivity modeling but instead select models that differ from constant medium poroelastic property values. In other words, the analysis is performed such that f , μ , and ρ for both the upper and lower media remain constant while a_f , a_μ , a_ρ and $\Delta f/f$, $\Delta\mu/\mu$, $\Delta\rho/\rho$ are calculated accordingly. In Table (5.6), the perturbation values increase by increments of 0.200 from Figure (5.6a) – (5.6c) and (5.6c) – (5.6e). The reflectivity values however, increase by 0.278 from Figure (5.6b) – (5.6d) and another increase by 0.357 from Figure (5.6d) – (5.6f). Given that the values for f , μ , and ρ are comparatively analyzed in each pair of (5.6a), (5.6b), and (5.6c), (5.6d), and (5.6e), (5.6f), it is clear that the reflectivity domain equations are consistently more accurate than the perturbation based equations.

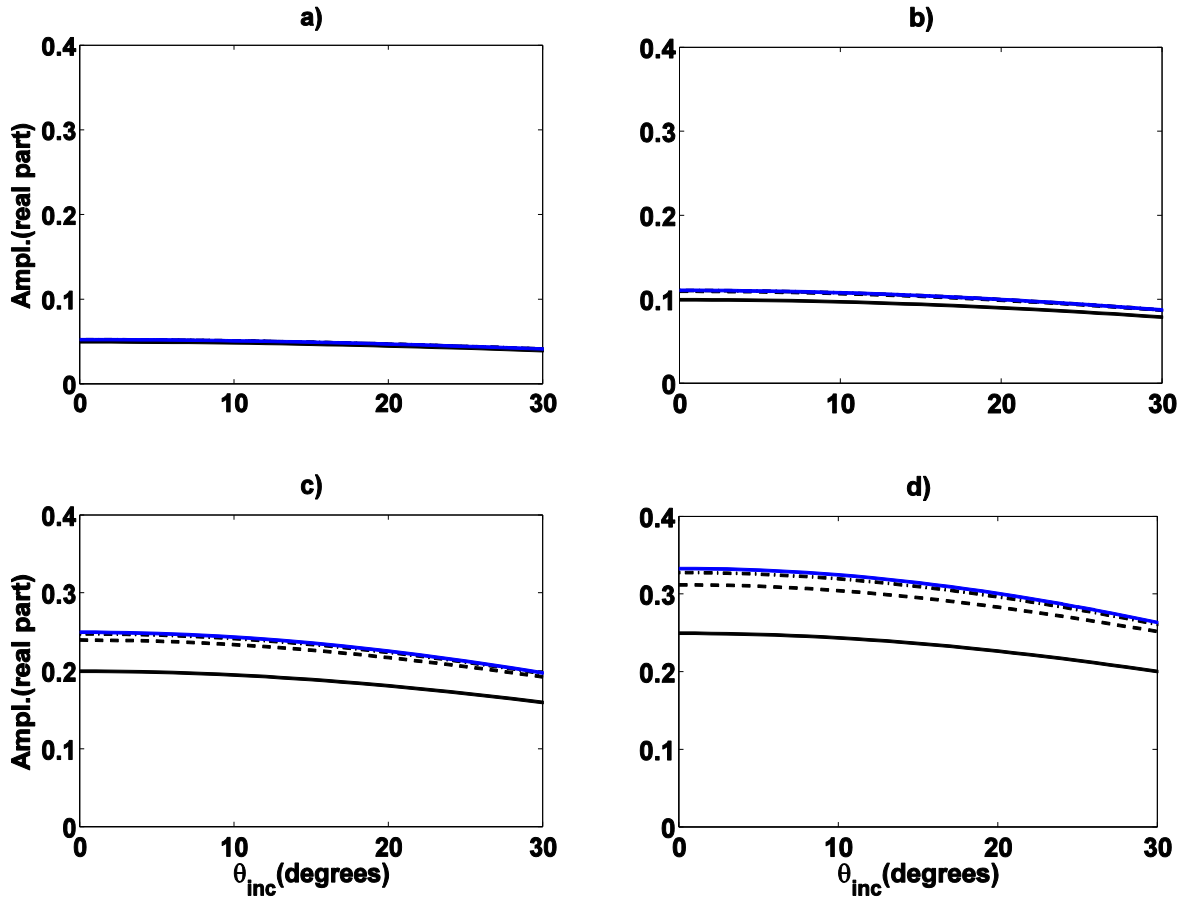


Figure 5.1: All four panels have a consistent perturbation each in a_f , a_μ , and a_ρ . Four curves are produced in each panel: the blue curve represents the exact solutions while the solid, dashed, and dash-dotted black curves represent the 1st, 2nd, and 3rd order approximations respectively.

Figures	Values for perturbations ($a_f = a_\mu = a_\rho$)
5.1a	0.100
5.1b	0.200
5.1c	0.400
5.1d	0.500

Table 5.1: Perturbation values from Figure (5.1).

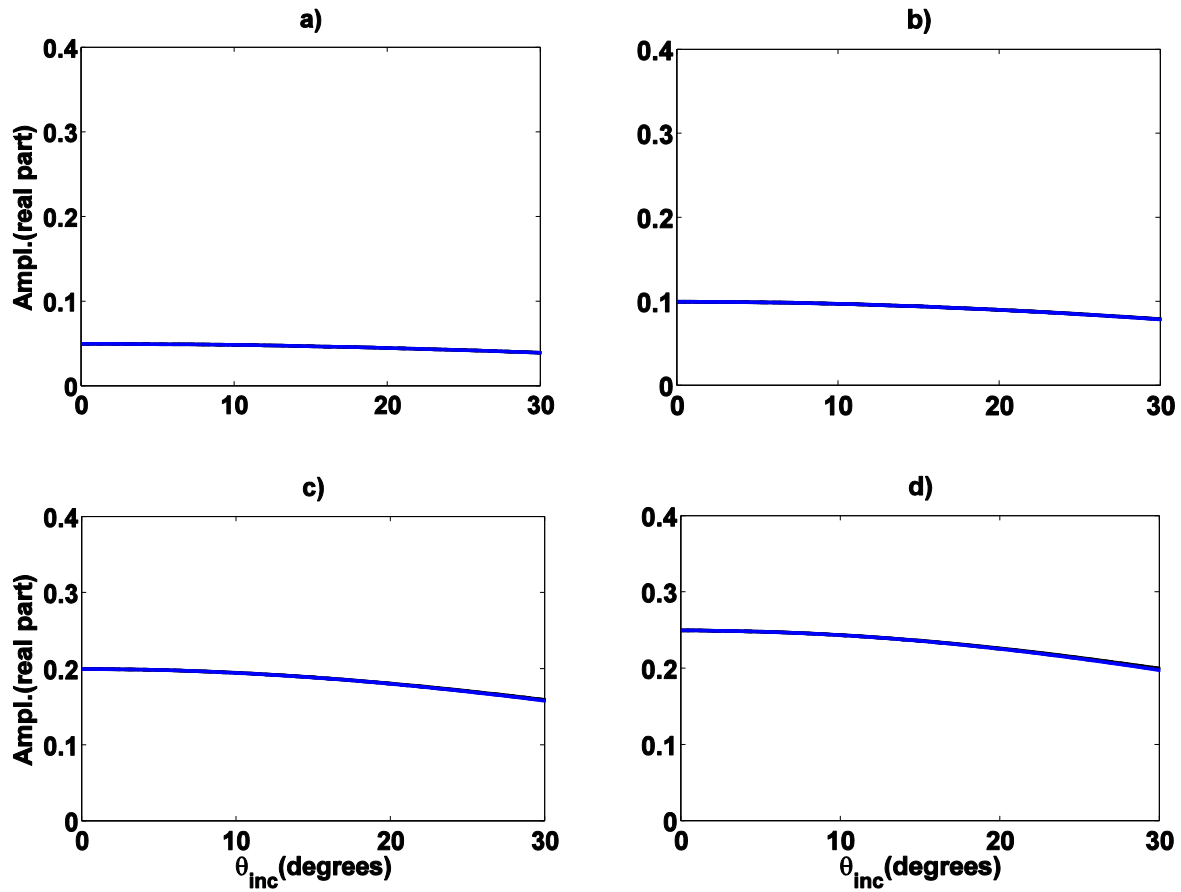


Figure 5.2: The four panels use a consistent reflectivity of $\Delta f/f$, $\Delta\mu/\mu$, and $\Delta\rho/\rho$ in each. Four curves are reproduced in each panel: the blue curve represents the exact solutions while the solid, dashed, and dash-dotted black curves represent the 1st, 2nd, and 3rd order approximations respectively.

Figures	Values for reflectivity ($\Delta f/f = \Delta\mu/\mu = \Delta\rho/\rho$)
5.2a	0.100
5.2b	0.200
5.2c	0.400
5.2d	0.500

Table 5.2: Reflectivity values from Figure (5.2).

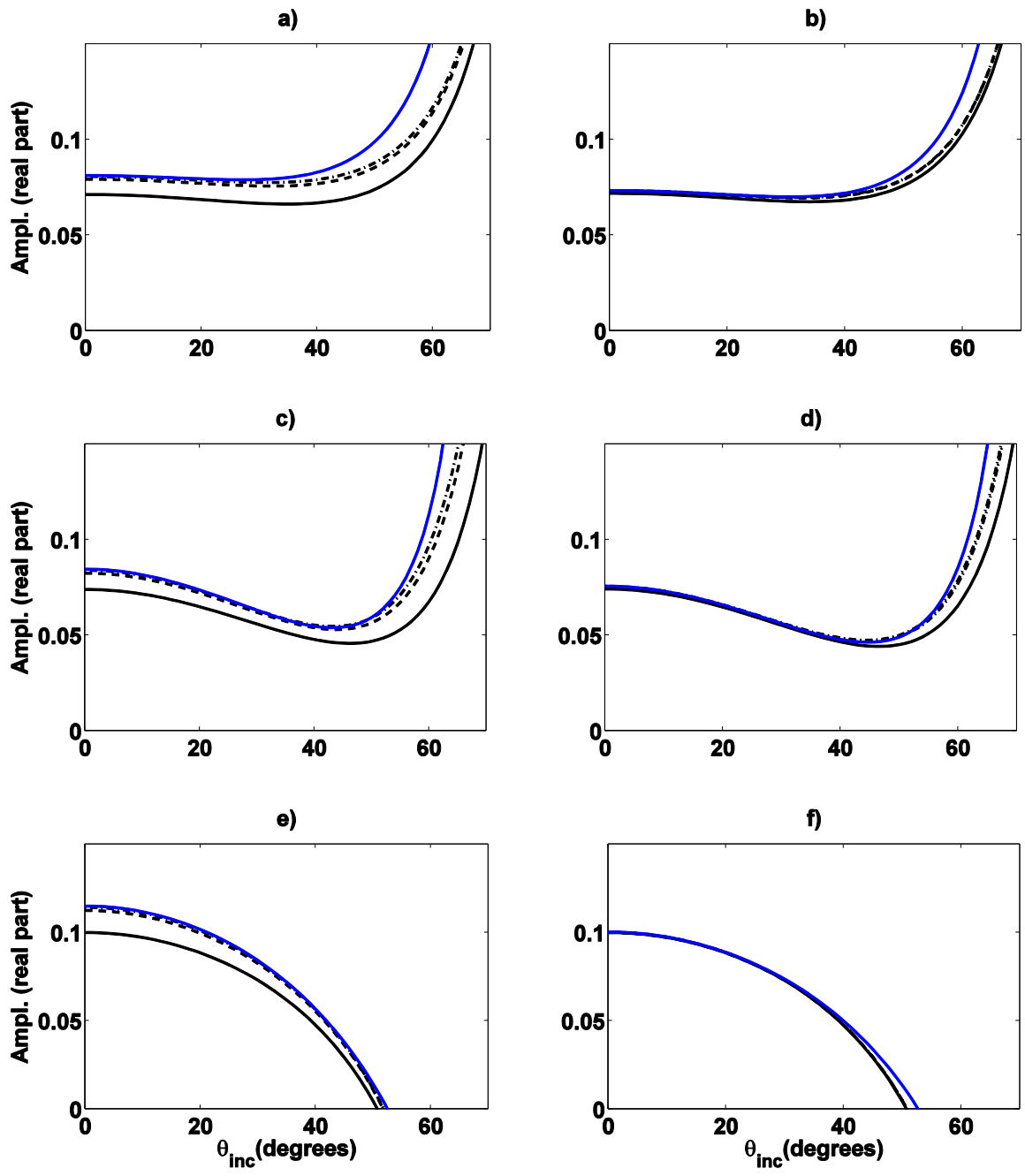


Figure 5.3: Figures (a), (c), and (e) represent the perturbation based poroelastic AVO approximations of 1st, 2nd, and 3rd order, as shown by the solid, dashed, and dash-dotted black curves respectively. Figures (b), (d), and (f) represent the reflectivity based poroelastic AVO approximations of 1st, 2nd, and 3rd order, as shown by the solid, dashed, and dash-dotted black curves respectively. The exact amplitudes are shown by the blue curve.

Figure	a_f	a_μ	a_ρ	Figure	$\Delta f/f$	$\Delta\mu/\mu$	$\Delta\rho/\rho$
5.3a	0.300	0.100	0.100	5.3b	0.300	0.100	0.100
5.3c	0.100	0.300	0.100	5.3d	0.100	0.300	0.100
5.3c	0.100	0.100	0.300	5.3f	0.100	0.100	0.300

Table 5.3: Values for perturbation and reflectivity for Figure (5.3).

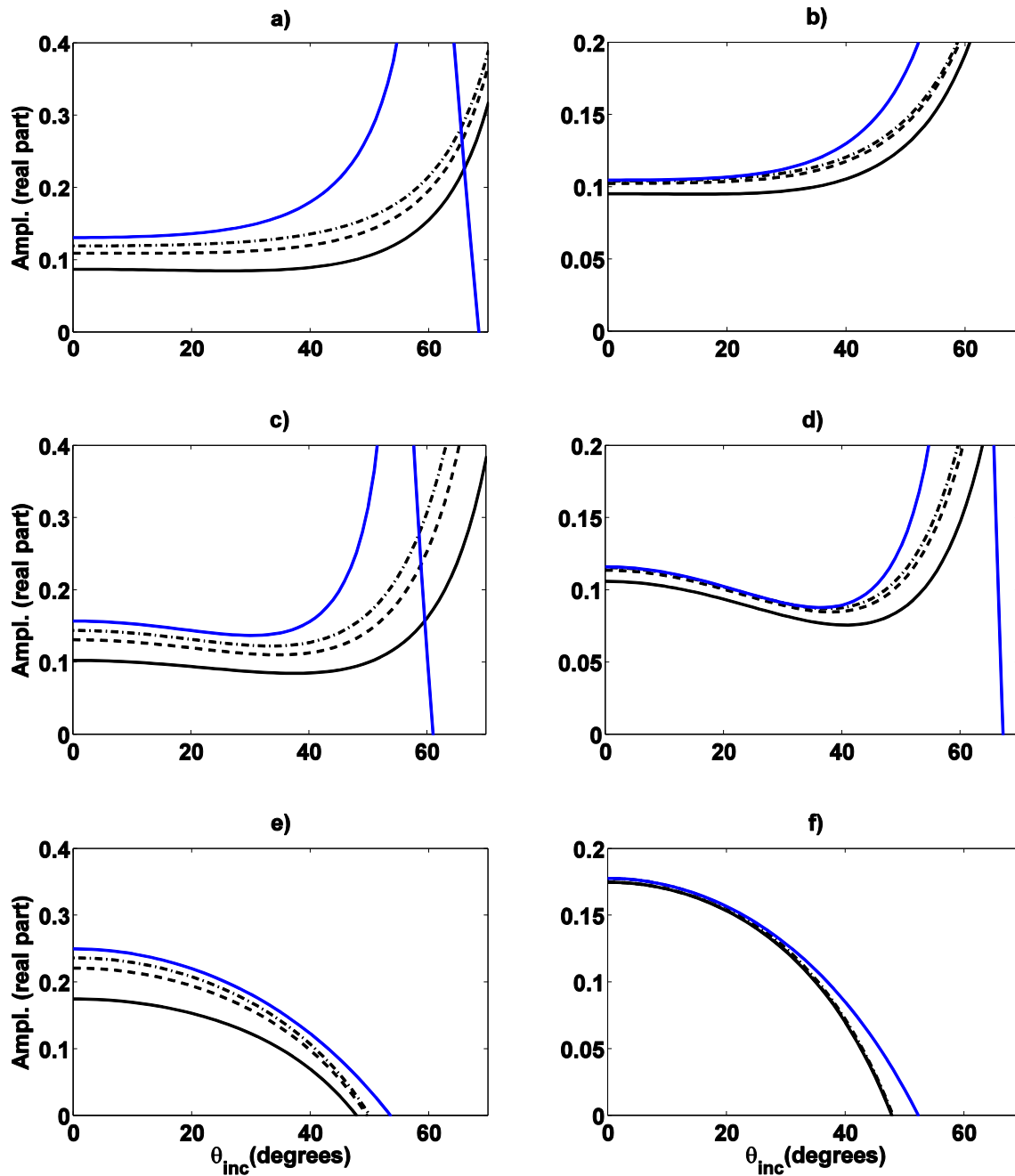


Figure 5.4: Figures (a), (c), and (e) represent the perturbation based poroelastic AVO approximations of 1st, 2nd, and 3rd order, as shown by the solid, dashed, and dash-dotted black curves respectively. Figures (b), (d), and (f) represent the reflectivity based poroelastic AVO approximations of 1st, 2nd, and 3rd order, as shown by the solid, dashed, and dash-dotted black curves respectively. The exact amplitudes are shown by the blue curve.

Figure	a_f	a_μ	a_ρ	Figure	$\Delta f/f$	$\Delta\mu/\mu$	$\Delta\rho/\rho$
5.4a	0.600	0.100	0.100	5.4b	0.600	0.100	0.100
5.4c	0.100	0.600	0.100	5.4d	0.100	0.600	0.100
5.4c	0.100	0.100	0.600	5.4f	0.100	0.100	0.600

Table 5.4: Values for perturbation and reflectivity for Figure (5.4).

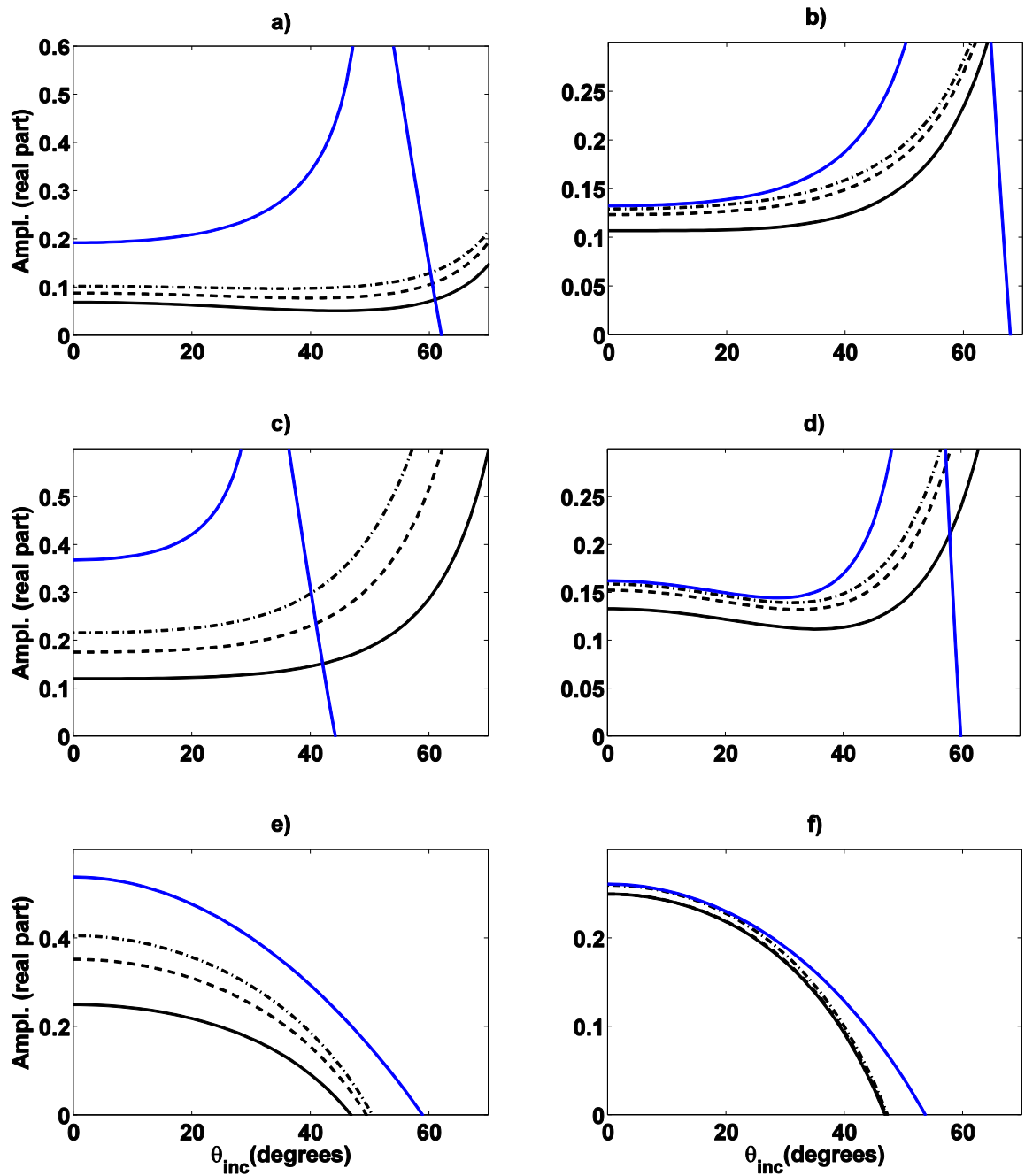


Figure 5.5: Figures (a), (c), and (e) represent the perturbation based poroelastic AVO approximations of 1st, 2nd, and 3rd order, as shown by the solid, dashed, and dash-dotted black curves respectively. Figures (b), (d), and (f) represent the reflectivity based poroelastic AVO approximations of 1st, 2nd, and 3rd order, as shown by the solid, dashed, and dash-dotted black curves respectively. The exact amplitudes are shown by the blue curve.

Figure	a_f	a_μ	a_ρ	Figure	$\Delta f/f$	$\Delta\mu/\mu$	$\Delta\rho/\rho$
5.5a	0.900	0.100	0.100	5.5b	0.900	0.100	0.100
5.5c	0.100	0.900	0.100	5.5d	0.100	0.900	0.100
5.5c	0.100	0.100	0.900	5.5f	0.100	0.100	0.900

Table 5.5: Values for perturbation and reflectivity for Figure (5.5).

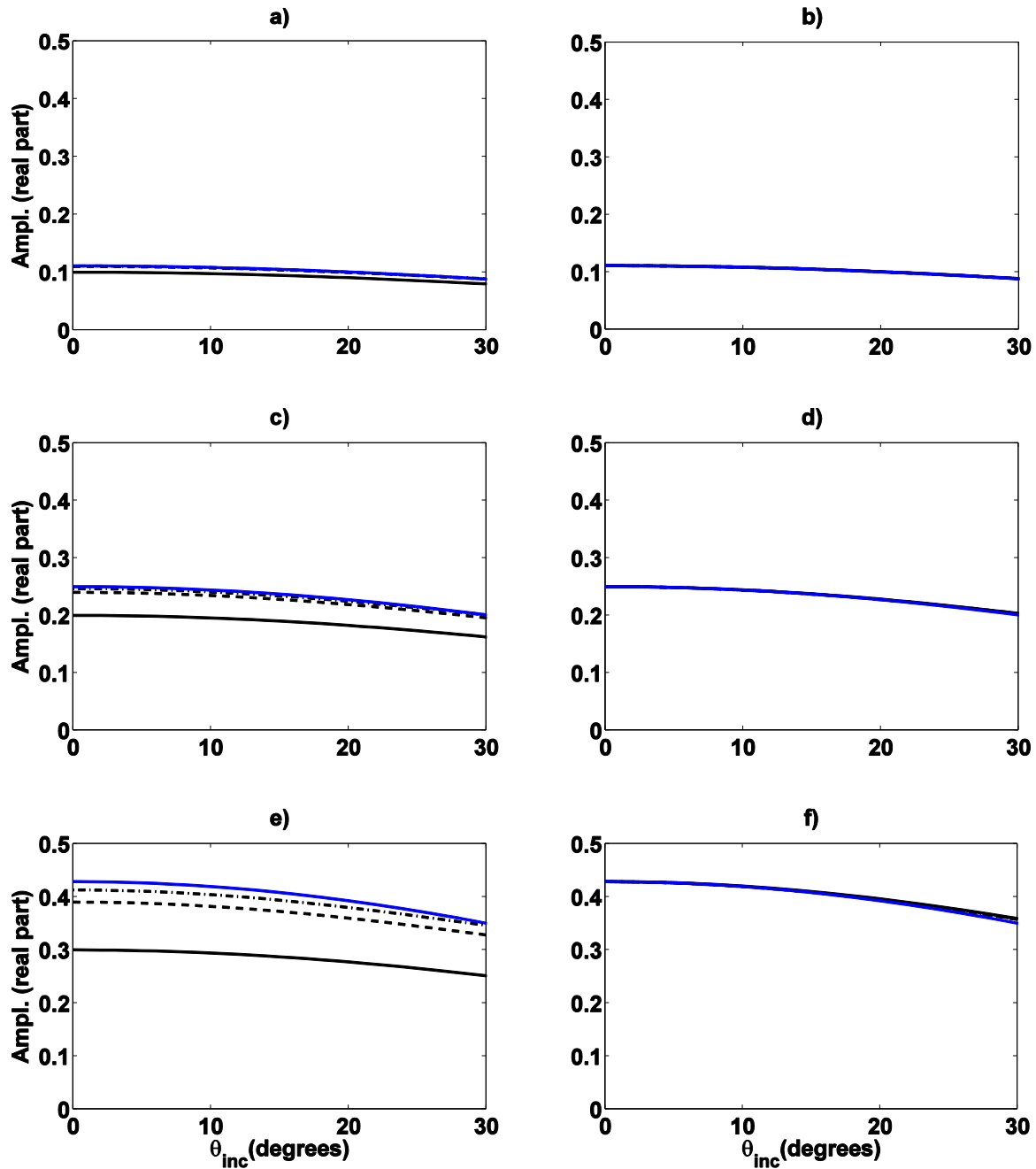


Figure 5.6: Figures (a), (c), and (e) represent the perturbation based poroelastic AVO approximations of 1st, 2nd, and 3rd order, as shown by the solid, dashed, and dash-dotted black curves respectively. Figures (b), (d), and (f) represent the reflectivity based poroelastic AVO approximations of 1st, 2nd, and 3rd order, as shown by the solid, dashed, and dash-dotted black curves respectively. The exact amplitudes are shown by the blue curve.

Figure	a_f	a_μ	a_ρ	Figure	$\Delta f/f$	$\Delta\mu/\mu$	$\Delta\rho/\rho$
5.6a	0.200	0.200	0.200	5.6b	0.222	0.222	0.222
5.6c	0.400	0.400	0.400	5.6d	0.500	0.500	0.500
5.6e	0.600	0.600	0.600	5.6f	0.857	0.857	0.857

Table 5.6: Values for perturbation and reflectivity for Figure (5.6).

5.5 Chapter summary

This chapter compares the first order approximation in reflectivity and compares it to Russell and Gray's approximation. The results validate our derivation methods. We then show the numerical results using the first, second and third order approximations with exact R_{PP} in both the perturbation and reflectivity domains as a guide to measure the accuracy of the approximations.

A variety of different numerical values were tested for AVO modeling. The first test shown in Figure (5.1) consisted of a constant perturbation value such that $a_f = a_\mu = a_\rho$. An increase in value for perturbation showed a steady decrease in accuracy for the first order approximation.

The second test in Figure (5.2) consisted of using a constant reflectivity value such that $\frac{\Delta f}{f} =$

$\frac{\Delta\mu}{\mu} = \frac{\Delta\rho}{\rho}$ where increasing the value for reflectivity showed consistently accurate predictions from

each of the reflectivity approximations. The numerical results following the first two tests

compared the results of perturbation approximations against reflectivity approximations using

various different numerical circumstances. It was consistently shown that the reflectivity models

provided more accurate results in all orders of approximation relative to the perturbation in AVO

modeling.

Chapter Six: Towards a more complete picture of poroelasticity

6.1 Chapter overview

The purpose of this chapter is to show the final results from the analysis of reflection and transmission coefficients in poroelastic media achieved by Gurevich et al. (2004). Background information discussed by Gurevich et al. (2004) will be mentioned in section 6.2. This will be followed by the study that Gurevich et al. (2004) provided for poroelastic reflection and transmission modeling from an incident P-wave in two scenarios; the first in a porous-porous medium and the other in a free fluid-porous medium. The equations for each medium will be shown in sections 6.3 and 6.4 respectively. Both sections will include the extent of our work which consists of re-writing the Gurevich equations using Russell et al. (2011) notation. Finally, the chapter will be closed with a summary.

6.2 An introduction to the Gurevich study

Hydrocarbon reservoirs as well as many other sedimentary rocks are fluid-saturated porous materials, with elastic properties that can be described by the theory of poroelasticity (Biot, 1962). This theory predicts the effects of movement of the pore fluid relative to the solid skeleton by seismic waves propagating through the rock (Gurevich et al., 2004). This opens potential opportunities to estimate fluid and rock transport properties from measurements of seismic waves (Gurevich et al., 2004). However, these opportunities are somewhat limited by the fact that, at low frequencies, relative fluid movement becomes negligible and the rock behaves like an elastic solid with elastic moduli equivalent to Gassmann's (1951) equations (Gurevich et al., 2004).

In particular, the theory of poroelasticity predicts that elastic wave attenuation and dispersion only become significant at frequencies comparable to the so-called Biot's characteristic frequency $\omega_c = \eta\phi/\kappa\rho_f$, where ϕ and κ are the porosity and permeability of the rock matrix respectively, and η and ρ_f are the steady-state shear viscosity and density of the pore fluid, respectively (Gurevich et al., 2004). For commonly encountered natural rocks such as sandstones or limestones saturated with water, oil or gas, ω_c is usually 0.1 MHz or higher. This is much higher than the frequency of waves of surface seismic exploration (20-70 Hz) and well logging (5-50 kHz). For frequencies much smaller than ω_c , both attenuation and dispersion are very small (Gurevich et al., 2004). However, White (1983) shows that dynamic poroelasticity effects may be pronounced at low frequencies when macroscopic heterogeneity is present in porous media (Gurevich et al., 2004). In other words, when a plane wave interacts with fluid across an interface, a loss of energy from that propagating wave occurs (Gurevich et al., 2004). This loss of energy is related to the calculation of the reflection coefficient, which is proportional to the square root of frequency in this particular environment. What this suggests is that we may be able to monitor fluid effects within porous media using reflection sounding at relatively low frequencies (Gurevich et al., 2004).

There are various parameterizations of reflection and transmission coefficients for poroelastic media. These expressions are also typically nonlinear. From an inversion perspective, nonlinearity causes instability when inverting for desired (predicted) components from the data. Therefore, we would like to present a framework of equations following Gurevich et al. (2004), namely normal incidence, frequency dependent, reflection/transmission coefficients. A linearized

form for these coefficients would provide a computationally faster measure of inverted poroelastic parameters.

Gurevich et al. (2004) derives normal incident reflection and transmission coefficients using two different geological scenarios. The first is a two-layer model that consists of a solid poroelastic medium overlying another solid poroelastic medium. This scenario produces two reflection coefficients R_{11} and R_{12} and two transmission coefficients T_{11} and T_{12} . The second geologic scenario consists of a solid poroelastic medium overlying a free fluid. This scenario produces one reflection coefficient R_{11} and two transmission coefficients T_{11} and T_{12} . The subscript '1' indicates propagation of a fast P-wave which we understand as $v = \sqrt{\frac{\lambda+2\mu}{\rho}}$ and subscript '2' indicates propagation of the Biot slow P-wave.

6.3 Reflection and transmission coefficients for porous-porous media

One set of expressions derived by Gurevich et al. (2004) is used to calculate reflection and transmission coefficients of an incident P-wave in fluid-saturated media for a two-layer case. As a result of the frequency dependent effect of porous media on calculating reflection and transmission coefficients, two P-waves are generated from an incident plane wave, $e^{i\omega t}$; a fast P-wave and a slow P-wave.

Figure (6.1) shows the schematic which Gurevich et al. (2004) uses in deriving the normal incidence reflection and transmission coefficients.

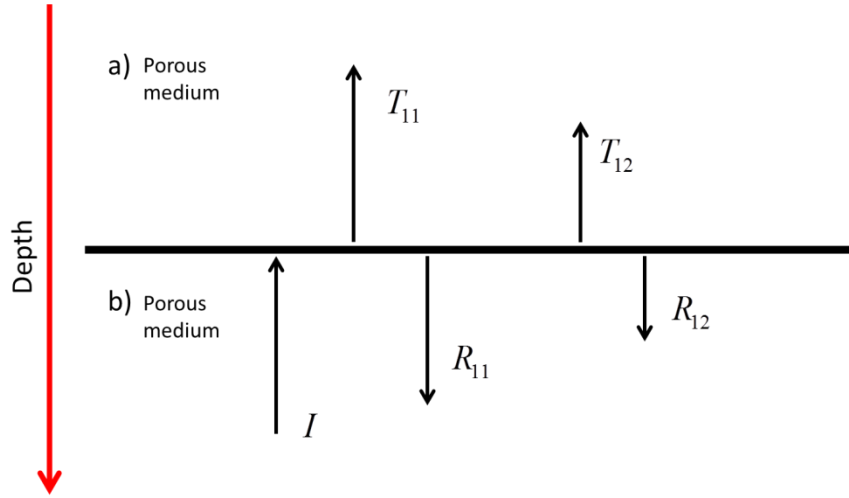


Figure 6.1: A representation of an incoming P-wave in layer b. The reflection and transmission coefficients are for P-waves only and the subscripts indicate a fast P-wave (1) and Biot's slow wave (2).

For a fast P-wave, corresponding reflection and transmission coefficients are produced, labelled R_{11} and T_{11} respectively. The Biot slow P-wave also produces a reflected and transmitted P-wave labelled R_{12} and T_{12} . For the fast P-wave, the expressions for the reflection and transmission coefficient are shown as

$$R_{11}(\omega) = \frac{\rho_1 v_1 - (1-X)\rho_0 v_0}{\rho_1 v_1 + (1+X)\rho_0 v_0}, \quad (6.1)$$

and

$$T_{11}(\omega) = \frac{2\rho_1 v_1}{\rho_1 v_1 + (1+X)\rho_0 v_0}. \quad (6.2)$$

At first glance, by setting $X = 0$, R_{11} and T_{11} are reverted back to their elastic forms. This implies that the X term contains all of the implicit poroelastic properties of the media. This X term will determine poroelastic variations in fluid and shear modulus while the density terms that

are outside of X will show the density variations. As shown by Gurevich et al. (2004) X is defined as

$$X(\omega) = \frac{H_1(k_1)_{\text{fast}} \left(\frac{C_0}{H_0} - \frac{C_1}{H_1} \right)^2}{(k_0)_{\text{slow}} N_0 + (k_1)_{\text{slow}} N_1}, \quad (6.3)$$

where the X term contains moduli that overlap with Russell et al. (2011). Since the research from previous chapters of this thesis use notation from Russell et al. (2011), this overlap will allow equation (6.3) to be written in terms of perturbations. This step would include substitution of α_f and α_μ for f_0/f_1 and μ_0/μ_1 ratios respectively.

Other terms such as steady-state shear viscosity of a fluid η or steady-state permeability of a solid skeleton κ , will be kept in their original notation as provided by Gurevich et al. (2004). The constants H , C , and N are

$$H = K_{\text{dry}} + \frac{4}{3} \mu + f, \quad (6.4)$$

$$C = \alpha M, \quad (6.5)$$

and

$$N = \frac{C}{\alpha} - \frac{C^2}{H}. \quad (6.6)$$

In H , K_{dry} is the bulk modulus of the skeleton framework, μ is the shear modulus, and f is the fluid term. The fluid term is also mentioned in chapter 2 where $f = \alpha^2 M$ where α is referred to as the Biot coefficient

$$\alpha = 1 - \frac{K_{\text{dry}}}{K_{\text{m}}},$$

and M is the modulus

$$M = \left(\frac{\alpha - \phi}{K_m} + \frac{\phi}{K_{fl}} \right)^{-1}.$$

This then leaves $(k)_{\text{slow}}$ and $(k)_{\text{fast}}$ which are expressions for wavenumbers corresponding to Biot's slow P-wave and fast P-wave respectively. These variables are left unchanged from Gurevich et al. (2004) and are described as

$$k_{\text{slow}} = \sqrt{\frac{i\omega\eta}{\kappa N}}, \quad (6.7)$$

where η represents steady-state shear viscosity of a pore fluid, κ is the steady-state permeability of a solid skeleton, $\omega = 2\pi f$ which is the angular frequency and

$$k_{\text{fast}} = \frac{\omega}{v}. \quad (6.8)$$

Substitution of equations (6.4) – (6.8) into (6.3) produces

$$X(\omega) = \frac{\left((K_1)_{\text{dry}} + \frac{4}{3}\mu_1 + f_1 \right) (k_1)_{\text{fast}} \left(\frac{\alpha_0 M_0}{(K_0)_{\text{dry}} + \frac{4}{3}\mu_0 + f_0} - \frac{\alpha_1 M_1}{(K_1)_{\text{dry}} + \frac{4}{3}\mu_1 + f_1} \right)^2}{\frac{N_0}{\sqrt{N_0}} \sqrt{\frac{i\omega\eta_0}{\kappa_0}} + \frac{N_1}{\sqrt{N_1}} \sqrt{\frac{i\omega\eta_1}{\kappa_1}}}, \quad (6.9)$$

where $\frac{N}{\sqrt{N}}$ is written as

$$\frac{N}{\sqrt{N}} = \frac{M \left(1 - \frac{f}{(K)_{\text{dry}} + \frac{4}{3}\mu + f} \right)}{\sqrt{M} \sqrt{1 - \frac{f}{(K)_{\text{dry}} + \frac{4}{3}\mu + f}}}. \quad (6.10)$$

Equation (6.9) contains instances of nonlinearity. There are squared terms as well as square root terms in f_1 and μ_1 that can be expanded in series. By substituting this newly formed equation for X back into R_{11} and T_{11} , expressions that are in terms of fluid, shear modulus, and density are now available for fast P-waves.

For slow P-waves, the reflection and transmission coefficients are

$$R_{12}(\omega) = \frac{2X'_1 \rho_0 v_0}{\rho_1 v_1 + (1+X) \rho_0 v_0}, \quad (6.11)$$

and

$$T_{12}(\omega) = \frac{2X'_0 \rho_0 v_0}{\rho_1 v_1 + (1+X) \rho_0 v_0}. \quad (6.12)$$

In these two expressions, the X'_0 and X'_1 terms are expressed as

$$X'_0(\omega) = \frac{X}{\frac{H_0}{C_0} \left(\frac{C_0}{H_0} - \frac{C_1}{H_1} \right)}, \quad (6.13)$$

and

$$X'_1(\omega) = \frac{X}{\frac{H_1}{C_1} \left(\frac{C_0}{H_0} - \frac{C_1}{H_1} \right)}. \quad (6.14)$$

After substituting equations (6.4) – (6.5) into (6.13) and (6.14), X'_0 and X'_1 become

$$X'_0(\omega) = \frac{X}{\frac{(K_0)_{\text{dry}} + \frac{4}{3} \mu_0 + f_0}{\alpha_0 M_0} \left(\frac{\alpha_0 M_0}{(K_0)_{\text{dry}} + \frac{4}{3} \mu_0 + f_0} - \frac{\alpha_1 M_1}{(K_1)_{\text{dry}} + \frac{4}{3} \mu_1 + f_1} \right)}, \quad (6.15)$$

and

$$X'_1(\omega) = \frac{X}{\frac{(K_1)_{\text{dry}} + \frac{4}{3}\mu_1 + f_1}{\alpha_1 M_1} \left(\frac{\alpha_0 M_0}{(K_0)_{\text{dry}} + \frac{4}{3}\mu_0 + f_0} - \frac{\alpha_1 M_1}{(K_1)_{\text{dry}} + \frac{4}{3}\mu_1 + f_1} \right)}, \quad (6.16)$$

which both equivalently have f_1 and μ_1 dependencies as X does. Finally, expressions for R_{11} , T_{11} , R_{12} , T_{12} are expressed in terms of f , μ , and ρ .

6.4 Reflection and transmission coefficients for free fluid-porous media

Shown in the previous geological case of a porous medium overlying a porous medium, similar observations of the reflection and transmission coefficient expressions are made again for the case of a porous medium overlying a free fluid. For instance, the equation for R_{11} is defined by impedances of both layers with a $(1 - X)$ embedded in the numerator and the denominator to allow for fluid compensated effects. When $X = 0$, the equations for R_{11} and T_{11} have been reduced to their elastic forms and the fluid and shear modulus constants are contained within X .

Figure (6.2) represents the case where the incident P-wave pulse begins its propagation in layer b) and travels in the negative depth direction. The only difference between this figure and Figure (6.1) is the lack of R_{12} . One reason for this difference is the lack of a R_{12} amplitude in the displacement vectors shown by Gurevich et al. (2004). The expressions for the reflection and transmission coefficients for a fast P-wave are similarly constructed in equations (6.1) and (6.2) with a key difference is that the modulus contains all of the physical poroelastic information. This was expressed as X for a porous-porous medium and is expressed as Y for a free fluid-

porous medium. The reflection and transmission coefficients for fast P-waves in a free fluid-porous medium are

$$R_{11}(\omega) = \frac{\rho_1 v_1 - (1-Y)\rho_0 v_0}{\rho_1 v_1 + (1+Y)\rho_0 v_0}, \quad (6.17)$$

and

$$T_{11}(\omega) = \frac{2\rho_1 v_1}{\rho_1 v_1 + (1+Y)\rho_0 v_0}, \quad (6.18)$$

where Y is described as

$$Y(\omega) = \left(\frac{C_0}{H_0} - 1 \right)^2 \sqrt{-\frac{i\omega\kappa_0}{\eta_0 N_0}} \rho_1 v_1. \quad (6.19)$$

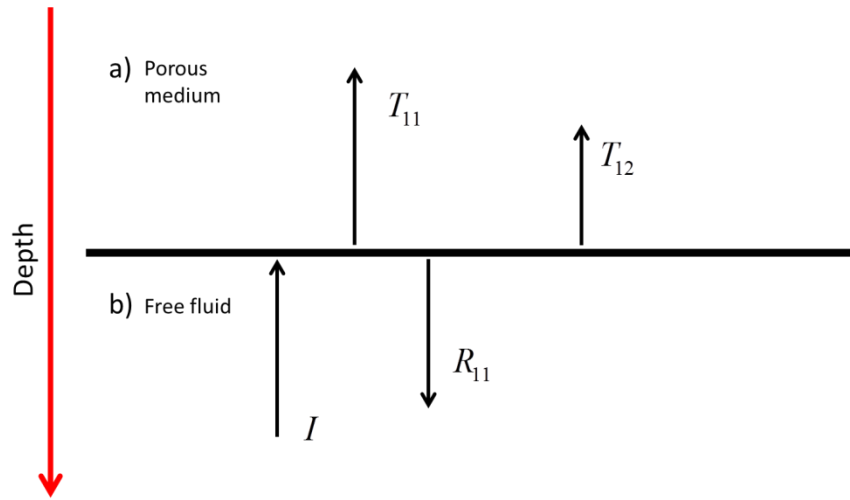


Figure 6.2: A second representation of an incoming P-wave in a free fluid occupying layer b. The reflection and transmission coefficients are for P-waves only and the subscripts indicate a fast P-wave (1) and Biot's slow wave (2).

By inspection, equation (6.19) is a reduced form of (6.3). This occurs by replacing the bottom layer with a free fluid ($H_1 = C_1 = K_1$) and the assumption of infinite permeability (κ) of the

free fluid (Gurevich et al., 2004). Using Russell et al's (2011) notation C , H , and N are explicitly shown in the poroelastic modulus Y to obtain

$$Y(\omega) = \left(\frac{\alpha_0 M_0}{(K_0)_{\text{dry}} + \frac{4}{3} \mu_0 + f_0} - 1 \right)^2 \left(1 - \frac{f_0}{(K_0)_{\text{dry}} + \frac{4}{3} \mu_0 + f_0} \right)^{-1/2} \sqrt{-\frac{i\omega\kappa_0}{\eta_0 M_0}} \rho_1 v_1. \quad (6.20)$$

Since only f_0 and μ_0 are shown in Y , this determines that neither fluid contrasts nor shear modulus contrasts will affect R_{11} or T_{11} . Only one instance of ρ_1 appears in Y which shows that there are perturbations of density in R_{11} and T_{11} . Thus for incidence P-waves traveling in a free fluid that interacts with a boundary of a porous medium, R_{11} and T_{11} contain only a density perturbation.

For the Biot slow wave, the transmission coefficient is

$$T_{12}(\omega) = \frac{2Y' \rho_0 v_0}{\rho_1 v_1 + (1+Y) \rho_0 v_0}, \quad (6.21)$$

where the slow P-wave induces a modified poroelastic variable, Y' , which is a reduced expression of X'_0

$$Y'(\omega) = \frac{Y}{1 - \frac{H_0}{C_0}} = \frac{C_0}{H_0} \left(\frac{C_0}{H_0} - 1 \right) \sqrt{-\frac{i\omega\kappa_0}{\eta_0 N_0}} \rho_1 v_1. \quad (6.22)$$

Since it appears that Y' also does not contain any dependence on a fluid or shear modulus perturbation, T_{12} is also only dependent on a density perturbation. Again, by explicitly replacing C , H , and N into forms that are in terms of f and μ , Y' becomes

$$\begin{aligned}
Y'(\omega) = & \frac{\alpha_0 M_0}{(K_0)_{\text{dry}} + \frac{4}{3} \mu_0 + f_0} \left(\frac{\alpha_0 M_0}{(K_0)_{\text{dry}} + \frac{4}{3} \mu_0 + f_0} - 1 \right) \\
& \times \left(1 - \frac{f_0}{(K_0)_{\text{dry}} + \frac{4}{3} \mu_0 + f_0} \right)^{-1/2} \sqrt{-\frac{i\omega\kappa_0}{\eta_0 M_0}} \rho_1 v_1.
\end{aligned} \tag{6.23}$$

6.5 Chapter summary

This chapter shows how to write the Gurevich reflection and transmission coefficients in terms of the Russell et al. (2011) notation. The next step following this Gurevich study will be to transition the poroelastic parameters f , μ and ρ into perturbations. Once they are in perturbations, a Taylor series expansion can be applied to R_{11} and R_{12} such that they are in series in orders of a_f , a_μ and a_ρ .

Chapter Seven: Conclusions

7.1 Summary

7.1.1 Review of AVO poroelasticity

Amplitude variation with offset is a useful tool to predict lithological properties using seismic signals. Knott (1899) and Zoeppritz (1919) each provide a set of equations that precisely calculate plane wave amplitudes. Koefoed (1955) demonstrates several examples using the Knott (1899) formulation to show that hydrocarbons may be detected by changes in measurement of Poisson's ratio across an interface. Koefoed (1955) uses a two-layer model using various velocity, density, and Poisson's ratios. Like Koefoed (1955), Richards (1961) performs amplitude analysis using the Zoeppritz equations to show several AVO curves that model a Paleozoic limestone in Western Canada. During the period that Koefoed and Richards published their work, calculation of either the Zoeppritz equations or the Knott equations required much time and patience.

The Zoeppritz equations are highly complex to interpret analytically. Linearization of these equations resulted from this complexity. There are examples in literature that demonstrate this (Fatti et al., 1994; Gray, 1999; Aki and Richards, 2002; Russell et al., 2011). One is the Russell and Gray approximation, parameterized in terms of fluid, shear modulus, and density (f , μ , ρ). Russell et al. (2011) derived from the Aki and Richards' approximation, a way to extract three poroelastic parameters from PP reflection data by showing how to solve for a linearized R_{PP} written in terms of the fluid term (f), saturated shear modulus (μ), and saturated density (ρ). . The Russell and Gray approximation, which provides alternative approximations for poroelastic AVO modeling, is the motivation behind this thesis. Here the approximations come in the form

of first, second and third-ordered corrective terms that measure poroelastic changes across a boundary. As opposed to the derivation methods presented by Russell et al. (2011), the methods presented in this thesis are shown as a sequence of mathematical processes to manipulate the elastic Zoeppritz equations formally produce exact forms of poroelastic PP reflection coefficients using poroelastic parameters f , μ and ρ .

7.1.2 Exact expressions for poroelastic R_{PP} , R_{PS} , R_{SS} , R_{SP}

Deriving exact expressions for PP, PS, SS and SP poroelastic reflection coefficients begins by analysis of the Zoeppritz equations, derived from the displacement amplitude equations.

After an incident P- or S-wave encounters an interface at an oblique angle θ , P and S reflections and transmissions are expected as a result of the encounter. One incident P-wave approaching the interface generates one PP reflection, one PS reflection, one PP transmission, and one PS transmission. One incident S-wave approaching the interface generates one SS reflection, one SP reflection, one SS transmission, and one SP transmission. Considering incident plane waves from below the boundary doubles the number of these reflections and transmissions. The relationships of these waves can be determined with the displacement amplitude equations as shown by Aki and Richards (2002). From these equations, a convenient matrix-notated form of the Zoeppritz equations may be solved for R_{PP} , R_{PS} , T_{PP} , and T_{PS} for incident P-waves, and R_{SS} , R_{SP} , T_{SS} , and T_{SP} for incident S-waves. Since surface seismic experiments observe up-going reflection amplitudes, incident plane waves are typically considered approaching the interface above the boundary.

The contents of this thesis explicitly show the analytical forms for elastic wave displacement amplitudes from incident P- and S-waves. These forms are referred to as the P- and S-wave Zoeppritz equations. Poroelastic parameters (f, μ, ρ) are substituted for the elastic ones (V_P, V_S, ρ) in both equations. This gives the poroelastic P- and S-wave Zoeppritz equations parameterized in $(f_0, \mu_0, \rho_0, f_1, \mu_1, \rho_1, \sin \theta_0)$. These equations model poroelastic amplitudes in the same way the elastic Zoeppritz equations model elastic amplitudes.

7.1.3 Series solutions for poroelastic R_{PP}

Although these equations account for poroelastic variations, the nonlinearity of the Zoeppritz equations can be an issue. The Russell and Gray approximation is a linearized expression, one of many examples that can model AVO and estimate model parameters effectively. Real seismic data is subject to nonlinear effects such as a combination of scatter, heat loss and anisotropy. Therefore, an extension to Russell et al. (2011) is provided by adding nonlinear terms to the Russell and Gray approximation. As previously mentioned above, this will be accomplished by re-parameterizing the Zoeppritz equations in terms of poroelastic parameters (f, μ, ρ) and by completing a sequence of mathematical processes. In order to achieve series solutions of R_{PP} , a few steps need to be accomplished. Those steps are:

- 1) Transition from poroelastic Zoeppritz equations by substituting parameters $f_0, \mu_0, \rho_0, f_1, \mu_1,$ and ρ_1 with parameters of perturbation $a_f, a_\mu,$ and a_ρ . This is performed by looking for instances of poroelastic ratios such as $\left(\frac{\mu_1}{\mu_0}\right)\left(\frac{\rho_0}{\rho_1}\right)$ and $\left(\frac{\rho_0}{\rho_1}\right)\left(\frac{s_1+f_1}{s_0+f_0}\right)$ that are found in the A_{ij} and a_i elements in \mathbf{P} and \mathbf{m}_P of the poroelastic P-wave Zoeppritz equations.

- 2) Taylor expand A_{ij} and a_i elements in in orders of $\sin^2 \theta_0$, a_f , a_μ , and a_ρ . This step eliminates any perturbation parameters that are nonlinear in those elements.
- 3) The final step is to apply Cramer's rule which solves for R_{PP} and calculates the determinant of ratios of augmented \mathbf{P} and un-augmented \mathbf{P} .

After the third step, an exact form for R_{PP} has been determined in the perturbation domain. The series solutions for R_{PP} can similarly be accomplished for reflectivity parameters, which requires repeating the three steps shown above but by replacing a_f , a_μ , a_ρ with $\Delta f/f$, $\Delta\mu/\mu$, $\Delta\rho/\rho$ in the first two steps. If the exact form for R_{PP} has already been determined in perturbation, an alternative approach to solving a series solution in reflectivity is possible.

7.1.4 Analytic and numerical validation

In chapter 5, a comparison is made between the first order poroelastic R_{PP} with the Russell and Gray approximation. The purpose of this comparison is validation. The Russell and Gray approximation is derived from the Aki and Richards's approximation and is solved by using the definition for fluid $f = \rho V_P^2 - \gamma_{dry}^2 \rho V_S^2$ and the chain rule of f such that $\Delta f = \frac{\partial f}{\partial V_P} \Delta V_P + \frac{\partial f}{\partial V_S} \Delta V_S + \frac{\partial f}{\partial \rho} \Delta \rho$. With these two definitions, Russell and Gray are able to derive an expression for PP reflection coefficients.

The approach to derive a first order poroelastic approximation begins by modifying the elastic constants V_P , V_S , ρ into either poroelastic reflectivity parameters $\Delta f/f$, $\Delta\mu/\mu$, $\Delta\rho/\rho$ or poroelastic perturbation parameters a_f , a_μ , a_ρ in each of the A_{ij} elements of the Zoeppritz

equations. These elements are then expanded in terms of $\sin^2 \theta_0$, $\Delta f/f$, $\Delta\mu/\mu$, and $\Delta\rho/\rho$ or $\sin^2 \theta_0$, a_f , a_μ , and a_ρ . Once complete, Cramer's rule is applied in order to solve for an exact form of R_{PP} .

A comparison between the Russell and Gray approximation and the first order poroelastic R_{PP} approximation ultimately shows that they are equivalent. This validates the technique used for deriving the exact poroelastic R_{PP} equation. A truncation of this expression may provide linear or nonlinear approximations of R_{PP} . These nonlinear terms are investigated for second and third order variations in R_{PP} . First $(R_{PP}(\theta_0) \approx R_{PP}^{(1)})$, second $(R_{PP}(\theta_0) \approx R_{PP}^{(1)} + R_{PP}^{(2)})$ and third $(R_{PP}(\theta_0) \approx R_{PP}^{(1)} + R_{PP}^{(2)} + R_{PP}^{(3)})$ order approximations are explicitly shown for reflectivity and perturbation. Numerical analysis is performed between these two sets of approximations for various a_f , a_μ , and a_ρ values for the first set and $\Delta f/f$, $\Delta\mu/\mu$, and $\Delta\rho/\rho$ for the second set. It is clear that the third order approximation is better at predicting amplitudes than the first and second order approximations. Moreover, the reflectivity approximations are able to handle larger poroelastic contrasts than the perturbation approximations.

7.1.5 Dynamic poroelasticity

Gurevich et al. (2004) shows how to derive normal incident reflection and transmission coefficients in poroelastic media. Dynamic poroelasticity involves a frequency dependence of these amplitude coefficients and is highly complex even for the simplest, normal incident case. Gurevich et al. (2004) uses two different geological models to model frequency dependent, normal incident amplitudes. The first geological model involves a porous solid overlying another

porous solid, and the second geological model involves a porous solid overlying a free fluid.

Plane wave propagation in both models comes from an incident P-wave, $e^{i\omega t}$, that begins in the lower medium and propagates upwards toward the boundary. In the first model, this creates reflection and transmission coefficients R_{11} , R_{12} , T_{11} , and T_{12} respectively. In the second model, reflection and transmission coefficients R_{11} , T_{11} , and T_{12} are generated. The subscripts of R and T indicate the P-wave type. The subscript '1' indicates a fast P-wave written as $v = \sqrt{\frac{\lambda+2\mu}{\rho}}$ and '2' is the Biot slow P-wave.

In the first model, the fast P-wave reflection and transmission coefficients take the form

$$R_{11}(\omega) = \frac{\rho_1 v_1 - (1-X)\rho_0 v_0}{\rho_1 v_1 + (1+X)\rho_0 v_0}, \quad (7.1)$$

and

$$T_{11}(\omega) = \frac{2\rho_1 v_1}{\rho_1 v_1 + (1+X)\rho_0 v_0}, \quad (7.2)$$

respectively. If $X = 0$ in equations (7.1) and (7.2), they would reduce to the elastic forms under normal incidence conditions. Therefore X , which is a function of ω and also contains all of the poroelastic constituents, is written as

$$X(\omega) = \frac{\left((K_1)_{\text{dry}} + \frac{4}{3}\mu_1 + f_1 \right) (k_1)_{\text{fast}} \left(\frac{\alpha_0 M_0}{(K_0)_{\text{dry}} + \frac{4}{3}\mu_0 + f_0} - \frac{\alpha_1 M_1}{(K_1)_{\text{dry}} + \frac{4}{3}\mu_1 + f_1} \right)^2}{\frac{N_0}{\sqrt{N_0}} \sqrt{\frac{i\omega\eta_0}{\kappa_0}} + \frac{N_1}{\sqrt{N_1}} \sqrt{\frac{i\omega\eta_1}{\kappa_1}}},$$

where η and κ are the steady-state shear viscosity of a fluid and the steady-state permeability of a material skeleton respectively, $(K)_{\text{dry}}$ is the bulk modulus of the skeleton framework, μ is the shear modulus, f is the fluid term, $(k)_{\text{fast}} = \omega/v$, ω is the angular frequency, α is the Biot coefficient, M is a poroelastic modulus, and N/\sqrt{N} contains poroelastic parameters such that

$$\frac{N}{\sqrt{N}} = \frac{M \left(1 - \frac{f}{(K)_{\text{dry}} + \frac{4}{3}\mu + f} \right)}{\sqrt{M} \sqrt{1 - \frac{f}{(K)_{\text{dry}} + \frac{4}{3}\mu + f}}}.$$

The Biot slow P-wave reflection and transmission coefficients are

$$R_{12}(\omega) = \frac{2X'_1 \rho_0 v_0}{\rho_1 v_1 + (1+X) \rho_0 v_0}, \quad (7.3)$$

and

$$T_{12}(\omega) = \frac{2X'_0 \rho_0 v_0}{\rho_1 v_1 + (1+X) \rho_0 v_0}, \quad (7.4)$$

where R_{12} and T_{12} contain the term X'_1 and X'_0 respectively. X'_0 and X'_1 take the form

$$X'_0(\omega) = \frac{X}{\frac{(K_0)_{\text{dry}} + \frac{4}{3}\mu_0 + f_0}{\alpha_0 M_0} \left(\frac{\alpha_0 M_0}{(K_0)_{\text{dry}} + \frac{4}{3}\mu_0 + f_0} - \frac{\alpha_1 M_1}{(K_1)_{\text{dry}} + \frac{4}{3}\mu_1 + f_1} \right)},$$

and

$$X'_1(\omega) = \frac{X}{\frac{(K_1)_{\text{dry}} + \frac{4}{3}\mu_1 + f_1}{\alpha_1 M_1} \left(\frac{\alpha_0 M_0}{(K_0)_{\text{dry}} + \frac{4}{3}\mu_0 + f_0} - \frac{\alpha_1 M_1}{(K_1)_{\text{dry}} + \frac{4}{3}\mu_1 + f_1} \right)},$$

which contain the X term in the numerator in both equations. One observation concludes that R_{12} and T_{12} are more analytically complex than R_{11} and T_{11} .

In the second geological model, the fast P-wave reflection and transmission coefficients are

$$R_{11}(\omega) = \frac{\rho_1 v_1 - (1-Y)\rho_0 v_0}{\rho_1 v_1 + (1+Y)\rho_0 v_0}, \quad (7.5)$$

and

$$T_{11}(\omega) = \frac{2\rho_1 v_1}{\rho_1 v_1 + (1+Y)\rho_0 v_0}. \quad (7.6)$$

Similar to equations (7.1) and (7.2), R_{11} and T_{11} are reduced to their elastic forms if $Y = 0$ and thus Y contains all of the poroelastic elements and is shown as

$$Y(\omega) = \left(\frac{\alpha_0 M_0}{(K_0)_{\text{dry}} + \frac{4}{3}\mu_0 + f_0} - 1 \right)^2 \left(1 - \frac{f_0}{(K_0)_{\text{dry}} + \frac{4}{3}\mu_0 + f_0} \right)^{-1/2} \sqrt{-\frac{i\omega\kappa_0}{\eta_0 M_0}} \rho_1 v_1.$$

This explicit form for Y indicates that perturbation in fluid and shear modulus cannot be written as no instances of f_1 nor μ_1 constants exist to create poroelastic ratios. There is only a single instance that ρ_1 appears which suggests that a density perturbation a_ρ appears in R_{11} and T_{11} for the second model. This shows that, in a circumstance where an incident P-wave is travelling through a free fluid and interacts with a boundary of a porous solid, only density contrasts will affect the amplitudes at normal incidence.

The Biot slow P-wave transmission coefficient is

$$T_{12}(\omega) = \frac{2Y'\rho_0v_0}{\rho_1v_1 + (1+Y)\rho_0v_0}, \quad (7.7)$$

where Y' is written as

$$Y'(\omega) = \frac{\alpha_0 M_0}{(K_0)_{\text{dry}} + \frac{4}{3}\mu_0 + f_0} \left(\frac{\alpha_0 M_0}{(K_0)_{\text{dry}} + \frac{4}{3}\mu_0 + f_0} - 1 \right) \times \left(1 - \frac{f_0}{(K_0)_{\text{dry}} + \frac{4}{3}\mu_0 + f_0} \right)^{-1/2} \sqrt{-\frac{i\omega\kappa_0}{\eta_0 M_0}} \rho_1 v_1.$$

Since Y' does not contain f_1 , μ_1 and one ρ_1 constant as for Y , Y' is also dependent only on the density perturbation.

7.2 Key outcomes of the study

One key outcome of this research is the production of linear and nonlinear poroelastic AVO approximations for PP reflection models. For the linear case, this equation is validated by comparison with the Russell and Gray equation shown by Russell et al. (2011). This validation shows that our linear equation is consistent with Russell and Gray. This discovery led to the inclusion of nonlinear terms added to the set of linear terms in R_{pp} such that significant improvement of AVO modeling accuracy is found. AVO modeling in terms of perturbation contrasts (a_f , a_μ , a_ρ) showed a significant decrease in accuracy of the linear approximation with respect to the second and third order approximations when perturbation is large (50%). For small perturbations (10%), the linear and nonlinear expressions are stable. Intermediate perturbation sizes (10% - 50%) revealed a steady decline in accuracy for all 3 expressions, especially for the linear case. In the case for the reflectivity contrasts ($\Delta f/f$, $\Delta\mu/\mu$, $\Delta\rho/\rho$), the same modeling

constraints were applied yet yielded different results. High reflectivity contrast values (50%) consistently revealed that the nonlinear expressions are accurate but show a notable decrease in accuracy for the linear expression. For small reflectivities (10%), the linear, second, and third order expressions predicted correctly with the same level of accuracy, while intermediate reflectivity sizes (10% - 50%) showed a steady decline in accuracy for all 3 expressions, proportional to the 3 perturbation equations. It is clear that each AVO observation made across all perturbation and reflectivity models showed better results in favour of the reflectivity models.

Another key outcome is the framework for dynamic poroelastic amplitude equations. The next step requires the expansion of the poroelastic perturbation models (a_f , a_μ , a_ρ) in each R_{11} , T_{11} , R_{12} , T_{12} for the porous-porous case and in each R_{11} , T_{11} , T_{12} for the porous-free fluid case. Also, substitution of the perturbation models with reflectivity models ($\Delta f/f$, $\Delta\mu/\mu$, $\Delta\rho/\rho$) is also desired.

7.3 Future directions

7.3.1 Synthetic data

Peter Manning and Joe Wong of CREWES developed an algorithm that creates synthetic shot gathers for horizontal seismic lines. The algorithm is executed with MATLAB and uses a finite-difference, time-stepping method to simulate elastic wave propagation in spatially, two-dimensional environments. The elastic wave can be simulated across 1000 m laterally and 2000 m in depth for an array of nominal receivers with single or multi-shot sources. The source parameter may be controlled for its depth, type of source (Ricker, windowed cosine, minimum phase), dominant frequency, and type of energy source (shallow explosion, deep explosion,

double-couple, X-monopole, Z-monopole). If desired, the seismic experiment can be manipulated to simulate a vertical seismic profile. Other parameters such as the grid size and time step increment can also be customized. It is important to note that the amplitudes as well as phases of the seismograms produced from this algorithm are not correct therefore the analysis of AVO synthetics would be an exercise to simulate the process of analysis of AVO rather than a study of the accuracy of AVO modeling.

7.3.2 Physical model data

CREWES has a three-dimensional positioning system based on high-precision linear electric motors, coupled to arrays of multiple transmitting and receiving piezoelectric transducers (Wong et al., 2009). For generating and detecting ultrasonic waves, piezoelectric transducers called piezopins are used. Piezopins are cylindrical with dimensions approximately 1.0 mm by 0.5 mm long. The piezopins are interchangeable on two gantry carriages and can act either as sources or as receivers that generate and detect ultrasonic seismic pulses. The maximum range of motion for these motors is 1000 mm, 800 mm, and 160 mm in the x, y, and z directions respectively. The scale factor is $1:10^4$, so these dimensions represent a real-world volume 10.0 km by 8.0 km by 1.6 km respectively. The same scaling factor applies to time such that recorded seismic pulses at 1.0 MHz are scaled down to 100 Hz for real-world values. This system is designed to collect thousands of scale-model seismic data traces per hour. There are 8 linear motors in this system with digital position encoders and motor drives configured in a two-gantry orthogonal motion system and controlled through a controller board installed in a desktop computer. The physical model lab in CREWES has performed numerous experiments acquiring data for various different environments (Hernandez et al., 2011; Wong and Lines, 2011; Wong et al, 2011; Arthur et al.,

2012; Al Dulaijan et al., 2013; Isaac et al., 2010). A proposed model that incorporates a solid medium that is infused with a fluid could replicate a poroelastic system. The dimensions of this physical model would require discussions and planning with CREWES' physical modeling data expert.

7.3.3 Field data

Field data is ideal in testing the capabilities and limitations of the poroelastic AVO equations. Data that is well known and analyzed, and also show an attribute of permeated fluid inside a solid medium is preferable.

7.3.4 Generalization to dynamic poroelasticity

Dynamic poroelasticity shows an additional P-wave generated due to heterogeneity within a medium. The P-wave that geophysicists are familiar with for the elastic case is known as the fast P-wave and the additional P-wave generated by interaction with porous inclusions is known as the slow P-wave or Biot's slow wave. The Biot slow wave is generated due to heterogeneities in the porous medium that cause mode conversion of an incoming wave. The result is a wave that is subject to a high degree of attenuation, especially at low frequencies (Gurevich et al., 1998). Steps to move forward will determine a set of linear and nonlinear expressions to measure any modeling efficacy for amplitudes at varying frequencies.

7.3.5 Generalization to full poroelastic scattering

Estimating the seismic wave field's response corresponding to the small model parameters' perturbations is a classical problem in inverse scattering (Pan and Innanen, 2013). Instead of

perturbations and reflectivity models, scattering theory uses scattering potentials for the forward problem. For the inverse problem, Fréchet derivatives, which are sensitivity matrices, are considered as sensitivity kernels in the least squares inverse problem. The research of Pan and Innanen (2013) shows that it is possible to derive the poroelastic scattering potential by first introducing the poroelastic wave equations as shown by Biot in terms of displacement of the solid (\mathbf{u}) and displacement of the fluid relative to the solid (\mathbf{w}). These equations are thus

$$\nabla \cdot (\lambda_{\text{sat}} \nabla \cdot \mathbf{u} + C \nabla \cdot \mathbf{w}) \mathbf{I} + 2\mu \nabla^2 \mathbf{u} + \mathbf{F} = -\omega^2 (\rho_{\text{sat}} \mathbf{u} + \rho_f \mathbf{w}), \quad (7.8)$$

and

$$\nabla \cdot (C \nabla \cdot \mathbf{u} + M \nabla \cdot \mathbf{w}) \mathbf{I} + \mathbf{f} = -\omega^2 (\rho_f \mathbf{u} + \tilde{\rho} \mathbf{w} + m \mathbf{w}), \quad (7.9)$$

where λ_{sat} , C , M , μ , ρ_{sat} , ρ_f , $\tilde{\rho}$, and m are 8 poroelastic parameters and ω is angular frequency.

We may write equations (7.8) and (7.9) in matrix form such that

$$\mathbf{L}_p(\mathbf{r}, \omega) \cdot \begin{pmatrix} \mathbf{u}(\mathbf{r}, \omega) \\ \mathbf{w}(\mathbf{r}, \omega) \end{pmatrix} = - \begin{pmatrix} \mathbf{F} \\ \mathbf{f} \end{pmatrix}, \quad (7.10)$$

where $\mathbf{L}_p(\mathbf{r}, \omega)$ is the operator of the scattered wave field in terms of spatial coordinates ($\mathbf{r} = x, y, z$) and frequency (ω). This operator is written as a matrix consisting of 4 sub matrices such that

$$\mathbf{L}_p(\mathbf{r}, \omega) = \begin{pmatrix} \mathbf{L}^{s1}(\mathbf{r}, \omega) & \mathbf{L}^{f1}(\mathbf{r}, \omega) \\ \mathbf{L}^{s2}(\mathbf{r}, \omega) & \mathbf{L}^{f2}(\mathbf{r}, \omega) \end{pmatrix}, \quad (7.11)$$

where each sub matrix \mathbf{L}^{s1} , \mathbf{L}^{f1} , \mathbf{L}^{s2} , and \mathbf{L}^{f2} contains 9 elements and are implicitly written as

$$\begin{aligned}
\mathbf{L}^{s1} &= \begin{pmatrix} L_{xx}^{s1} & L_{xy}^{s1} & L_{xz}^{s1} \\ L_{yx}^{s1} & L_{yy}^{s1} & L_{yz}^{s1} \\ L_{zx}^{s1} & L_{zy}^{s1} & L_{zz}^{s1} \end{pmatrix}, \quad \mathbf{L}^{f1} = \begin{pmatrix} L_{xx}^{f1} & L_{xy}^{f1} & L_{xz}^{f1} \\ L_{yx}^{f1} & L_{yy}^{f1} & L_{yz}^{f1} \\ L_{zx}^{f1} & L_{zy}^{f1} & L_{zz}^{f1} \end{pmatrix} \\
\mathbf{L}^{s2} &= \begin{pmatrix} L_{xx}^{s2} & L_{xy}^{s2} & L_{xz}^{s2} \\ L_{yx}^{s2} & L_{yy}^{s2} & L_{yz}^{s2} \\ L_{zx}^{s2} & L_{zy}^{s2} & L_{zz}^{s2} \end{pmatrix}, \quad \mathbf{L}^{f2} = \begin{pmatrix} L_{xx}^{f2} & L_{xy}^{f2} & L_{xz}^{f2} \\ L_{yx}^{f2} & L_{yy}^{f2} & L_{yz}^{f2} \\ L_{zx}^{f2} & L_{zy}^{f2} & L_{zz}^{f2} \end{pmatrix}.
\end{aligned} \tag{7.12}$$

The complete details of these sub matrices may be found in Pan and Innanen (2013). From the wave operator, the scattering potential is simply the difference of the perturbed wave operator \mathbf{L}_P and the unperturbed wave operator \mathbf{L}_P^0 such that

$$\mathbf{V}_P = \mathbf{L}_P - \mathbf{L}_P^0. \tag{7.13}$$

The scattering potential is thus

$$\mathbf{V}_P = \begin{pmatrix} \mathbf{V}^{s1} & \mathbf{V}^{f1} \\ \mathbf{V}^{s2} & \mathbf{V}^{f2} \end{pmatrix}. \tag{7.14}$$

This completes the necessary steps involved in deriving the scattering potential \mathbf{V}_P and will be used to derive the poroelastic Fréchet derivative for the inversion case. Referring to equation (7.10), the Fréchet derivative may be derived by first writing the solution using integral representation as shown by Müller and Gurevich (2005). The equation becomes

$$\begin{pmatrix} u_i(\mathbf{r}, \omega) \\ w_i(\mathbf{r}, \omega) \end{pmatrix} = \int_{\Omega} d^3\mathbf{r}' \begin{pmatrix} G_{ij}^{s1}(\mathbf{r}', \omega) & G_{ij}^{f1}(\mathbf{r}', \omega) \\ G_{ij}^{s2}(\mathbf{r}', \omega) & G_{ij}^{f2}(\mathbf{r}', \omega) \end{pmatrix} \cdot \begin{pmatrix} F_j \delta(\mathbf{r} - \mathbf{r}') \\ f_j \delta(\mathbf{r} - \mathbf{r}') \end{pmatrix}. \tag{7.15}$$

This shows an integration of Green's tensor with the field-source tensor that produces the tensors for \mathbf{u} and \mathbf{w} . By combining the field-source term $(\mathbf{F}, \mathbf{f})^T = \mathbf{V} \cdot (\mathbf{u}, \mathbf{w})^T$ with the unperturbed displacements $(\mathbf{u}^0, \mathbf{w}^0)^T$, the scattering equation becomes

$$\begin{pmatrix} u_i \\ w_i \end{pmatrix} = \begin{pmatrix} u_i^0 \\ w_i^0 \end{pmatrix} + \int_{\Omega} dV \begin{pmatrix} G_{ij}^{s1} & G_{ij}^{f1} \\ G_{ij}^{s2} & G_{ij}^{f2} \end{pmatrix} \cdot \begin{pmatrix} V_{jk}^{s1} & V_{jk}^{f1} \\ V_{jk}^{s2} & V_{jk}^{f2} \end{pmatrix} \cdot \begin{pmatrix} u_k \\ w_k \end{pmatrix}. \tag{7.16}$$

The perturbed and unperturbed quantities of \mathbf{u} and \mathbf{w} may be written in terms of Green's functions for an inhomogeneous medium. Equation (7.16) becomes

$$\begin{pmatrix} \mathbf{G}_{il}^{s1} & \mathbf{G}_{il}^{f1} \\ \mathbf{G}_{il}^{s2} & \mathbf{G}_{il}^{f2} \end{pmatrix} = \begin{pmatrix} {}^0\mathbf{G}_{il}^{s1} & {}^0\mathbf{G}_{il}^{f1} \\ {}^0\mathbf{G}_{il}^{s2} & {}^0\mathbf{G}_{il}^{f2} \end{pmatrix} + \int_{\Omega} dV \begin{pmatrix} {}^0\mathbf{G}_{ij}^{s1} & {}^0\mathbf{G}_{ij}^{f1} \\ {}^0\mathbf{G}_{ij}^{s2} & {}^0\mathbf{G}_{ij}^{f2} \end{pmatrix} \cdot \begin{pmatrix} \mathbf{V}_{jk}^{s1} & \mathbf{V}_{jk}^{f1} \\ \mathbf{V}_{jk}^{s2} & \mathbf{V}_{jk}^{f2} \end{pmatrix} \cdot \begin{pmatrix} \mathbf{G}_{kl}^{s1} & \mathbf{G}_{kl}^{f1} \\ \mathbf{G}_{kl}^{s2} & \mathbf{G}_{kl}^{f2} \end{pmatrix}. \quad (7.17)$$

In simpler notation, equation (7.17) may be written as

$$\mathbf{G} = \mathbf{G}_0 + \int_{\Omega} dV \mathbf{G}_0 \mathbf{V} \mathbf{G}. \quad (7.18)$$

By inspection, the scattering equation can become an infinite series by replacing the perturbed Green's function on the far-right hand side of equation (7.18) with the equation itself. Doing so creates an infinite series known as the Born series. This wave field can then be written as

$$\mathbf{G} = \mathbf{G}_0 + \int \mathbf{G}_0 \mathbf{V} \mathbf{G}_0 + \iint \mathbf{G}_0 \mathbf{V} \mathbf{G}_0 \mathbf{V} \mathbf{G}_0 + \dots \quad (7.19)$$

An approximation may be formed by terminating all nonlinear terms which includes terms that are beyond the second term in equation (7.19). Doing so produces the Born approximation. The Born approximation assumes weak inhomogeneity and the \mathbf{G}_0 term may be subtracted on both sides to give

$$\delta \mathbf{G} \approx \int_{\Omega} dV \mathbf{G}_0 \mathbf{V} \mathbf{G}_0. \quad (7.20)$$

The wave field $\delta \mathbf{G}$ can be described as a volume integral of the unperturbed Green's function \mathbf{G}_0 and the scattering potential \mathbf{V} . Referring back to the scattering equation in equation (7.17), the Born approximation assumption of weak inhomogeneity allows the Green's tensor on the far right hand side to become homogeneous, thus the scattered wave field may be written as

$$\begin{pmatrix} \delta \mathbf{G}_{il}^{s1} & \delta \mathbf{G}_{il}^{f1} \\ \delta \mathbf{G}_{il}^{s2} & \delta \mathbf{G}_{il}^{f2} \end{pmatrix} \approx \int_{\Omega} dV \begin{pmatrix} {}^0\mathbf{G}_{ij}^{s1} & {}^0\mathbf{G}_{ij}^{f1} \\ {}^0\mathbf{G}_{ij}^{s2} & {}^0\mathbf{G}_{ij}^{f2} \end{pmatrix} \cdot \begin{pmatrix} \mathbf{V}_{jk}^{s1} & \mathbf{V}_{jk}^{f1} \\ \mathbf{V}_{jk}^{s2} & \mathbf{V}_{jk}^{f2} \end{pmatrix} \cdot \begin{pmatrix} {}^0\mathbf{G}_{kl}^{s1} & {}^0\mathbf{G}_{kl}^{f1} \\ {}^0\mathbf{G}_{kl}^{s2} & {}^0\mathbf{G}_{kl}^{f2} \end{pmatrix}. \quad (7.21)$$

Finally, the poroelastic Fréchet derivative may be written in terms of the model parameter δs such that

$$\begin{pmatrix} \frac{\delta G_{il}^{s1}}{\delta s} & \frac{\delta G_{il}^{f1}}{\delta s} \\ \frac{\delta G_{il}^{s2}}{\delta s} & \frac{\delta G_{il}^{f2}}{\delta s} \end{pmatrix} \approx \int_{\Omega} dV \begin{pmatrix} {}^0G_{ij}^{s1} & {}^0G_{ij}^{f1} \\ {}^0G_{ij}^{s2} & {}^0G_{ij}^{f2} \end{pmatrix} \cdot \begin{pmatrix} \frac{V_{jk}^{s1}}{\delta s} & \frac{V_{jk}^{f1}}{\delta s} \\ \frac{V_{jk}^{s2}}{\delta s} & \frac{V_{jk}^{f2}}{\delta s} \end{pmatrix} \cdot \begin{pmatrix} {}^0G_{kl}^{s1} & {}^0G_{kl}^{f1} \\ {}^0G_{kl}^{s2} & {}^0G_{kl}^{f2} \end{pmatrix}. \quad (7.22)$$

This sensitivity matrix is crucial in perturbation analysis.

References

- Aki, K., and Richards, P. G., 1980, Quantitative seismology: Theory and methods: W. H. Freeman and Co.
- Aki, K., and Richards, P. G., 2002, Quantitative seismology, 2nd ed.: W. H. Freeman and Co.
- Al Dulaijan, K., Margrave, G., and Wong, J., 2013, A physical model investigation of P and S wave azimuthal anisotropy on transmission: CREWES Research Report, **25**, 1-16.
- Allard, J. F., 1993, Propagation of sound in porous media: Modelling sounds absorbing materials: Elsevier Applied Science.
- Arthur, J. M., Lawton, D. C., and Wong, J., 2012, Physical seismic modeling of a vertical fault: CREWES Research Report, **24**, 1-30.
- Biot, M. A., 1941, General theory of three-dimensional consolidation: Applied Physics, **12**, 155-164.
- Biot, M. A., 1962, Mechanics of deformation and acoustic propagation in porous media: Applied Physics, **33**, 1482-1498.
- Bortfeld, R., 1961, Approximation to the reflection and transmission coefficients of plane longitudinal and transverse waves: Geophys. Prosp., **9**, 485-503.
- Bourbié T., Coussy, O., and Zinzner, B., 1987, Acoustics of porous media: Editions Technip.
- Carcione, J. M., 2007, Wave fields in real media: Theory and numerical simulation of wave propagation in anisotropic, anelastic, porous and electromagnetic media, 2nd ed.: Elsevier Scientific Publ. Co., Inc.
- Carcione, J. M., Morency, C., and Santos, J. E., 2010, Computational poroelasticity – A review: Geophysics, **75**, 75A229-75A243.

- Castagna, J. P., 1993, Petrophysical imaging using AVO: The Leading Edge, March, 1993, 172-178.
- Castagna, J. P., and Backus, M. M., 1993, AVO analysis – tutorial and review, *in* Castagna, J. and Backus, M. M., eds, Offset-dependent reflectivity – Theory and practice of AVO analysis: Soc. Expl. Geophys., 3-36.
- Castagna, J. P., Swan, H. W., and Foster, D. J., 1998, Framework for AVO gradient and intercept interpretation: *Geophysics*, **63**, 948-956.
- Fatti, J. L., Vail, P. J., Smith, G. C., Strauss, P. J., and Levitt, P. R., 1994, Detection of gas in sandstone reservoirs using AVO analysis: A 3-D seismic case history using the geostack technique: *Geophysics*, **59**, 1362-1376.
- Foster, D. J., Keys, R. G., and Lane, F. D., 2010, Interpretation of AVO anomalies: *Geophysics*, **75**, 75A3-75A13.
- Gassmann, F., 1951, Über die elastizität poroser median: *Vierteljahrsschrift der naturforschenden gesellschaft*, **96**, 1-23.
- Gidlow, P. M., Smith, G. C., and Vail, P. J., 1992, Hydrocarbon detection using fluid factor traces: A case history: how useful is AVO analysis?: Joint Summer Research Workshop, SEG/EAGE, Expanded Abstracts, 78-89.
- Goodway, W. N., Chen, T., and Downton, J., 1997, Improved AVO fluid detection and lithology discrimination using Lamé petrophysical parameters; “ $\lambda\lambda$,” “ $\mu\mu$,” and “ λ/μ fluid stack,” from P and S inversions: 67th Annual International Meeting, SEG, Expanded Abstracts, 183-186.

- Gray, F., Chen, T., and Goodway, W., 1999, Bridging the gap: Using AVO to detect changes in fundamental elastic constants: 69th Annual International Meeting, SEG, Expanded Abstracts, 852-855.
- Gurevich, B., Ciz, R., and Denneman, A. I. M., 2004, Simple expressions for normal incidence reflection coefficients from an interface between fluid-saturated porous materials: *Geophysics*, **69**, 1372-1377.
- Gurevich, B., Sadovnichaja, A. P., Lopatnikov, S. L., and Shapiro, S. A., 1998, Scattering of a compressional wave in a poroelastic medium by an ellipsoidal inclusion: *Geophys. J. Int.*, **133**, 91-103.
- Hernandez, M., Innanen, K., and Wong, J., 2011, Internal multiple attenuation based on inverse scattering II: implementation in physical model seismic data: CREWES Research Report, **23**, 1-7.
- Innanen, K., 2011a, Inversion of the seismic AVF/AVA signatures of highly attenuative targets: *Geophysics*, **76**, R1-R14.
- Innanen, K., 2011b, Matrix forms for the Knott-Zoeppritz equations: CREWES Research Report, **23**, 1-5.
- Isaac, J. H., Wong, J., and Hall, K. W., 2010, Physical modelling of a 3D marine seismic survey: CREWES Research Report, **22**, 1-4.
- Keys, R. G., 1989, Polarity reversals in reflections from layered media: *Geophysics*, **54**, 900-905.
- Knott, C. G., 1899, Reflexion and refraction of elastic waves with seismological applications, *Philos. Mag.*, **XLVIII**, 64-97.

- Koefoed, O., 1955, On the effect of Poisson's ratios of rock strata on the reflection coefficients of plane waves: *Geophys. Prosp.*, **3**, 381-387.
- Levin, F. K., 1986, When reflection coefficients are zero: *Geophysics*, **51**, 736-741.
- Mahmoudian, F., 2013, Physical Modeling and Analysis of Seismic Data from a Simulated Fractured Medium: University of Calgary, PhD. Thesis.
- Moradi, S., and Lawton, D., C., 2013, Velocity-stress finite-difference modeling of poroelastic wave propagation: CREWES Research Report, **25**, 1-10.
- Müller, T. M., and Gurevich, B., 2005, A first order statistical smoothing approximations for the coherent wave field in random porous media: *J. Acoust. Soc. Am.*, **117**, 1796-1805.
- Müller, T. M., Gurevich, B., and Lebedev, M., 2010, Seismic wave attenuation and dispersion resulting from wave-induced flow in porous rocks – A review: *Geophysics*, **75**, 75A147-75A164.
- Ostrander, W. J., 1982, Method for interpretation of seismic records to yield indication of gaseous hydrocarbons: United States Patent No. 4,316,268.
- Ostrander, W. J., 1984, Plane-wave reflection coefficients for gas sands at nonnormal angles of incidence: *Geophysics*, **49**, 1637-1648.
- Pan, W., and Innanen, K., 2013, Poroelastic scattering potentials and inversion sensitivities: CREWES Research Report, **25**, 1-23.
- Pickett, G. R., 1963, Acoustic character logs and their application in formation evaluation: *J. Petr. Tech.*, **15**, 659-667.
- Quakenbush, M., Shang, B., and Tuttle, C., 2006, Poisson impedance: *The Leading Edge*, **25**, 128–138.

- Ren, H., Goloshubin, G., and Hilterman, F. J., 2009, Poroelastic analysis of amplitude-versus-frequency variations: *Geophysics*, **74**, N41-N48.
- Richards, P. G., and Frasier, C. W., 1976, Scattering of elastic waves from depth-dependent inhomogeneities: *Geophysics*, **41**, 441-458.
- Richards, T. C., 1961, Motion of the ground on arrival of reflected longitudinal and transverse waves at wide-angle reflection distances: *Geophysics*, **26**, 277-297.
- Russell, B. H., Gray, D., and Hampson, D. P., 2011, Linearized AVO and poroelasticity: *Geophysics*, **76**, C19-C29.
- Russell, B. H., Hedlin, K., Hilterman, F. J., and Lines, L. R., 2003, Fluid-property discrimination with AVO: A Biot-Gassmann perspective: *Geophysics*, **68**, 29-39.
- Rutherford, S. R., and Williams, R. H., 1989, Amplitude-versus-offset variations in gas sands: *Geophysics*, **54**, 680-688.
- Shuey, R. T., 1985, A simplification of the Zoeppritz equations: *Geophysics*, **50**, 609-614.
- Smith, G. C., and Gidlow, P. M., 1987, Weighted stacking for rock property estimation and detection of gas: *Geophys. Prosp.*, **35**, 993-1014.
- Smith, G. C., and Gidlow, P. M., 2000, A comparison of the fluid factor with lambda and mu in AVO analysis: 70th Annual International Meeting, SEG, Expanded Abstracts, 122–125.
- Stovas, A., and Ursin, B., 2001, Second-order approximations of the reflection and transmission coefficients between two viscoelastic isotropic media: *Journal of Seismic Exploration*, **9**, 223–233.
- Tatham, R.H., 1982, V_p/V_s and lithology: *Geophysics*, **47**, 336-344.
- White, J. E., 1983, *Underground Sound*: Elsevier Science Publishers.

- Wiggins, R., G. S. Kenny, and C. D. McClure, 1983, A method for determining and displaying the shear-velocity reflectivities of a geologic formation: European Patent Application 0113944.
- Wong, J., and Lines, L. R., 2011, Physical modeling I: reflections off a low-Q material: CREWES Research Report, **23**, 1-12.
- Wong, J., Mahmoudian, F., Gallant, E., and Margrave, G., 2011, Physical modeling III: Acquiring modeled data for VVAZ/AVAZ analysis: CREWES Research Report, **23**, 1-18.
- Zoeppritz, K., 1919, Erdbebenwellen VIII B, Über die Reflexion and Durchgang seismischer Wellen durch Unstetigkeitsflächen: Gottinger Nachr, **1**, 66-84.
- Zong, Z., Yin, X., and Wu, G., 2012, AVO inversion and poroelasticity with P- and S-wave moduli: Geophysics, **77**, N29-N36.

Appendix A: Poroelastic weighting factors

The contents of this appendix show the explicit forms of $R_{\text{PP}}^{(1)}$, $R_{\text{PP}}^{(2)}$, and $R_{\text{PP}}^{(3)}$ in both the perturbation (a_f , a_μ , a_ρ) and reflectivity ($\Delta f/f$, $\Delta\mu/\mu$, $\Delta\rho/\rho$) domains.

A.1 First order poroelastic weighting factors for a_f , a_μ , a_ρ

$$R_{\text{PP}}^{(1)} = W_{a_1} a_f + W_{a_2} a_\mu + W_{a_3} a_\rho \quad (\text{A.1})$$

$$W_{a_1} = \frac{1}{4} \left(1 + \sin^2 \theta_0 \right) - \frac{(\gamma_0)_{\text{dry}}^2}{4(\gamma_0)_{\text{sat}}^2} \left(1 + \sin^2 \theta_0 \right)$$

$$W_{a_2} = \frac{(\gamma_0)_{\text{dry}}^2}{4(\gamma_0)_{\text{sat}}^2} \left(1 + \sin^2 \theta_0 \right) - \frac{2}{(\gamma_0)_{\text{sat}}^2} \sin^2 \theta_0$$

$$W_{a_3} = \frac{1}{4} - \frac{\sin^2 \theta_0}{4}$$

A.2 Second order poroelastic weighting factors for a_f , a_μ , a_ρ

$$R_{\text{PP}}^{(2)} = W_{a_4} a_f^2 + W_{a_5} a_\mu^2 + W_{a_6} a_\rho^2 + W_{a_7} a_f a_\mu + W_{a_8} a_f a_\rho + W_{a_9} a_\mu a_\rho \quad (\text{A.2})$$

$$W_{a_4} = \left(1 - \frac{(\gamma_0)_{\text{dry}}^2}{(\gamma_0)_{\text{sat}}^2} \right) \frac{\sin^2 \theta_0}{4} + \frac{1}{8} \left(1 - \frac{(\gamma_0)_{\text{dry}}^4}{(\gamma_0)_{\text{sat}}^4} \right)$$

$$W_{a_5} = \frac{(\gamma_0)_{\text{dry}}^2}{4(\gamma_0)_{\text{sat}}^2} \left(\sec^2 \theta_0 - \frac{(\gamma_0)_{\text{dry}}^2}{2(\gamma_0)_{\text{sat}}^2} \right) - \frac{2}{(\gamma_0)_{\text{sat}}^2} \left(1 - \frac{1}{2(\gamma_0)_{\text{sat}}} \right) \sin^2 \theta_0$$

$$W_{a_6} = \frac{1}{8} \left(1 - \frac{2}{(\gamma_0)_{\text{sat}}} \sin^2 \theta_0 \right)$$

$$W_{a_7} = -\frac{(\gamma_0)_{\text{dry}}^2}{4(\gamma_0)_{\text{sat}}^2} \left(1 - \frac{(\gamma_0)_{\text{dry}}^2}{(\gamma_0)_{\text{sat}}^2} \right)$$

$$W_{a_8} = -\left(1 - \frac{(\gamma_0)_{\text{dry}}^2}{(\gamma_0)_{\text{sat}}^2} \right) \frac{\sin^2 \theta_0}{4}$$

$$W_{a_9} = \frac{1}{(\gamma_0)_{\text{sat}}^2} \left(1 - \frac{(\gamma_0)_{\text{dry}}^2}{4} \right) \sin^2 \theta_0$$

A.3 Third order poroelastic weighting factors for a_f , a_μ , a_ρ

$$\begin{aligned} R_{\text{PP}}^{(3)} = & W_{a_{10}} a_f^3 + W_{a_{11}} a_\mu^3 + W_{a_{12}} a_\rho^3 + W_{a_{13}} a_f^2 a_\mu + W_{a_{14}} a_f^2 a_\rho + W_{a_{15}} a_\mu^2 a_f \\ & + W_{a_{16}} a_\mu^2 a_\rho + W_{a_{17}} a_\rho^2 a_f + W_{a_{18}} a_\rho^2 a_\mu + W_{a_{19}} a_f a_\mu a_\rho \end{aligned} \quad (\text{A.3})$$

$$W_{a_{10}} = \frac{1}{64} \left[5(1 + 3 \sin^2 \theta_0) \left(1 - \frac{(\gamma_0)_{\text{dry}}^4}{5(\gamma_0)_{\text{sat}}^4} \right) + \frac{(\gamma_0)_{\text{dry}}^2}{(\gamma_0)_{\text{sat}}^2} (1 - 13 \sin^2 \theta_0) - 5 \frac{(\gamma_0)_{\text{dry}}^6}{(\gamma_0)_{\text{sat}}^6} \left(1 - \frac{\sin^2 \theta_0}{5} \right) \right]$$

$$\begin{aligned} W_{a_{11}} = & \frac{5}{64} \frac{(\gamma_0)_{\text{dry}}^6}{(\gamma_0)_{\text{sat}}^6} \left(1 - \frac{\sin^2 \theta_0}{5} \right) + \frac{(\gamma_0)_{\text{dry}}^2}{4(\gamma_0)_{\text{sat}}^2} \sec^2 \theta_0 + \frac{7}{4(\gamma_0)_{\text{sat}}^3} \left(1 - \frac{2(\gamma_0)_{\text{dry}}^2}{7(\gamma_0)_{\text{sat}}^2} \right) \sin^2 \theta_0 \\ & - \frac{2}{(\gamma_0)_{\text{sat}}^2} \left(1 - \frac{(\gamma_0)_{\text{dry}}^4}{16(\gamma_0)_{\text{sat}}^4} \right) \sin^2 \theta_0 - \frac{(\gamma_0)_{\text{dry}}^4}{4(\gamma_0)_{\text{sat}}^4} \end{aligned}$$

$$W_{a_{12}} = \frac{5}{64} \left(1 + \frac{\sin^2 \theta_0}{5} \right) - \frac{3}{16(\gamma_0)_{\text{sat}}} \sin^2 \theta_0$$

$$\begin{aligned} W_{a_{13}} = & \frac{15(\gamma_0)_{\text{dry}}^6}{64(\gamma_0)_{\text{sat}}^6} \left(1 - \frac{\sin^2 \theta_0}{5} \right) - \frac{(\gamma_0)_{\text{dry}}^2}{64(\gamma_0)_{\text{sat}}^2} (1 + 3 \sin^2 \theta_0) - \frac{7(\gamma_0)_{\text{dry}}^4}{32(\gamma_0)_{\text{sat}}^4} \left(1 - \frac{3}{7} \sin^2 \theta_0 \right) \\ & - \frac{(\gamma_0)_{\text{dry}}^2}{4(\gamma_0)_{\text{sat}}^4} \left(1 - \frac{(\gamma_0)_{\text{dry}}^2}{2(\gamma_0)_{\text{sat}}^2} \right) \sin^2 \theta_0 + \frac{1}{8(\gamma_0)_{\text{sat}}^2} \sin^2 \theta_0 \end{aligned}$$

$$W_{a_{14}} = \frac{(\gamma_0)_{\text{dry}}^2}{32(\gamma_0)_{\text{sat}}^2} (1 + 9 \sin^2 \theta_0) - \frac{(\gamma_0)_{\text{dry}}^4}{64(\gamma_0)_{\text{sat}}^4} \sec^2 \theta_0 - \frac{1}{64} (1 + 17 \sin^2 \theta_0)$$

$$W_{a_{15}} = \left(1 - \frac{(\gamma_0)_{\text{dry}}^2}{(\gamma_0)_{\text{sat}}^2} \right) \left(\frac{(\gamma_0)_{\text{dry}}^2}{4(\gamma_0)_{\text{sat}}^4} - \frac{1}{2(\gamma_0)_{\text{sat}}^3} \right) \sin^2 \theta_0 - \frac{(\gamma_0)_{\text{dry}}^2}{4(\gamma_0)_{\text{sat}}^2} + \frac{31(\gamma_0)_{\text{dry}}^4}{64(\gamma_0)_{\text{sat}}^4} \left(1 - \frac{3}{31} \sin^2 \theta_0 \right) - \frac{15(\gamma_0)_{\text{dry}}^6}{64(\gamma_0)_{\text{sat}}^6} \left(1 - \frac{\sin^2 \theta_0}{5} \right)$$

$$W_{a_{16}} = \frac{5}{4(\gamma_0)_{\text{sat}}^2} \left(1 + \frac{(\gamma_0)_{\text{dry}}^2}{5(\gamma_0)_{\text{sat}}^2} \right) \sin^2 \theta_0 - \frac{3}{4(\gamma_0)_{\text{sat}}^3} \left(1 + \frac{(\gamma_0)_{\text{dry}}^2}{3(\gamma_0)_{\text{sat}}^{-1}} \right) \sin^2 \theta_0 - \frac{(\gamma_0)_{\text{dry}}^4}{64(\gamma_0)_{\text{sat}}^4} \sec^2 \theta_0$$

$$W_{a_{17}} = - \left(1 - \frac{(\gamma_0)_{\text{dry}}^2}{(\gamma_0)_{\text{sat}}^2} \right) \left(\frac{1}{8(\gamma_0)_{\text{sat}}} + \frac{\sec^2 \theta_0}{64} \right)$$

$$W_{a_{18}} = \frac{3}{8(\gamma_0)_{\text{sat}}^2} \left(1 - \frac{(\gamma_0)_{\text{dry}}^2}{3(\gamma_0)_{\text{sat}}} \right) \sin^2 \theta_0 - \frac{1}{16(\gamma_0)_{\text{sat}}} \sin^2 \theta_0 - \frac{(\gamma_0)_{\text{dry}}^2}{64(\gamma_0)_{\text{sat}}^2} \sec^2 \theta_0$$

$$W_{a_{19}} = \left(1 - \frac{(\gamma_0)_{\text{dry}}^2}{(\gamma_0)_{\text{sat}}^2} \right) \left(\frac{1}{4(\gamma_0)_{\text{sat}}^2} \sin^2 \theta_0 - \frac{(\gamma_0)_{\text{dry}}^2}{32(\gamma_0)_{\text{sat}}^2} \sec^2 \theta_0 \right)$$

A.4 First order poroelastic weighting factors for $\Delta f/f$, $\Delta \mu/\mu$, $\Delta \rho/\rho$

$$R_{\text{PP}}^{(1)} = W_{\Delta_1} \frac{\Delta f}{f} + W_{\Delta_2} \frac{\Delta \mu}{\mu} + W_{\Delta_3} \frac{\Delta \rho}{\rho} \quad (\text{A.4})$$

$$W_{\Delta_1} = \left(1 - \frac{(\gamma_0)_{\text{dry}}^2}{(\gamma_0)_{\text{sat}}^2} \right) \frac{\sec^2 \theta_0}{4}$$

$$W_{\Delta_2} = \frac{(\gamma_0)_{\text{dry}}^2}{4(\gamma_0)_{\text{sat}}^2} \sec^2 \theta_0 - \frac{2}{(\gamma_0)_{\text{sat}}^2} \sin^2 \theta_0$$

$$W_{\Delta_3} = \frac{1}{2} - \frac{\sec^2 \theta_0}{4}$$

A.5 Second order poroelastic weighting factors for $\Delta f/f$, $\Delta\mu/\mu$, $\Delta\rho/\rho$

$$\begin{aligned} R_{\text{PP}}^{(2)} = & W_{\Delta_4} \left(\frac{\Delta f}{f} \right)^2 + W_{\Delta_5} \left(\frac{\Delta\mu}{\mu} \right)^2 + W_{\Delta_6} \left(\frac{\Delta\rho}{\rho} \right)^2 + W_{\Delta_7} \frac{\Delta f}{f} \frac{\Delta\mu}{\mu} + W_{\Delta_8} \frac{\Delta f}{f} \frac{\Delta\rho}{\rho} \\ & + W_{\Delta_9} \frac{\Delta\mu}{\mu} \frac{\Delta\rho}{\rho} \end{aligned} \quad (\text{A.5})$$

$$W_{\Delta_4} = \frac{1}{8} \left(1 - \frac{(\gamma_0)_{\text{dry}}^2}{(\gamma_0)_{\text{sat}}^2} \right) \left(\sin^2 \theta_0 + \frac{(\gamma_0)_{\text{dry}}^2}{(\gamma_0)_{\text{sat}}^2} \right)$$

$$W_{\Delta_5} = \frac{(\gamma_0)_{\text{dry}}^2}{8(\gamma_0)_{\text{sat}}^2} \left(\sec^2 \theta_0 - \frac{(\gamma_0)_{\text{dry}}^2}{(\gamma_0)_{\text{sat}}^2} \right) - \frac{1}{(\gamma_0)_{\text{sat}}^2} \left(1 - \frac{1}{(\gamma_0)_{\text{sat}}} \right) \sin^2 \theta_0$$

$$W_{\Delta_6} = \left(1 - \frac{2}{(\gamma_0)_{\text{sat}}} \right) \frac{\sin^2 \theta_0}{8}$$

$$W_{\Delta_7} = -\frac{(\gamma_0)_{\text{dry}}^2}{4(\gamma_0)_{\text{sat}}^2} \left(1 - \frac{(\gamma_0)_{\text{dry}}^2}{(\gamma_0)_{\text{sat}}^2} \right)$$

$$W_{\Delta_8} = -\left(1 - \frac{(\gamma_0)_{\text{dry}}^2}{(\gamma_0)_{\text{sat}}^2} \right) \frac{\sin^2 \theta_0}{4}$$

$$W_{\Delta_9} = \frac{1}{(\gamma_0)_{\text{sat}}^2} \left(1 - \frac{(\gamma_0)_{\text{dry}}^2}{4} \right) \sin^2 \theta_0$$

A.6 Third order poroelastic weighting factors for $\Delta f/f$, $\Delta\mu/\mu$, $\Delta\rho/\rho$

$$\begin{aligned}
R_{\text{PP}}^{(3)} = & W_{\Delta_{10}} \left(\frac{\Delta f}{f} \right)^3 + W_{\Delta_{11}} \left(\frac{\Delta \mu}{\mu} \right)^3 + W_{\Delta_{12}} a_\rho^3 \left(\frac{\Delta \rho}{\rho} \right)^3 + W_{\Delta_{13}} \left(\frac{\Delta f}{f} \right)^2 \frac{\Delta \mu}{\mu} + W_{\Delta_{14}} \left(\frac{\Delta f}{f} \right)^2 \frac{\Delta \rho}{\rho} \\
& + W_{\Delta_{15}} \left(\frac{\Delta \mu}{\mu} \right)^2 \frac{\Delta f}{f} + W_{\Delta_{16}} \left(\frac{\Delta \mu}{\mu} \right)^2 \frac{\Delta \rho}{\rho} + W_{\Delta_{17}} \left(\frac{\Delta \rho}{\rho} \right)^2 \frac{\Delta f}{f} + W_{\Delta_{18}} \left(\frac{\Delta \rho}{\rho} \right)^2 \frac{\Delta \mu}{\mu} \\
& + W_{\Delta_{19}} \frac{\Delta f}{f} \frac{\Delta \mu}{\mu} \frac{\Delta \rho}{\rho}
\end{aligned} \tag{A.6}$$

$$W_{\Delta_{10}} = \frac{1}{64} \left[3 \left(1 - \frac{(\gamma_0)_{\text{dry}}^4}{(\gamma_0)_{\text{sat}}^4} \right) \sin^2 \theta_0 - 3 \frac{(\gamma_0)_{\text{dry}}^2}{(\gamma_0)_{\text{sat}}^2} \left(1 + \frac{\sin^2 \theta_0}{3} \right) + \left(1 + 7 \frac{(\gamma_0)_{\text{dry}}^4}{(\gamma_0)_{\text{sat}}^4} \right) - 5 \frac{(\gamma_0)_{\text{dry}}^6}{(\gamma_0)_{\text{sat}}^6} \left(1 - \frac{\sin^2 \theta_0}{5} \right) \right]$$

$$\begin{aligned}
W_{\Delta_{11}} = & \frac{5(\gamma_0)_{\text{dry}}^6}{64(\gamma_0)_{\text{sat}}^6} \left(1 - \frac{\sin^2 \theta_0}{5} \right) - \frac{1}{2(\gamma_0)_{\text{sat}}^2} \left(1 + \frac{(\gamma_0)_{\text{dry}}^2}{(\gamma_0)_{\text{sat}}^2} \right) \sin^2 \theta_0 + \frac{(\gamma_0)_{\text{dry}}^2}{16(\gamma_0)_{\text{sat}}^2} \sec^2 \theta_0 \\
& - \frac{(\gamma_0)_{\text{dry}}^4}{8(\gamma_0)_{\text{sat}}^4} \left(1 - \frac{\sin^2 \theta_0}{(\gamma_0)_{\text{sat}}^2} \right) + \frac{3}{4(\gamma_0)_{\text{sat}}^3} \sin^2 \theta_0
\end{aligned}$$

$$W_{\Delta_{12}} = \frac{1}{64} (1 - 3 \sin^2 \theta_0) + \frac{1}{16(\gamma_0)_{\text{sat}}} \sin^2 \theta_0$$

$$\begin{aligned}
W_{\Delta_{13}} = & \frac{1}{8(\gamma_0)_{\text{sat}}^2} \sin^2 \theta_0 - \frac{3(\gamma_0)_{\text{dry}}^2}{64(\gamma_0)_{\text{sat}}^2} \left(1 + \frac{(\gamma_0)_{\text{dry}}^4}{(\gamma_0)_{\text{sat}}^4} \right) \sin^2 \theta_0 - \frac{(\gamma_0)_{\text{dry}}^2}{4(\gamma_0)_{\text{sat}}^4} \left(1 - \frac{(\gamma_0)_{\text{dry}}^2}{2(\gamma_0)_{\text{sat}}^2} \right) \sin^2 \theta_0 \\
& - \frac{11(\gamma_0)_{\text{dry}}^4}{32(\gamma_0)_{\text{sat}}^4} \left(1 - \frac{3}{11} \sin^2 \theta_0 \right) + \frac{7(\gamma_0)_{\text{dry}}^2}{64(\gamma_0)_{\text{sat}}^2} \left(1 + \frac{15(\gamma_0)_{\text{dry}}^4}{7(\gamma_0)_{\text{sat}}^4} \right)
\end{aligned}$$

$$W_{\Delta_{14}} = \frac{(\gamma_0)_{\text{dry}}^2}{32(\gamma_0)_{\text{sat}}^2} (1 + 5 \sin^2 \theta_0) - \frac{(\gamma_0)_{\text{dry}}^4}{64(\gamma_0)_{\text{sat}}^4} \sec^2 \theta_0 - \frac{1}{64} (1 + 9 \sin^2 \theta_0)$$

$$\begin{aligned}
W_{\Delta_{15}} = & \left(\frac{(\gamma_0)_{\text{dry}}^2}{4(\gamma_0)_{\text{sat}}^4} - \frac{1}{2(\gamma_0)_{\text{sat}}^3} \right) \left(1 - \frac{(\gamma_0)_{\text{dry}}^2}{(\gamma_0)_{\text{sat}}^2} \right) \sin^2 \theta_0 - \frac{15(\gamma_0)_{\text{dry}}^6}{64(\gamma_0)_{\text{sat}}^6} \left(1 - \frac{3}{15} \sin^2 \theta_0 \right) \\
& + \frac{23(\gamma_0)_{\text{dry}}^4}{64(\gamma_0)_{\text{sat}}^4} \left(1 - \frac{3}{23} \sin^2 \theta_0 \right) - \frac{(\gamma_0)_{\text{dry}}^2}{8(\gamma_0)_{\text{sat}}^2}
\end{aligned}$$

$$W_{\Delta_{16}} = \frac{3}{4(\gamma_0)_{\text{sat}}^2} \left(1 - \frac{1}{(\gamma_0)_{\text{sat}}} \right) \sin^2 \theta_0 - \frac{(\gamma_0)_{\text{dry}}^2}{8(\gamma_0)_{\text{sat}}^2} \left(1 - \frac{2}{(\gamma_0)_{\text{sat}}} \right) \sin^2 \theta_0 - \frac{(\gamma_0)_{\text{dry}}^4}{64(\gamma_0)_{\text{sat}}^4} \sec^2 \theta_0$$

$$W_{\Delta_{17}} = \left(1 - \frac{(\gamma_0)_{\text{dry}}^2}{(\gamma_0)_{\text{sat}}^2} \right) \left(\frac{9}{64} \sin^2 \theta_0 - \frac{1}{8(\gamma_0)_{\text{sat}}} \sin^2 \theta_0 - \frac{1}{64} \right)$$

$$W_{\Delta_{18}} = -\frac{(\gamma_0)_{\text{dry}}^2}{64(\gamma_0)_{\text{sat}}^2} (1 - 9 \sin^2 \theta_0) - \frac{1}{16(\gamma_0)_{\text{sat}}} \left(1 + 2 \frac{(\gamma_0)_{\text{dry}}^2}{(\gamma_0)_{\text{sat}}^2} \right) \sin^2 \theta_0 - \frac{1}{8(\gamma_0)_{\text{sat}}^2} \sin^2 \theta_0$$

$$W_{\Delta_{19}} = \left(1 - \frac{(\gamma_0)_{\text{dry}}^2}{(\gamma_0)_{\text{sat}}^2} \right) \left(\frac{\sin^2 \theta_0}{4(\gamma_0)_{\text{sat}}^2} - \frac{(\gamma_0)_{\text{dry}}^2}{32(\gamma_0)_{\text{sat}}^2} \sec^2 \theta_0 \right)$$